UNIVERSITA' DEGLI STUDI DI PARMA

DOTTORATO DI RICERCA IN
"SCIENZA E TECNOLOGIA DEI MATERIALI"

CICLO XXXVII

Photopolymer-Based Technologies for 3D Printing and Frontal Polymerization

Coordinatore:
Prof. Enrico Dalcanale

Tutore:
Prof. Enrico Dalcanale

Dottorando: Alex Bonacini

Anni Accademici 2022/2023 – 2024/2025

Abstract

Photopolymerization has become a widely utilized technique, extensively applied across various fields such as 3D printing, surface coatings, dental composites, and numerous other applications. The first three chapters of this work are dedicated to the development of innovative photoresin formulations aimed at imparting specific properties to the photocured materials or affecting their behavior during photopolymerization.

The first chapter focuses on the incorporation of dynamic crosslinkers based on boronate ester functionalities into photoresins for vat photopolymerization (VP) 3D printing. These crosslinkers are evaluated as potential agents for reducing mechanical anisotropy in the resulting 3D-printed structures. The investigation begins with an analysis of the viscoelastic properties of the materials during and after photocuring, followed by 3D printing experiments and a comparative evaluation of the mechanical isotropy of the printed materials compared to control samples. The results indicate an enhancement in the isotropy of the 3D-printed materials.

The second chapter investigates isosorbide-based interpenetrating polymer networks (IPNs) synthesized via photopolymerization. The precursor photoresins for these materials were evaluated for their potential application in vat photopolymerization (VP) 3D printing. Taking advantage of their ability to degrade in water, isosorbide-based materials were identified as promising candidates for the production of disposable molds in complex-shape carbon fiber manufacturing and injection molding processes. The research focused on testing various formulations composed of two isosorbide derivatives, which were photocured using two principal protocols. A preliminary mechanical characterization of the photocured materials was performed, and rapid disintegration in water was confirmed. Finally, 3D printing trials demonstrated encouraging results but also highlighted significant challenges.

The third chapter focuses on the development of a formulation for fully cationic photoinduced frontal polymerization. This advanced manufacturing technique initiates a curing front by exposing localized regions of the resin to light. Once initiated, the curing front self-propagates, facilitating the polymerization of the entire resin. Typically, this process is achieved by combining cationic photoinitiators with thermal radical initiators, enabling what is known as radical-induced cationic frontal polymerization. In this study, a

novel formulation was created by blending two primary epoxy crosslinkers with both a cationic photoinitiator and a thermal cationic initiator. This formulation demonstrated the ability to support both thermally and photoinduced fully cationic frontal polymerization.

Finally, the last chapter presents a stand-alone topic, focusing on the study of quinoxaline cavitands as potential candidates for the sequestration of poly- and perfluoroalkyl substances (PFAS) from polluted water. PFAS constitute an emerging class of persistent micropollutants characterized by hydrophobic, fluorinated tails of varying lengths. Given that quinoxaline cavitands have previously demonstrated the ability to reversibly complex a range of hydrophobic molecules, they emerge as promising candidates for the decontamination of wastewater from PFAS. The study aims to investigate the host-guest complexation of PFAS with well-known quinoxaline-based cavitands, and to design and synthesize new ad hoc receptors. The effective complexation of PFAS with quinoxaline-based cavitands was suggested by ^{1}H and ^{19}F NMR titrations, although salt precipitation worsened the quality of the results. Also, the ability of these cavitands to absorb the micropollutants in water was investigated, the results suggest a higher efficiency in removing longer-chain PFAS compared to shorter ones. Research then switched on the development of a new receptor capable of efficiently hosting both long and short-chain PFAS by combining hydrophobic interactions with an ionic bond promoted by the presence of permanent ammonium function on one quinoxaline wall. Preliminary investigations into the absorption of PFAS in water led to promising results for both long and short-chain species.

Table of contents

Chapter 0

Fundamentals on 3D Printing

Chapter 1

Boronate Esters Dynamic Networks for the Reduction of Mechanical Anisotropy in Vat 3D Printed Manufacts

Chapter 2

Photocurable Isosorbide-Based Water Disintegrable Interpenetrating Polymer Networks

Chapter 4

Sequestration of Anthropogenic Perfluorinated Micropollutants with Quinoxaline-based Cavitands

Chapter 0

“Fundamentals on 3D Printing”

The 3D printing techniques

3D printing technologies are innovative methods that enable the rapid and cost-effective productionof complex, highly customizable objects. These techniques have the potential to revolutionize the manufacturing industry by increasing production speed, reducing costs, and enabling the creation of products tailored to specific consumer requirements due to the high degree of design freedom they offer.

3D printing offers several advantages, largely due to its ability to produce objects directly from 3D digital models created using CAD (Computer Aided Design) models. The process begins with the design of the object in a CAD program, where the three-dimensional model is generated. Once the design is finalized, the CAD data is processed and converted into a series of thin horizontal layers, each representing a cross-section of the object. These layers are then sequentially printed by the 3D printer, which constructs the object layer by layer.[1,2] The printer uses various methods, such as extruding molten material, sintering powder, or curing resins, depending on the specific 3D printing technique. This layer-by-layer construction allows for the creation of complex geometries and intricate details that would be difficult or impossible to achieve using traditional manufacturing methods. The ability to precisely control each layer's dimensions and structure provides a high level of design flexibility, making 3D printing a powerful tool for rapid prototyping and customized production.

The most commonly used 3D printing techniques include fused deposition modelling (FDM), selective laser sintering (SLS), inkjet 3D printing, and stereolithography (SLA). Each technique has distinct advantages and limitations, particularly in terms of cost, materials, printing speed, resolution, and final product performance.[3]

- Fused deposition modeling (FDM) is widely used for manufacturing polymeric and composite materials. In FDM, thermoplastic filaments are heated to a molten state and extruded through a nozzle onto a build platform, layer by layer. The layers adhere to each other as the material solidifies. Common thermoplastics like PC (polycarbonate), ABS (acrylonitrile-butadiene-styrene), and PLA (polylactic acid) are frequently used due to their low melting temperatures. Print quality can be optimized by adjusting parameters such as layer thickness, print orientation, pattern

width and angle, and internal void volume. FDM is known for its cost-effectiveness and versatility but may be limited by lower resolution and anisotropic material properties, where strength can vary in different directions.[4]

- Selective laser sintering (SLS) involves the use of powdered materials, including thermoplastics, metals, ceramics, and glass. These powders are sintered by a high-powered laser, which selectively fuses the particles together in a localized manner.[5] The resolution of the printed object is influenced by the particle size, laser power, and scanning speed.[6] After sintering, residual powder must be carefully removed from the final product. SLS is well-suited for creating complex and durable parts, with examples of its use in producing polymeric items like nylon, glass-filled nylon, and polystyrene, as well as metallic parts such as steel, stainless steel alloys, bronze, and titanium. However, it is often more expensive and produces a rough, powdery surface finish.

- Inkjet 3D printing works by spraying fine powders onto a platform using an inkjet printhead. After each layer of powder is deposited, the platform lowers, and a new layer is added. A binding liquid is then applied to the powder to bind the layers together, facilitating the formation of the desired object. The process is repeated until the object is complete, and the excess powder must be removed at the end. Factors influencing the final product quality include powder particle size, binder viscosity, binder-powder interaction, and binder deposition speed. This technique is cost-effective, fast, and allows for multi-material printing, though the resulting objects typically have moderate mechanical properties.[3]

SLA is described in detail in the next section.

Stereolithography (SLA)

Stereolithography (SLA) is an advanced 3D printing technique that fabricates three-dimensional structures via the localized, in situ polymerization of photocurable resins. This

process employs a monochromatic light source, typically within the UV-visible spectrum, to selectively solidify regions of the resin, either layer by layer or point by point.[7]

The SLA process begins with a photopolymerizable resin, typically consisting of (meth)acrylic monomers or, less commonly, epoxy monomers, combined with photoinitiators that respond to the specific wavelength of the light source.

While alternative configurations exist, the resin is usually contained in a vat with a transparent, anti-adhesion plastic bottom (commonly made of a fluorinated ethylene propylene copolymer) to minimize adhesion to the tray. Above the vat, a movable metallic platform serves as the build surface for the 3D object.

To form each layer, the platform lowers to a precise distance from the bottom of the vat, creating a thin film of resin between the platform and the anti-adhesion surface. A light source, such as a laser, an LCD screen, or a digital light projector (DLP), selectively irradiates specific regions of the resin layer, initiating polymerization and forming the first layer of the object. After curing, the platform elevates, allowing uncured resin to refill the space vacated by the solidified layer. This cycle is repeated iteratively to construct the object layer by layer.[8] The weak adhesion of the cured material to the vat's bottom ensures that the solidified layer adheres preferentially to the platform, facilitating its detachment from the film during the lifting phase.[7] (**Figure 1**)

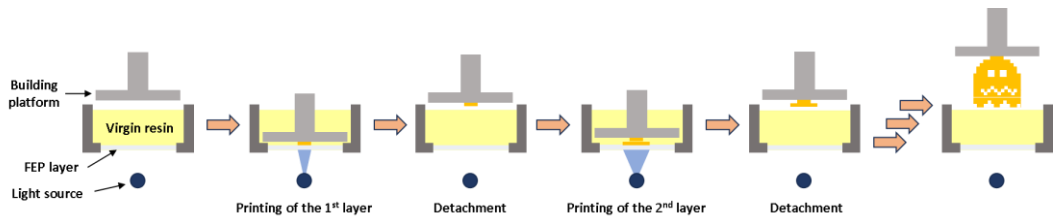

Figure 1. Schematic representation of the operating principle of an SLA apparatus.

SLA is renowned for its ability to produce objects with exceptional surface finish and high resolution, making it a preferred technique for applications such as biomedical devices, aerospace components, and prototyping. For example, SLA can fabricate biodegradable and biocompatible polymers used in tissue scaffolds, surgical tools, dental prosthetics, and

hearing aids. In the aerospace sector, SLA has been utilized to create prototypes of wing profiles and cabin components, including seatbacks and armrests.

Despite its many advantages, SLA also has notable limitations. Its relatively slow printing speed stems from the time-intensive curing process required for each layer, which is influenced by the intensity of the light source. Consequently, even moderately sized objects may take several hours to complete. Furthermore, photopolymer resins and unreacted photoinitiators exhibit cytotoxic properties, necessitating careful handling and proper disposal.

The mechanical properties of SLA-printed objects often fall short when compared to those produced by conventional manufacturing methods. This disparity arises from a limited range of commercially available monomers, the low viscosity required for UV-curable resins, and the intrinsic anisotropy of printed structures. These factors limit formulation flexibility and compromise mechanical uniformity.

To enhance mechanical properties, a widely adopted method involves two-step curing processes. During printing, the layers are only partially polymerized, leaving reactive functional groups in the freshly printed material, commonly referred to as “green”. A subsequent post-curing step, using UV-visible light and potentially thermal treatments, enhances the overall degree of polymerization and forms covalent bonds between adjacent layers.[8] This approach improves isotropy and mechanical strength, although some anisotropy persists, albeit to a lesser extent compared to other 3D printing techniques. (**Figure 2**)

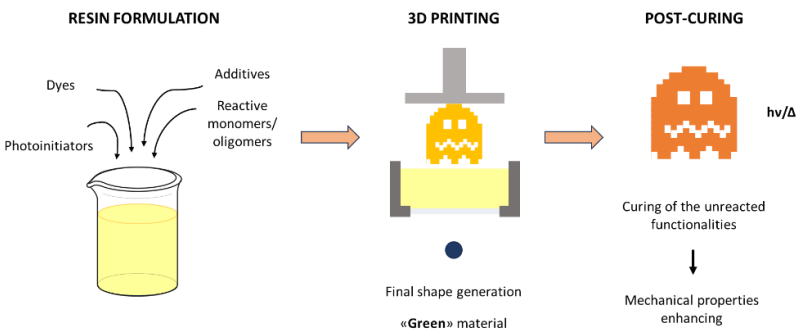

Figure 2. Representative image illustrating the various stages involved in a typical SLA printing process.

References

(1) P. A. Webb, A review of rapid prototyping (RP) techniques in the medical and biomedical sector. *J. Med. Eng. Technol.* **2000**, *24*, 149-153, https://doi.org/10.1080/03091900050163427.
(2) L. C. Hieu, N. Zlatov, J. Vander Sloten, E. Bohez, L. Khanh, P. H. Binh, Medical rapid prototyping applications and methods. *Assem. Autom.* **2005**, *25*, 284–92, https://doi.org/10.1108/01445150510626415.
(3) X. Wang, M. Jiang, Z. Zhou, J. Gou, D. Hui, 3D printing of polymer matrix composites: A review and prospective. *Compos. B: Eng.* **2017**, *110*, 442-458, 10.1016/j.compositesb.2016.11.034.
(4) K. Rajan, M. Samykano, K. Kadirgama, W. S. W. Harun, M. M. Rahman, Fused deposition modeling: process, materials, parameters, properties, and applications. *J. Adv. Manuf. Technol.* **2022**, *120*, 1531-1570, https://doi.org/10.1007/s00170-022-08860-7.
(5) D. D. Gu, W. Meiners, K. Wissenbach, R. Poprawe, Laser additive manufacturing of metallic components: Materials, processes and mechanisms. *Int. Mat. Rev.* **2012**, *57*, 133–164, https://doi.org/10.1179/1743280411Y.0000000014.
(6) I. Gibson, D. Shi, Material properties and fabrication parameters in selective laser sintering process. *Rapid Prototyp. J.* **1997**, *3*, 129-136, https://doi.org/10.1108/13552549710191836.
(7) J. Huang, Q. Qin, J. Wang, A review of stereolithography: Processes and systems. *Processes* **2020**, *8*, 1138, https://doi.org/10.3390/pr8091138.
(8) F. P. Melchels, J. Feijen, D. W. Grijpma, A review on stereolithography and its applications in biomedical engineering. *Biomater.* **2010**, *31*, 6121-6130, https://doi.org/10.1016/j.biomaterials.2010.04.050.

Chapter 1

"Boronate Esters Dynamic Networks for the Reduction of Mechanical Anisotropy in Vat 3D Printed Manufacts"

Adapted from: A. Bonacini, E. Saccani, C. Sciancalepore, D. Milanese, G. Drago, A. Pedrini, R. Pinalli, R. Nicolaÿ, E. Dalcanale, Boronate Esters Dynamic Networks for the Reduction of Mechanical Anisotropy in Vat 3D Printed Manufacts, *ACS Appl. Polym. Mater.* **2025**, *7*, 2624–2632. https://doi.org/10.1021/acsapm.4c04101.

1.1 Introduction

3D printing, also known as additive manufacturing (AM), offers efficient and cost-effective methods for producing complex, customizable objects.[1] Its versatility has broadened its applications across a wide range of fields, including aerospace,[2,3] energy,[4] construction,[5] biomedicine,[6-11] and many others.[12-18] Among the various 3D printing techniques, vat photopolymerization (VP) is distinguished by its ability to produce high-resolution structures using photopolymerizable resins. Key techniques, such as stereolithography (SLA), masked stereolithography (MSLA), and digital light processing (DLP), enable precise fabrication by selectively curing resin portions through localized exposure to UV-visible light.[19-21]

Despite these advantages, VP techniques have certain limitations, such as relatively slow production times that increase with object size, the requirement for low-viscosity resins, and a certain degree of anisotropy in the mechanical properties of the final prints, influenced by factors such as layer orientation, thickness, and irradiation time.[22-25]

Typical formulations for VP 3D printing consist of photopolymerizable oligomers and monomers combined with appropriate photoinitiators. Commonly employed polymerization mechanisms include free radical polymerization of (meth)acrylates,[26] photo-induced radical thiol-ene click chemistry,[27] and cationic ring-opening polymerization of epoxy groups.[28]

Recent advancements in VP 3D printing materials have focused on integrating specific functionalities into photopolymerizable formulations, yielding materials with well-defined properties. One key area of interest is the incorporation of dynamic covalent cross-links into VP 3D-printed thermosets, enabling functionalities such as post-printing reshaping, self-healing, adhesion, and reprocessing. Examples of dynamic covalent chemistries explored in VP 3D printing include β-hydroxy ester transesterification,[29,30] disulfide exchange,[31,32] and imine metathesis.[33]

A primary feature of materials that incorporate dynamic covalent cross-linking is their ability to relax applied stress by dissipating stored energy through topological reorganization. The relaxation rate is mainly governed by the exchange kinetics of dynamic bonds. In particular, materials containing boronate esters demonstrate the ability to rapidly relax stress at room

temperature due to catalyst-free rapid metathesis reactions between dynamic covalent cross-links.[34-37]

The chemical compatibility of boronate esters with a wide range of functional groups and reactive species, such as (meth)acrylates, amines, imines, aldehydes, epoxides, thiols,[38,39] and free radicals,[40,41] is another highly attractive feature of these moieties, making them ideal candidates for VP 3D printing applications.

In 2021, Robinson et al. successfully incorporated dynamic boronate ester cross-links into VP 3D-printed materials via photo-induced radical thiol-ene addition. These materials exhibited covalently adaptable network properties, allowing for stress relaxation at room temperature, surface smoothing, and post-printing adhesion. Boronate ester metathesis was also used to functionalize the printed materials with dyes, enhancing the complexity of the final constructs. However, to prevent structural collapse at room temperature, a small fraction of non-dynamic cross-links was necessary.[42]

In 2023, Sinawehl et al. developed boronate ester-based VP 3D-printed materials with potential applications in bone regeneration. By leveraging boronate ester chemistry, these materials could undergo controlled hydrolysis under both physiological and acidic conditions.[43]

In this study, we present a photopolymerized material that integrates dynamic boronate ester-based cross-linking with non-dynamic cross-linking. The material is synthesized via photo-induced free radical polymerization of a (meth)acrylate-based formulation and has demonstrated excellent suitability for VP 3D printing applications, exhibiting minimal shrinkage and rapid curing kinetics. Additionally, the material exhibited minimal creep at 65 °C, and 3D-printed specimens displayed reduced mechanical anisotropy compared to reference materials when printed in different layer orientations. (**Figure 1**)

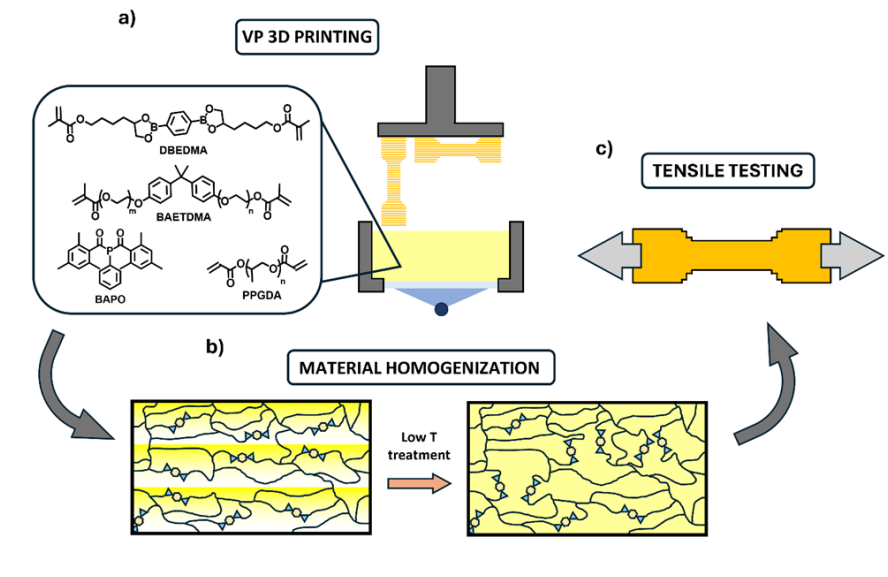

Figure 1. a) 3D printing of photocurable resins in different orientations followed by **b)** a low-temperature treatment to promote boronate ester metathesis reactions, **c)** enhancing material mechanical isotropy evaluated through tensile tests.

1.2 Results and discussion

The primary objective of this work is to develop a photocurable cross-linked material capable of rearranging its network topology at low temperatures by leveraging boronate ester metathesis chemistry. This strategy aims to reduce the mechanical anisotropy commonly observed in 3D-printed structures. To effectively achieve this goal through moderate temperature post-treatments, it is essential to maintain a low glass transition temperature (T_g). A low T_g ensures that the dynamic exchange of functional groups occurs without being restricted by the limited mobility of the polymer matrix.

1.2.1 Photoresin formulation and photocuring study

A diboronate ester dimethacrylate **(DBEDMA)** was selected as the primary dynamic cross-linker and synthesized on a large scale (synthetic pathway detailed in **Scheme A1**, and NMR characterization provided in **Figures A1–A5**).

In addition to **DBEDMA**, a commercial poly(propylene glycol) diacrylate (**PPGDA**) was incorporated into the final photocurable formulations. **PPGDA** has an average molar mass of 851 g/mol, as determined by ^{1}H NMR (refer to **Figure A6** and **Equations A1.1**-**A1.2**). This long and flexible static crosslinker increases the overall flexibility of the material, allowing for network rearrangement while ensuring that the material retains its desired shape.

A series of photocurable formulations with varying ratios of **DBEDMA** and **PPGDA** were tested. Each formulation contained the photoinitiator phenylbis(2,4,6-trimethylbenzoyl)phosphine oxide (**BAPO**) at a concentration of 1 mol% relative to the total moles of (meth)acrylate functions. This is equivalent to 2 mol% with respect to the total amount of crosslinker molecules. The molecular structures of the components are shown in **Figure 1**, and the molar ratios are specified in **Table 1** (additional details in **Table A1.1**).

Formulation	PPGDA	DBEDMA	BAETDMA	BAPO
100PPGDA	100 mol%	/	/	1 mol%
10DBEDMA**90**PPGDA	90 mol%	10 mol%	/	1 mol%
20DBEDMA**80**PPGDA	80 mol%	20 mol%	/	1 mol%
30DBEDMA**70**PPGDA	70 mol%	30 mol%	/	1 mol%
40DBEDMA**60**PPGDA	60 mol%	40 mol%	/	1 mol%
60DBEDMA**40**PPGDA	40 mol%	60 mol%	/	1 mol%
80DBEDMA**20**PPGDA	20 mol%	80 mol%	/	1 mol%
100DBEDMA	/	100 mol%	/	1 mol%
40BAETDMA**60**PPGDA	60 mol%	/	40 mol%	1 mol%

Table 1. Molar ratios of the components used in the photocurable formulations.

Preliminary studies of the viscoelastic response during photocuring were conducted using photorheology experiments at 25 °C. The results show a rapid increase in both storage modulus (G') and loss modulus (G") (**Figure 2**, left) immediately after the onset of irradiation at 50 s, with the moduli reaching a plateau within 40 s, depending on the specific formulation. Notably, a higher molar ratio of **DBEDMA** to **PPGDA** results in a slower

photopolymerization rate, which reflects the lower reactivity of methacrylates compared to acrylates in radical polymerization. This slower reaction is clearly illustrated by the t90 values (**Figure 2**, right), representing the time required to reach 90 % of the final G' value, further reinforcing the observed trend.

Additionally, the final values of G', G'', and complex viscosity |η*| (**Figure A1.8**) increase with the molar percentage of **DBEDMA** in the resin. This suggests that a higher **DBEDMA** content results in a higher crosslinking density, attributed to the shorter molecular structure of **DBEDMA** relative to the longer **PPGDA**.

Finally, the post-curing shrinkage of the photoresins was measured by monitoring the thickness of the resin over time under a constant normal force applied by the rheometer.[44] The results show minimal shrinkage, ranging from 5 % to 8 %, with no clear trend across the different formulations (**Figure A1.9**).

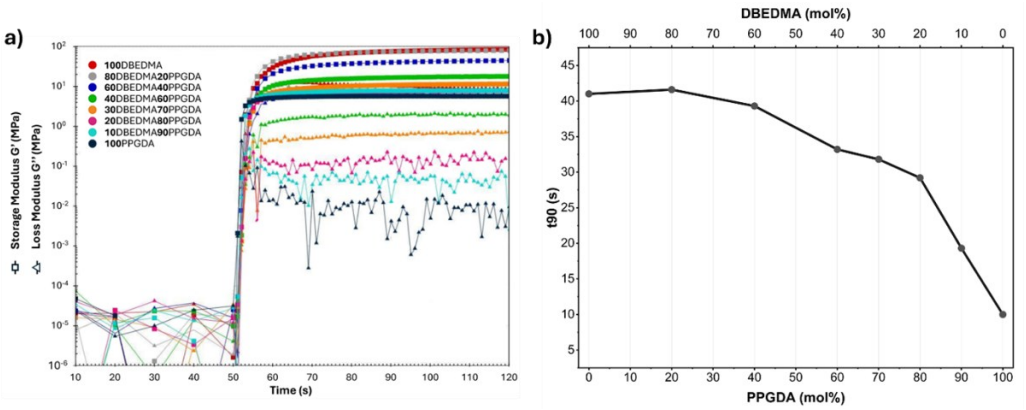

Figure 2. a) G' and G'' plotted as a function of time during the irradiation of the photoresins for 70 s, following a 50 s equilibration period in the dark, **b)** corresponding t90 values, representing the time required to reach 90 % of the final G' value.

1.2.2 Photopolymerization and viscoelastic characterization of materials

Flat samples were photocured into various shapes by irradiating resin-filled molds using a monochromatic 365 nm lamp for 5 minutes at a power density of 55 mW/cm².

The viscoelastic properties of the resulting materials, which remained thermally stable up to approximately 210 °C (**Figure A1.10**), were determined using DMA. DMA demonstrated that materials with **DBEDMA** content above 40 mol% exhibit heterogeneity, as evidenced by a broad tan δ peak (**Figure A1.11**). This prompted further investigations into formulations with a **DBEDMA** content cap at 40 mol%. This adjustment was made not only to improve material homogeneity but also to enable effective dilution of synthetic **DBEDMA** with commercially available molecules. The results (shown in **Figure 3**) indicate that all materials exhibit storage moduli (E') in the range of 10^3 MPa at low temperatures. Around -40 °C, the modulus decreases by two orders of magnitude, resulting in the formation of a rubbery plateau. The E' values measured at 25 °C are consistent with the final G' values obtained from photorheology, following the relationship E' ≈ 3 G'. Moreover, the E' values within the rubbery plateau exhibit the same trend observed in the photorheology experiments, increasing with the molar percentage of **DBEDMA**.

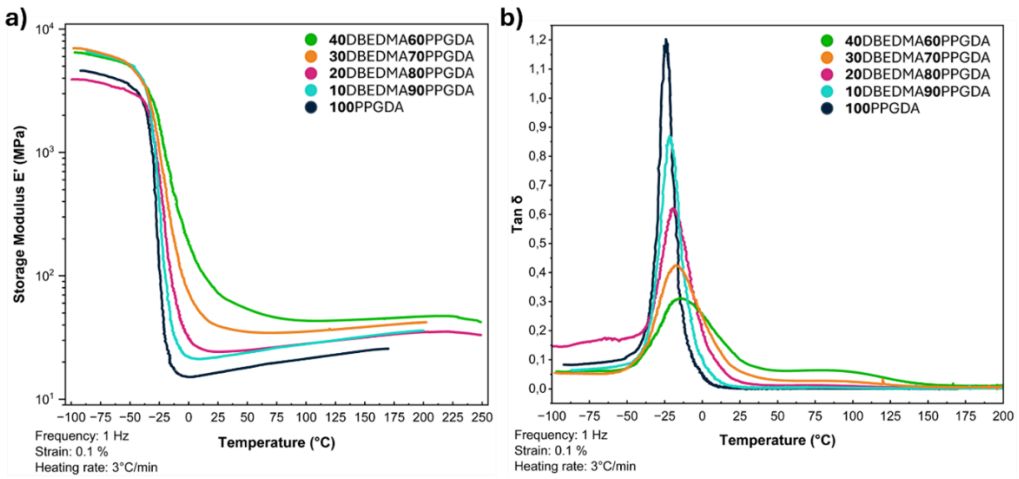

Figure 3. a) Storage modulus E' **b)** and tan δ of photocured materials as function of temperature.

T_g were estimated using both DMA and DSC, with the values extrapolated from DMA based on tan δ peaks being higher than those obtained from the DSC curves (**Figure A1.12**). In both cases, the glass transition temperatures increased with the molar percentage of the more

rigid **DBEDMA** relative to the more flexible **PPGDA**. However, all absolute T_g values were, as anticipated, lower than room temperature.

Stress relaxation studies were performed on the photocured materials at 65 °C (**Figure 4a**), a temperature at which all materials exhibit a rubbery plateau, as confirmed by previous DMA characterizations. The results indicate that the ability of the materials to relax stress increases with the molar fraction of dynamic **DBEDMA** compared to static **PPGDA**. Specifically, **DBEDMA**-rich materials show both a higher relaxation rate and lower residual stress after 30 min, whereas sample **100**PPGDA exhibits no capacity to relieve applied stress. Notably, stress relaxation increases with increasing **DBEDMA** concentration, indicating an increasing ability to rearrange the three-dimensional network due to the dynamicity of the boronate ester bonds, although complete stress relaxation is never achieved, suggesting that static **PPGDA** does not allow complete network rearrangement at this level of incorporation, i.e. at 60 mol% and above.

Resistance of materials to creep was investigated at the same temperature, by applying a constant stress of 0.025 MPa (**Figure 4b**). The applied stress value was selected based on the results of stress relaxation experiments to ensure that the instantaneous deformation for all materials remained within the range of 0.01 % to 0.1 %. Creep-recovery tests indicate that instantaneous elastic deformation increases with the molar ratio of **PPGDA** to **DBEDMA**, which correlates with the E' modulus values obtained through DMA. Furthermore, **DBEDMA**-rich materials exhibit a greater increase in deformation with time under stress, suggesting that boronate ester metathesis facilitates further deformation through network topological reorganization.

A similar behavior was observed during the recovery phase, where the original dimensions are immediately restored in the **100**PPGDA formulation, while recovery is delayed in samples containing **DBEDMA**. In the case of the **100**PPGDA formulation, the recovery phase is characterized by a complete restoration of the applied deformation, confirming a more elastic behavior given by a defined and static macromolecular structure, while a low residual strain is observed for materials incorporating the **DBEDMA** cross-linker, indicating a viscous flow in the material compatible with the structural adaptation of the boronate functionalities to the applied stress. This indicates that creep in 3D-printed materials is likely to be a minimal concern.

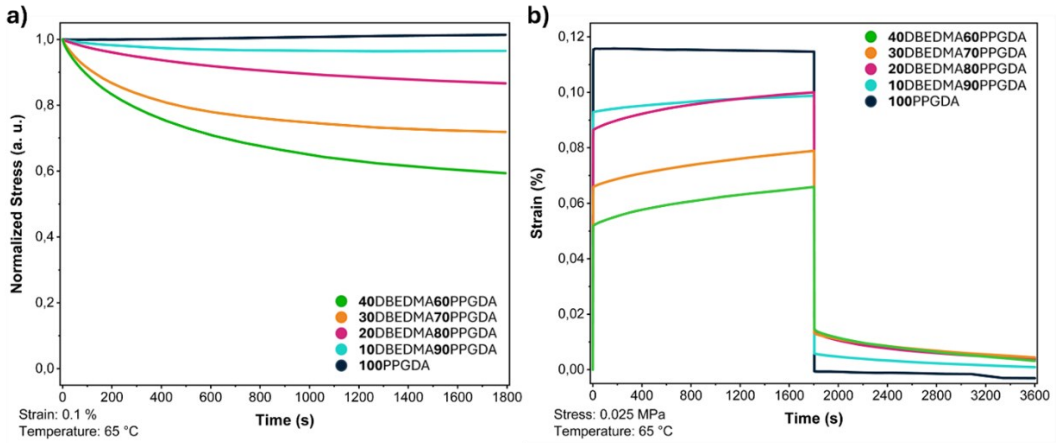

Figure 4. a) Normalized stress relaxation, **b)** and creep recovery studies conducted on photocured materials.

1.2.3 VP 3D printing

Among the photoresin formulations studied, **40**DBEDMA**60**PPGDA demonstrated an optimal balance, requiring a moderate amount of synthetic **DBEDMA** while effectively relieving applied stress through topological rearrangement. Due to these advantages, this formulation was selected for further 3D printing tests to produce tensile specimens for comparing the mechanical isotropy of 3D-printed parts made from **40**DBEDMA**60**PPGDA with those fabricated using the model photoresin **40**BAETDMA**60**PPGDA.

The model photoresin, **40**BAETDMA**60**PPGDA, was specifically designed to closely resemble **40**DBEDMA**60**PPGDA, with the dynamic **DBEDMA** cross-linker replaced by an equivalent molar amount of non-dynamic bisphenol A ethoxylate dimethacrylate (**BAETDMA**) (see molecular structures and formulation details in **Figure 1a** and **Table 1**). **BAETDMA** was chosen for its structural similarity to **DBEDMA**, as both feature a central rigid aromatic core with two flexible side chains terminated by methacrylate groups. The molar mass of **BAETDMA**, determined by ^{1}H NMR analysis (**Figure A1.7**, using **Equations A1.3-A1.4**), is 498 g/mol, which is nearly identical to that calculated for **DBEDMA** (498.19 g/mol). These similarities are expected to result in comparable

photocuring kinetics and mechanical properties for both **40**DBEDMA**60**PPGDA and **40**BAETDMA**60**PPGDA.

Tensile test specimens were 3D printed from both photoresins in two orientations: at 0° and 90° relative to the printing base (as shown in **Figure A1.13**). The printing process involved sequential irradiation of 0.07 mm-thick layers, each exposed for 15 s.

In **VP** 3D printing, it is common practice to retain some unreacted functional groups in freshly printed (commonly referred as "green") samples, which can then react during post-curing to improve layer adhesion and material isotropy.

FTIR analyses (**Figures A1.14-A1.15**) confirmed the presence of a moderate amount of unreacted (meth)acrylate groups in the green tensile specimens (**Figures 5a-5b**). Post-curing under conditions similar to those used for photocuring in a mold (365 nm monochromatic lamp, 55 mW/cm², 5 min) resulted in a noticeable amount of still unreacted functional groups. However, an alternative post-curing method, using a 405 nm monochromatic lamp for 60 min combined with heating at 80 °C, resulted in a more efficient conversion of the remaining reactive groups, as evidenced by a dramatic change in the color of the samples (**Figure 5c**). Furthermore, thermal treatment is expected to enhance the rate of boronate ester metathesis, facilitating topological rearrangement. The remaining unreacted functional groups were quantified via FTIR spectroscopy using specimens from the model photoresin **40**BAETDMA**60**PPGDA, whose spectra allow for easier interpretation (see FTIR spectra in **Figures A1.14-A1.15**).

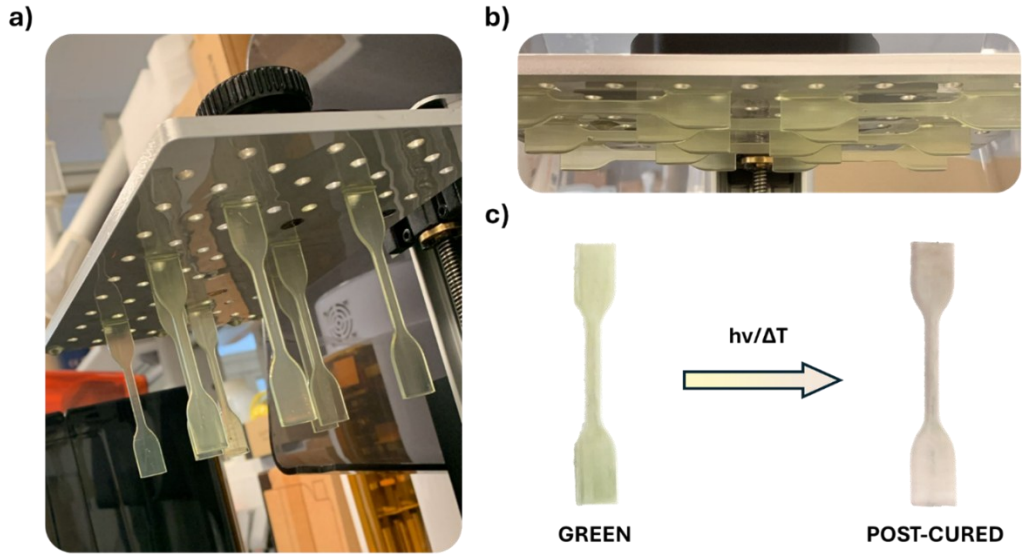

Figure 5. Images of the freshly prepared tensile test specimens **a)** printed at 90°, and **b)** 0° orientations, and **c)** color change of green specimens after post-curing.

1.2.4 Tensile tests

Since post-curing processes are widely applied to standard 3D-printed materials, tensile tests were conducted exclusively on post-cured specimens to evaluate the resulting changes in mechanical anisotropy.

Notably, samples printed with the model **40**BAETDMA**60**PPGDA resin exhibited significant differences in tensile tests when comparing samples oriented at 90° to those oriented at 0°. In contrast, samples printed with **40**DBEDMA**60**PPGDA demonstrated more consistent behavior (**Figure 6a**).

Additionally, the results indicate that samples prepared from **40**DBEDMA**60**PPGDA photoresin exhibit lower Young's modulus but greater toughness than specimens printed with **40**BAETDMA**60**PPGDA in the same orientation (**Figures 6b-6e**). This difference can be attributed to the presence of **DBEDMA**, which enables partial topological rearrangement of the polymeric network under applied stress, as confirmed by stress relaxation tests. This rearrangement, which occurs rapidly even at room temperature and with kinetics compatible

with tensile test experiments, is responsible for the increased energy dissipation observed during tensile loading.

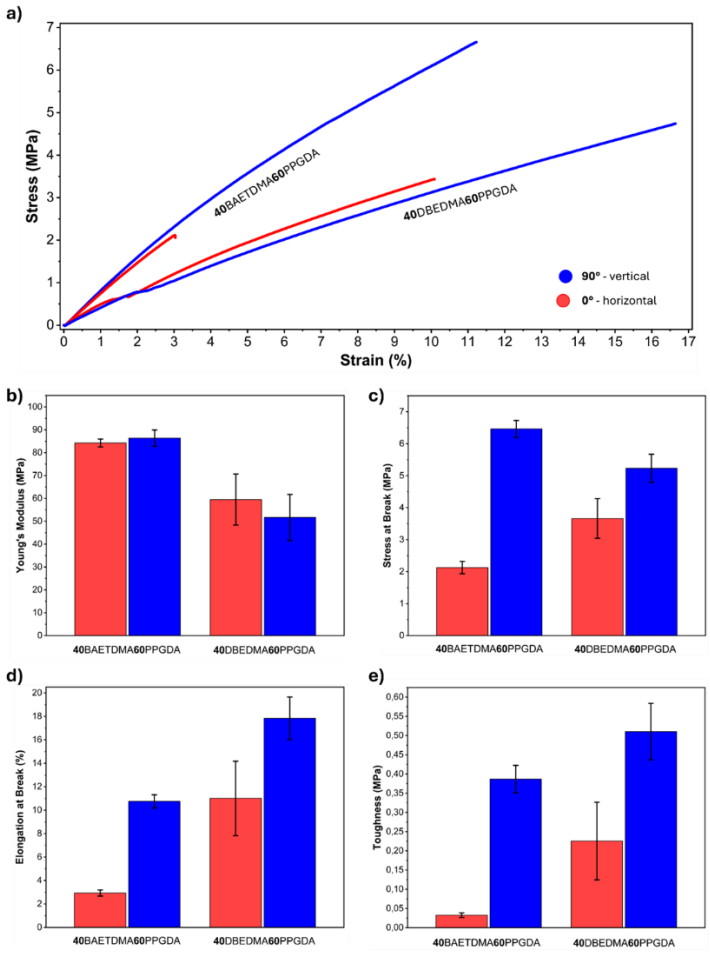

Figure 6. a) Comparison of representative stress-strain curves for tensile specimens printed with **40**BAETDMA**60**PPGDA and **40**DBEDMA**60**PPGDA in 90° (blue) and 0° (red) orientations. Comparison of **b)** Young's modulus, **c)** stress at break, **d)** elongation at break, **e)** and toughness for tensile specimens printed with **40**BAETDMA**60**PPGDA and **40**DBEDMA**60**PPGDA in 90° (blue) and 0° (red) orientations.

The parameters exhibiting the greatest variation in materials synthesized with **40**BAETDMA**60**PPGDA are stress at break, elongation at break, and consequently

toughness. Specifically, the 90° oriented samples exhibited stress and elongation at break values approximately 3 to 4 times greater than those of the 0° samples (**Figures 6c-6d**), while their toughness was nearly 12 times higher (**Figure 7**). Conversely, no significant difference in Young's modulus was observed between the two orientations.

This disparity may be attributed to differences in internal stress accumulation within the printed specimens, which increases with larger layer surface areas due to greater shrinkage during photopolymerization. Shrinkage during photopolymerization creates internal stresses that make the material susceptible to warping as it tries to relieve these stresses.[45] Specimens printed in the 0° orientation have fewer layers, but each with a larger surface area, compared to those printed in the 90° orientation. Considering that the curl deformation is proportional to the length of the raster pattern,[46] this configuration leads to a greater accumulation of internal stresses, which consequently results in reduced toughness and lower mechanical performance at failure.

Similar behaviors were observed in the specimens printed with the **40**DBEDMA**60**PPGDA photoresin. However, in this case, the increases in stress at break, elongation at break, and toughness for the 90° samples compared to the 0° samples are significantly less pronounced. Specifically, the stress and elongation at break values for the 90° samples are approximately 1.5 times higher, while toughness is only doubled (**Figure 7**). As with the previous photoresin, no significant differences in Young's modulus were found between the two orientations.

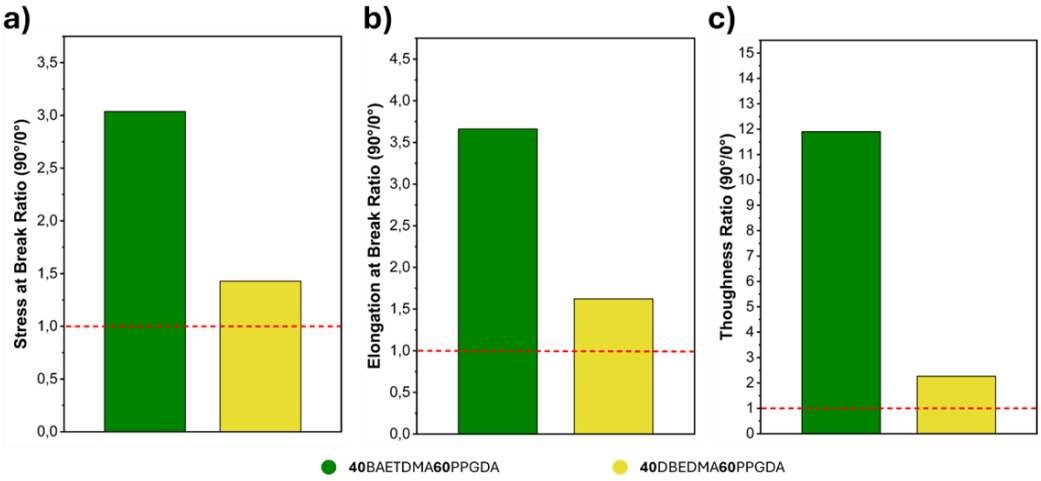

Figure 7. Plotted ratios of **a)** stress at break, **b)** elongation at break, **c)** and toughness for samples printed at 90° relative to those printed at 0°.

The specimens printed with the 40DBEDMA60PPGDA photoresin cannot be considered fully isotropic, as the measured parameter values for the 90° and 0° samples do not fall within the margin of error. This limitation is attributed to the substantial degree of static cross-linking, which significantly constrains the topological rearrangement permitted by the dynamic cross-linker. Nevertheless, the enhancements in mechanical anisotropy are remarkable in comparison to a fully static network.

1.2.5 Surface morphology observation via optical microscopy

Optical microscopy images of samples 3D-printed with **40**BAETDMA**60**PPGDA photoresin reveal a characteristic grid pattern often observed in VP 3D-printed materials,[48] with each repetitive unit of the grid displaying a parabolic-shaped motif (see **Figure 8a**). This pattern forms during the layer-by-layer curing process intrinsic to VP 3D printing. Each layer is cured individually and sequentially by the two-dimensional array of square pixels on the LCD screen, with each pixel contributing to a single parabolic-shaped motif.[47] The images clearly show that the surface pattern is more pronounced in samples obtained from static **40**BAETDMA**60**PPGDA, whereas samples produced from the partially dynamic

40DBEDMA**60**PPGDA photoresin exhibit a smoother, yet still distinct, surface pattern, suggesting partial network rearrangement (see **Figure 8b**). These observations are consistent with tensile test results. The attenuation of the surface pattern is associated with material homogenization, resulting from partial topological rearrangement and leading to reduced mechanical anisotropy.

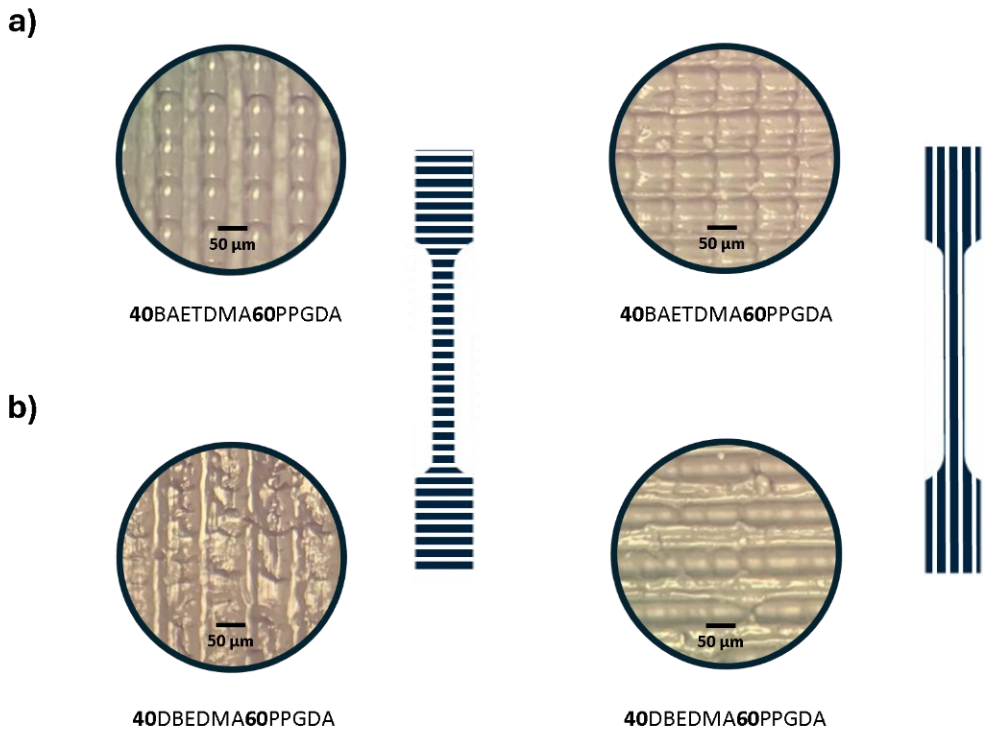

Figure 8. Optical microscopy images of post-cured 3D-printed samples using **a)** **40**BAETDMA**60**PPGDA, **b)** and **40**DBEDMA**60**PPGDA, shown in both 90° (left) and 0° (right) orientations.

1.3 Conclusions

In conclusion, this study demonstrates the successful incorporation of dynamic boronate ester cross-links into photoresins that undergo free radical polymerization of

(meth)acrylates, enabling their use in VP 3D printing applications. The photoresins exhibited rapid photocuring kinetics, with the curing rate increasing as the molar percentage of acrylates to methacrylates increased. The photopolymerized materials exhibited a remarkable ability to relax some of the applied stress while maintaining resistance to creep, indicating that 3D-printed objects exhibit dimensional stability despite the presence of dynamic boronate ester cross-links in their structure. Additionally, the materials showed a significant reduction in the mechanical anisotropy typically observed in 3D-printed structures, although they are not yet fully classified as isotropic. The reduction in mechanical anisotropy can be attributed to the partial topological rearrangement enabled by boronate ester metathesis. This rearrangement is further supported by the partial surface smoothing as observed via optical microscopy. These findings highlight the potential of dynamic boronate esters to enhance the performance of 3D-printed materials, paving the way for further advancements in the design and fabrication of high-performance polymer networks.

ACKNOWLEDGMENTS

Special thanks to Prof. Renaud Nicolaÿ from ESPCI Paris. Thanks to Gabriele Drago from Elantas EUROPE, Quattordio (Alessandria) for the help with the photorheology analyses. Thanks to Elena Saccani, Dr Corrado Sciancalepore and Prof Daniel Milanese from University of Parma for the help with 3D printing and tensile testing.

1.4 Experimental section

MATERIALS

The chemicals used for the synthesis were purchased from TCI, Sigma Aldrich, Fisher, Alfa Aesar, and Acros Organics, and all reagents and solvents were used as received without further purification.

Poly(propylene glycol) diacrylate (**PPGDA**) with a reported average number of propylene glycol repeating units of 12 was purchased from TCI. Bisphenol A ethoxylate dimethacrylate (**BAETDMA**) was kindly provided by Elantas EUROPE S.r.l. (Collecchio, PR, Italy).

SYNTHESIS OF DIBORONATE ESTER DIMETHACRYLATE (DBEDMA)

4,5-Dihydroxypentyl methacrylate (compound **C** in **Scheme S1**), a key precursor for the synthesis of **DBEDMA**, was synthesized following the procedures outlined in the literature.[34]

DBEDMA was synthesized by reacting 1,4-phenylenediboronic acid (13.3 g, 80.0 mmol) with compound **C** (34.0 g, 168 mmol) in THF (173 mL) and water (0.54 mL). The mixture was stirred at room temperature for 10 min before adding anhydrous $MgSO_4$ (57.8 g, 480 mmol). Stirring continued for 5 h at room temperature. The reaction mixture was then filtered, and the filtrate concentrated under reduced pressure, yielding **DBEDMA** as an orange oil (37.9 g, 76.1 mmol, 95 % yield).

PREPARATION, PHOTOCURING, 3D PRINTING AND POST-CURING OF PHOTORESINS

Photocurable formulations were prepared by mixing all the components in a light-protected container. All the mixtures were stirred for a minimum of 7 h while ensuring complete dissolution of the photo initiator.

Samples of photocured material used for Thermogravimetric Analysis (TGA), Differential Scanning Calorimetry (DSC), and Dynamic Mechanical Analysis (DMA) were prepared by irradiating a mold filled with the photocurable formulation for 5 min. The irradiation was

carried out using a UV CHAMBER™ from AMS Technologies, equipped with a 365 nm monochromatic LED lamp that provided a power density of 55 mW/cm².

3D printing was performed using a Kentstrapper Aura stereolithography printer, which features a 4K UV LCD screen emitting monochromatic light at a wavelength of 405 nm. 3D printed tensile test samples were prepared in accordance with ISO 527-2, type 5A standards. All specimens were prepared with a printing speed of 15 s per layer, and with a layer thickness of 0.07 mm.

The post-curing of the 3D-printed specimens was performed using either a 365 nm monochromatic LED lamp from PHOTOELECTRONICS delivering a power density of 55 mW/cm², or a Formlabs Form Cure, which has 13 LEDs with a power output of 39 W each and a wavelength of 405 nm.

CHARACTERIZATIONS

NMR spectra, including ^{1}H, COSY, ^{13}C DEPT135, and HSQC, were recorded on a Bruker AVANCE 400 MHz or on a Jeol 600 MHz spectrometer using $CDCl_3$ as the solvent.

Photo rheology experiments were performed using an Anton Paar MCR 102 rheometer. The device was equipped with an Omnicure Series 1500 lamp, which emits light in the 320–480 nm range. The power density at a wavelength of 365 nm was 5 mW/cm². The experiments were conducted in air using an 8 mm disposable parallel plate geometry made of quartz glass, with a frequency of 1 Hz and a shear strain of 0.1 %.

TGA was performed using a SETARAM THEMYS ONE instrument under a nitrogen atmosphere, with a heating rate of 10 °C/min.

DSC analyses were performed using a DSC250 instrument from the Discovery Series by TA Instruments, under air atmosphere, with a heating rate of 20 °C/min.

Images of the surface morphology of the 3D-printed specimens were captured using a Zeiss Axioskop optical microscope at 10x magnification.

DMA (1 Hz, 0.1 % strain, heating rate of 3°C/min), creep recovery and stress-relaxation analyses were conducted using a DMA Q800 instrument from TA Instruments.

Fourier transform infrared (FT-IR) spectroscopy **was performed** using Bruker FTIR LUMOS.

The tensile tests were carried out using the TesT GmbH model 112 servomechanical machine in displacement control mode with a deformation rate of 1 mm/min.

1.5 Appendix information

DIBORONATE ESTER DIMETHACRYLATE (DBEDMA) SYNTHESIS

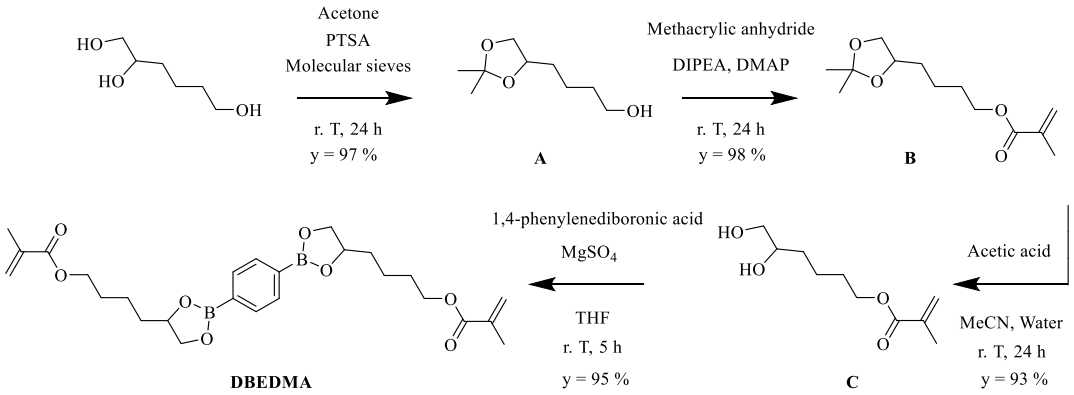

Scheme A1.1. Synthetic pathway for **DBEDMA**.

All chemical shifts (δ) are reported in parts per million (ppm), referenced either to the residual proton resonances from incomplete deuteration of the NMR solvents or to the solvent's ^{13}C resonance. The abbreviations: s, d, t and m indicated the spectrum peaks referred to: singlet, doublet, triplet and multiplet, respectively. The coupling constant (J) are expressed in Hz.

Compound **A**

p-Toluenesulfonic acid (PTSA, 5.10 g, 29.7 mmol) and 4 Å molecular sieves (5.60 g) were added to a solution of 1,2,6-hexanetriol (40.2 g, 300 mmol) in acetone (560 mL). The reaction mixture was stirred at room temperature for 24 h. After this time, $NaHCO_3$ (4.28 g, 50.9 mmol) was added, and the mixture was stirred for an additional 10 min. The molecular sieves were removed by filtration and the resulting solution was then concentrated under reduced pressure. An excess of water was added, followed by multiple extractions with DCM. The combined organic layers were collected and concentrated under reduced pressure, yielding compound **A** as a pale-yellow oil (50.9 g, 292 mmol, 97 % yield).

^{1}H NMR ($CDCl_3$, 400 MHz): δ (ppm) = 4.06 (m, 1H, -C**H**-), 4.02 (m, 1H, - $C(CH_3)_2OC\mathbf{H_2}$'CH -), 3.63 (t, J = 6.5 Hz, 2H, $HOC\mathbf{H_2}CH_2$ -), 3.49 (m, 1H, - $C(CH_3)_2COC\mathbf{H_2}$"CH -), 1.56 (bm, 6H, $HOCH_2C\mathbf{H_2}C\mathbf{H_2}C\mathbf{H_2}CH$ -), 1.39 (s, 3H, $C(C\mathbf{H_3}')_2O$ -), 1.33 (s, 3H, $C(C\mathbf{H_3}'')_2O$ -).

Compound **B**

N,N-Diisopropylethylamine (DIPEA, 79.6 mL, 457 mmol) and 4-dimethylaminopyridine (DMAP, 507 mg, 4.15 mmol) were added to intermediate **A** (72.4 g, 415 mmol) under stirring. Methacrylic anhydride (74.2 mL, 498 mmol) was then slowly added dropwise over the course of 1 h. The resulting mixture was stirred at room temperature for 24 h. After this period, MeOH (30 mL, 741 mmol) was added, and the mixture was stirred for 1 h. Hexane was then introduced, and the solution was extracted multiple times with water, followed by a 1 M HCl aqueous solution. The organic layer was collected and concentrated under reduced pressure, yielding compound **B** as a yellow oil (98.7 g, 407 mmol, 98 % yield).

^{1}H NMR ($CDCl_3$, 400 MHz): δ (ppm) = 6.03 (s, 1H, $C\mathbf{H_2}'$=$C(CH_3)$ -), 5.48 (s, 1H, $C\mathbf{H_2}''$=$C(CH_3)$ -), 4.08 (m, 1H, - $C(CH_3)_2OC\mathbf{H_2}'$CH -), 4.08 (t, J = 6.54 Hz, 2H, - $OC\mathbf{H_2}CH_2$ -), 4.02 (m, 1H, - C**H** -), 3.97 (m, 1H, - $C(CH_3)_2OC\mathbf{H_2}'$CH -), 3.44 (m, 1H, - $C(CH_3)_2OC\mathbf{H_2}''$CH -), 1.87 (s, 3H, CH_2=$C(C\mathbf{H_3})$ -), 1.53 (bm, 6H, - $OCH_2C\mathbf{H_2}C\mathbf{H_2}C\mathbf{H_2}CH$ -), 1.39 (s, 3H, $C(C\mathbf{H_3}')_2O$ -), 1.34 (s, 3H, $C(C\mathbf{H_3}'')_2O$ -).

Compound **C**

Acetic acid (54.2 mL, 947 mmol) was added to a solution of intermediate **B** (49.9 g, 206 mmol) dissolved in a mixture of water (250 mL) and MeCN (250 mL). The resulting solution was stirred at room temperature for 24 h. After this period, a large amount of EtOAc was added, and the mixture was extracted multiple times with a 1 M NaOH aqueous solution, followed by water. The organic layer was then collected and concentrated under reduced pressure, yielding compound **C** as a yellow oil (38.7 g, 191 mmol, 93 % yield).

^{1}H NMR ($CDCl_3$, 400 MHz): δ (ppm) = 6.08 (s, 1H, $C\mathbf{H_2}'$=$C(CH_3)$ -), 5.54 (s, 1H, $C\mathbf{H_2}''$=$C(CH_3)$ -), 4.14 (t, J = 6.51 Hz, 2H, - $OC\mathbf{H_2}CH_2$ -), 3.71 (m, 1H, - C**H** -), 3.64 (m, 1H, - $C(CH_3)_2OC\mathbf{H_2}'$CH -), 3.44 (m, 1H, - $C(CH_3)_2OC\mathbf{H_2}''$CH -), 1.92 (s, 3H, CH_2=$C(C\mathbf{H_3})$ -), 1.55 (bm, 6H, - $OCH_2C\mathbf{H_2}C\mathbf{H_2}C\mathbf{H_2}CH$ -).

DBEDMA

1,4-Phenylenediboronic acid (13.3 g, 80.0 mmol) and water (0.54 mL) were added to a solution of compound **C** (34.0 g, 168 mmol) in THF (173 mL). The resulting solution was stirred at room temperature for 10 min. After this time, anhydrous $MgSO_4$ (57.8 g, 480 mmol) was added, and the mixture was stirred for an additional 5 h at room temperature. The reaction mixture was then filtered, and the filtrate was concentrated under reduced pressure, yielding **DBEDMA** as an orange oil (37.9 g, 76.1 mmol, 95 % yield).

^{1}H NMR ($CDCl_3$, 400 MHz): δ (ppm) = 7.81 (s, 4H, Ar**H**), 6.10 (m, 2H, C**H$_2$'**=C(CH_3) -), 5.55 (m, 2H, C**H$_2$"**=C(CH_3) -), 4.59 (m, 2H, - C**H** -), 4.44 (m, 2H, - C(CH_3)$_2$OC**H$_2$'**CH -), 4.18 (t, J = 6.49 Hz, 2H, - OC**H$_2$**CH_2 -), 3.95 (m, 2H, - C(CH_3)$_2$OC**H$_2$"**CH -), 1.94 (s, 6H, CH_2=C(C**H$_3$**) -), 1.65 (bm, 12H, - OCH_2C**H$_2$**C**H$_2$**C**H$_2$**CH -).

DIBORONATE ESTER DIMETHACRYLATE (DBEDMA) NMR CHARACTERIZATION

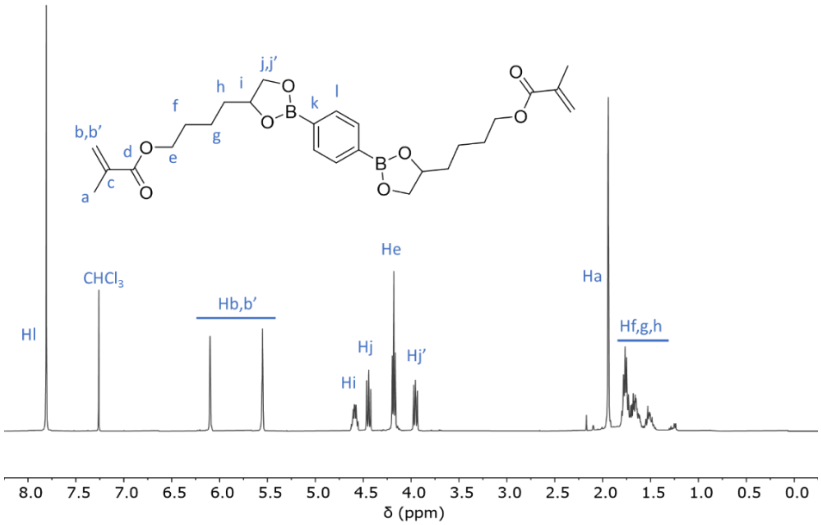

Figure A1.1. ^{1}H NMR of **DBEDMA**, in $CDCl_3$, 400 MHz, 25 °C.

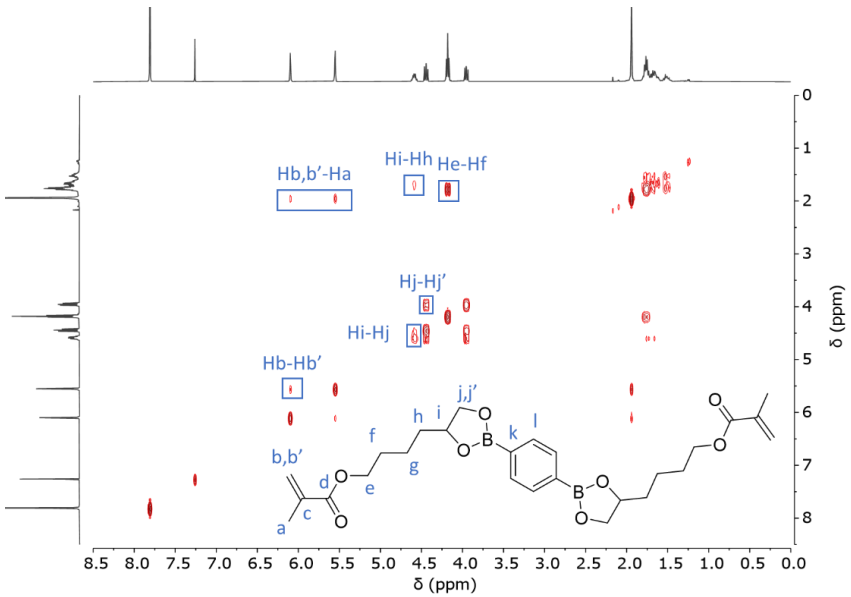

Figure A1.2. COSY NMR of **DBEDMA**, in $CDCl_3$, 400 MHz, 25 °C.

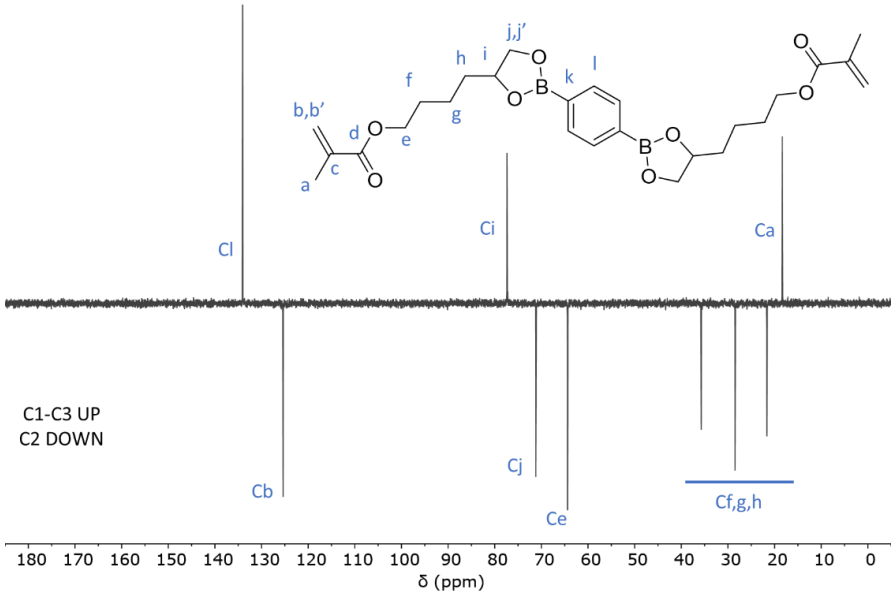

Figure A1.3. ^{13}C DEPT135 NMR of **DBEDMA** (CH_3 and CH up; CH_2 and C down), in $CDCl_3$, 101 MHz, 25 °C.

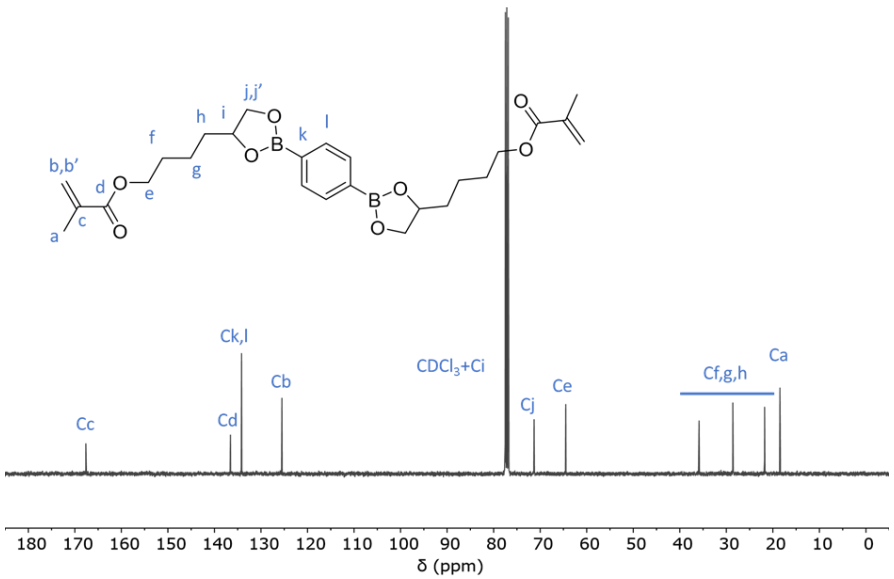

Figure A1.4. ^{13}C NMR of **DBEDMA**, in $CDCl_3$, 101 MHz, 25 °C.

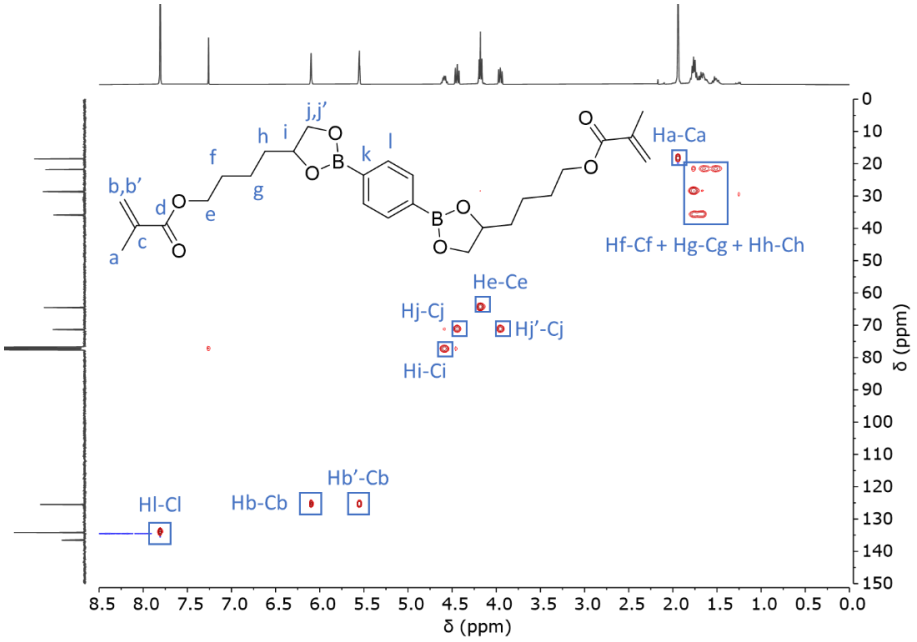

Figure A1.5. HSQC NMR of **DBEDMA**, in $CDCl_3$, 400 MHz, 25 °C.

POLY(PROPYLENE GLYCOL) DIACRYLATE (PPGDA) NMR CHARACTERIZATION AND AVERAGE MOLAR MASS CALCULATION

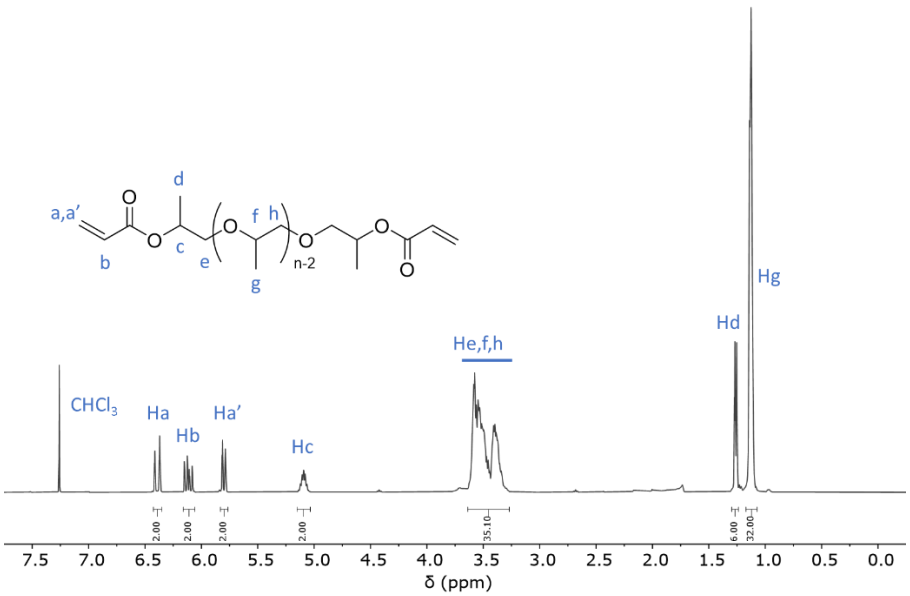

Figure A1.6. ^{1}H NMR of **PPGDA**, in $CDCl_3$, 400 MHz, 25 °C.

$$\mathbf{n} = \frac{\int \mathbf{Hc} + \int \mathbf{He,f,h} + \int \mathbf{Hd} + \int \mathbf{Hg}}{6} = \mathbf{12.52}$$

Equation A1.1. Formula for calculating the average **n** value of **PPGDA**.

$$\mathbf{M_w} = [124.14 + \mathbf{n}\ (58.08)]\ \text{g/mol} = \mathbf{851\ g/mol}$$

Equation A1.2. Formula for calculating the average molecular weight of **PPGDA**.

BISPHENOL A POLYETHYLENE GLYCOL DIACRYLATE (BAETDMA) NMR CHARACTERIZATION AND AVERAGE MOLAR MASS CALCULATION

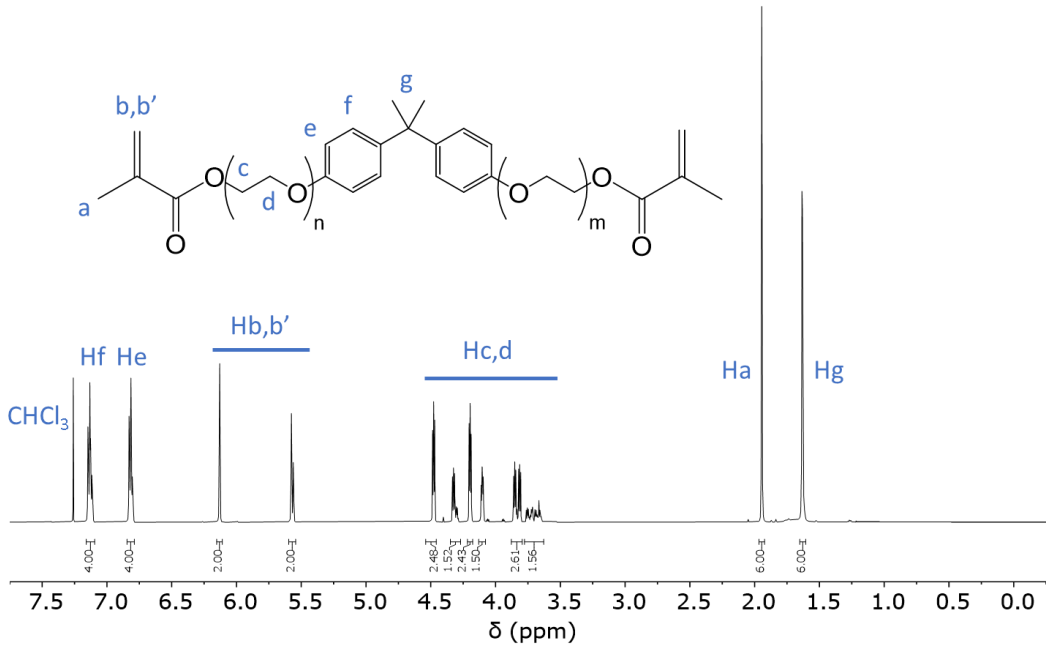

Figure A1.7. ^{1}H NMR of **BAETDMA**, in $CDCl_3$, 600 MHz, 25 °C.

$$(\mathbf{n}+\mathbf{m}) = \frac{\int \mathbf{Hc,d}}{4} = \mathbf{3.03}$$

Equation A1.3. Formula for calculating the average **n + m** value of **BAETDMA**.

$$\mathbf{M_w} = [364.44 + (\mathbf{n}+\mathbf{m})\ (44.05)]\ \mathrm{g/mol} = \mathbf{498\ g/mol}$$

Equation A1.4. Formula for calculating the average molecular weight of **BAETDMA**.

FORMULATION AND PHOTOCURING OF THE RESINS

Formulation	PPGDA	DBEDMA	BAETDMA	BAPO
100PPGDA	11.9 g (14.0 mmol) 100 mol%	/	/	11.8 mg (0.28 mmol) 2 mol%
10DBEDMA**90**PPGDA	10.7 g (12.6 mmol) 90 mol%	0.70 g (1.40 mmol) 10 mol%	/	11.8 mg (0.28 mmol) 2 mol%
20DBEDMA**80**PPGDA	9.52 g (11.2 mmol) 80 mol%	1.40 g (2.80 mmol) 20 mol%	/	11.8 mg (0.28 mmol) 2 mol%
30DBEDMA**70**PPGDA	8.33 g (9.80 mmol) 70 mol%	2.10 g (4.20 mmol) 30 mol%	/	11.8 mg (0.28 mmol) 2 mol%
40DBEDMA**60**PPGDA	7.14 g (8.40 mmol) 60 mol%	2.79 g (5.60 mmol) 40 mol%	/	11.8 mg (0.28 mmol) 2mol%
60DBEDMA**40**PPGDA	4.76 g (5.60 mmol) 40 mol%	4.19 g (8.40 mmol) 60 mol%	/	11.8 mg (0.28 mmol) 2 mol%
80DBEDMA**20**PPGDA	2.38 g (2.80 mmol) 20 mol%	5.58 g (11.2 mmol) 80 mol%	/	11.8 mg (0.28 mmol) 2 mol%
100DBEDMA	/	6.98 g (14.0 mmol) 100 mol%	/	11.8 mg (0.28 mmol) 2 mol%
40BAETDMA**60**PPGDA	7.14 g (8.40 mmol) 60 mol%	/	2.79 g (5.60 mmol) 40 mol%	11.8 mg (0.28 mmol) 2 mol%

Table A1.1. Measured masses and moles of each component used to prepare approximately 10 g of each formulation.

PHOTO RHEOLOGY EXPERIMENTS

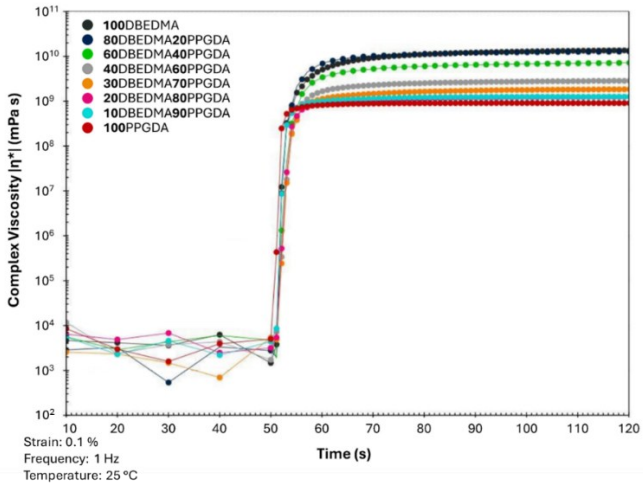

Figure A1.8. Complex viscosity measured before (from 10 s to 50 s) and during (from 50 s to 120 s) UV light exposure of the photocurable formulations.

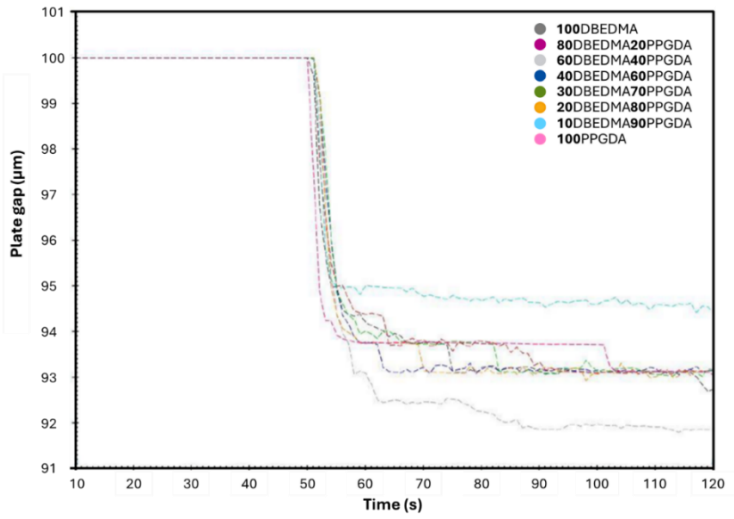

Figure A1.9. Resin shrinkage measured as a reduction in plate gap as result of UV light exposure (from 50 s to 120 s) of the photocurable formulations, while a constant normal force is applied.

THERMOGRAVIMETRIC ANALYSIS (TGA)

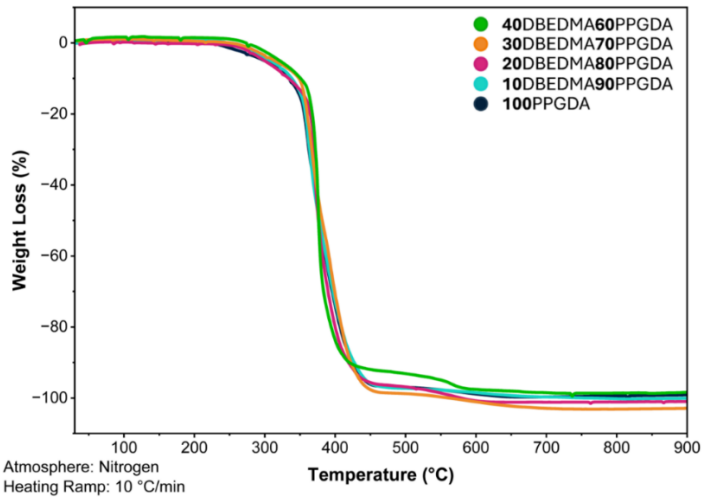

Figure A1.10. Thermogravimetric analysis of the photocured materials.

DYNAMIC MECHANICAL ANALYSIS (DMA)

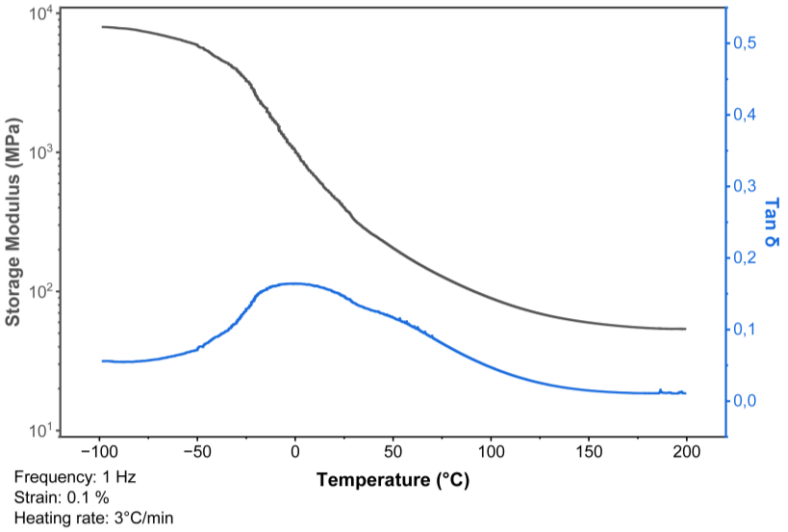

Figure A1.11. Storage modulus and tan δ of photocured **60**DBEDMA**40**PPGDA as function of temperature.

DIFFERENTIAL SCANNING CALORIMETRY (DSC)

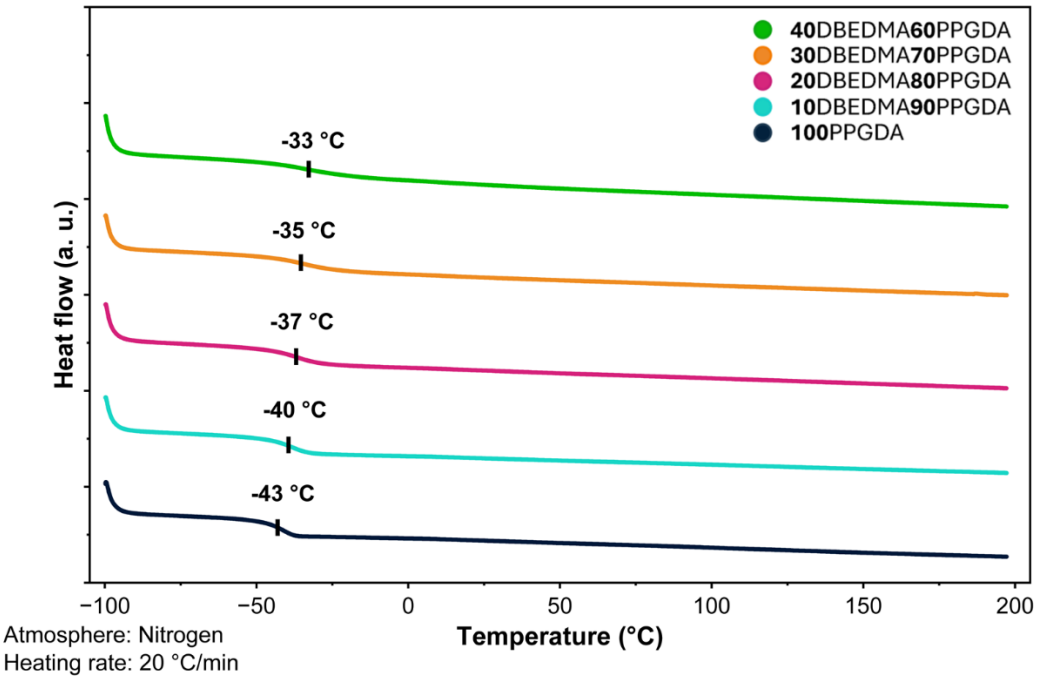

Figure A1.12. Differential scanning calorimetry analysis of the photocured materials.

VP 3D PRINTING AND POST-CURING OF THE SPECIMENS

Both resins, **40**DBEDMA**60**PPGDA and **40**BAETMA**60**PPGDA, were used to 3D print tensile test specimens in two different orientations:

- In the first orientation, the main extension axis is perpendicular to the printing base and parallel to the normal of the sequentially printed layers (90° orientation, **Figure S13a**).
- In the second orientation, the main extension axis is parallel to the printing base and perpendicular to the normal of the material layers (0° orientation, **Figure S13b**).

Eight identical specimens were printed simultaneously in each run, following the arrangements shown below. All the specimens were printed with a layer thickness of 0.07 mm, and each layer was irradiated for a total of 15 s.

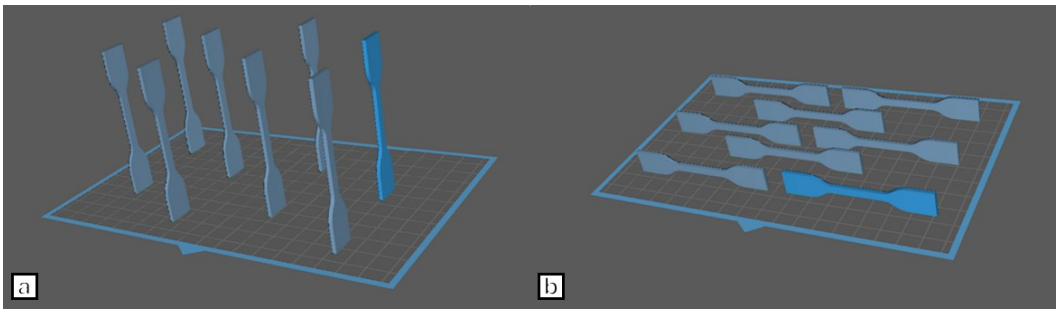

Figure A1.13. Arrangement of the specimens to be printed at angles of **a)** 90° and **b)** 0°, generated using ChiTuBox software.

For each print, 100 g of photocurable formulation, prepared according to the procedure described above, were used.

At the end of the printing process, the samples are carefully removed from the metal plate and washed with abundant MeCN. The solvent is allowed to evaporate for about an hour while keeping the printed objects shielded from light.

The post-curing of the 3D-printed specimens was performed using two alternative methods:

- In the first method, one of the larger flat surfaces of the sample was irradiated for 5 min using monochromatic light at 365 nm with a power density of 55 mW/cm^2.
- In the second method, the samples were first heated to 80 °C, then one of the larger flat surfaces was irradiated with 405 nm monochromatic light for 1 hour, while maintaining the same temperature.

FOURIER TRANSFORM INFRARED SPECTROSCOPY MEASUREMENTS

FTIR spectra in ATR mode were collected for the **40**BAETDMA**60**PPGDA formulation and for the photocured tensile specimens, obtained either by direct photocuring or by 3D printing with eventual post-curing.

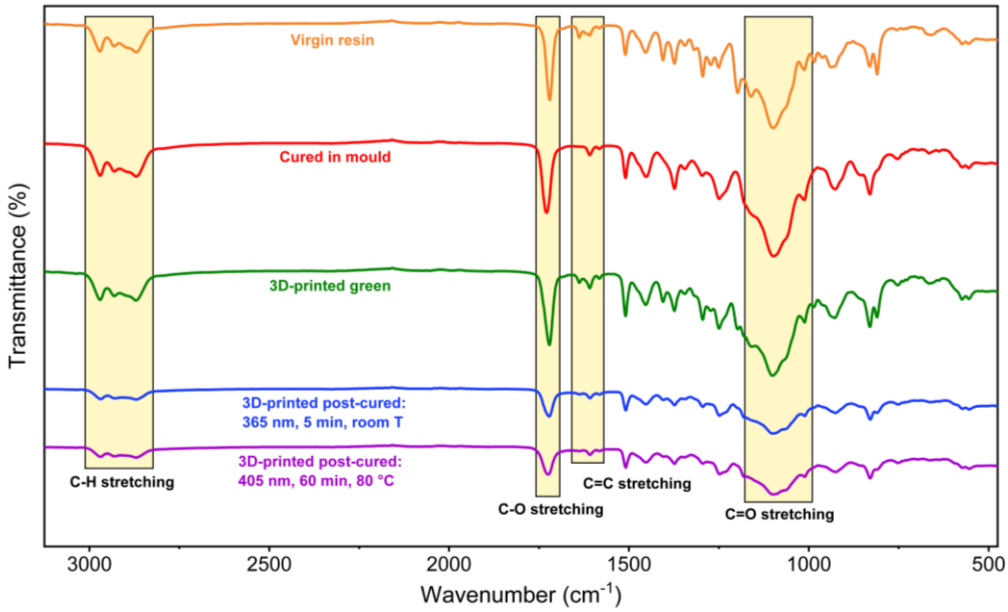

Figure A1.14. FTIR spectra of tensile test specimens, displayed in transmittance as a function of wavenumber.

The collected spectra were then converted to absorbance as a function of wavenumber, and a baseline, calculated using a fifth-degree polynomial, was subtracted.

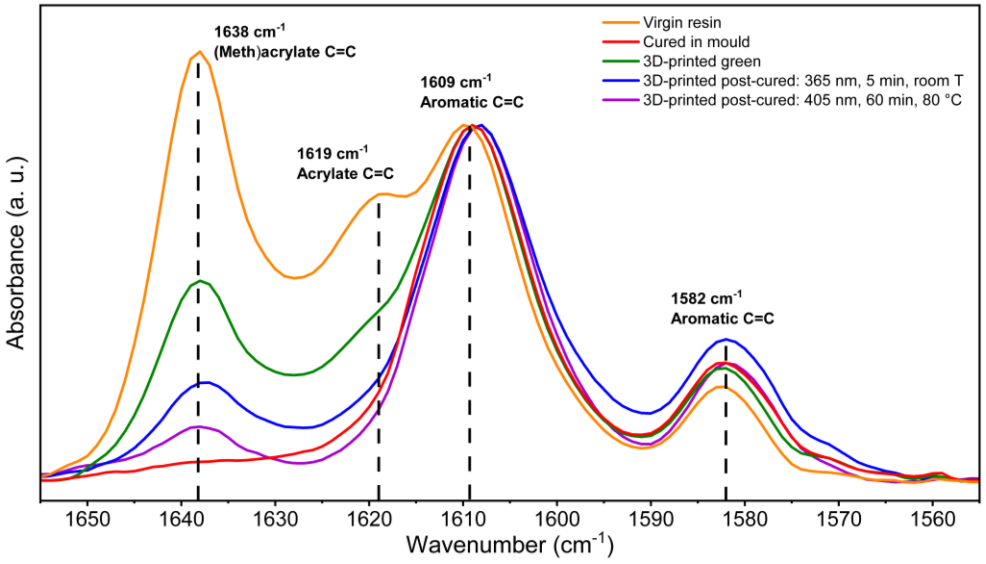

Figure A1.15. FTIR spectra of tensile test specimens, shown as absorbance versus wavenumber, normalized to the 1609 cm^{-1} peak.

TENSILE TESTS

The printed specimens were subjected to mechanical tensile tests using a dynamometer. For each sample, the thickness and width of the central section, as well as the distance between the grips holding the specimen in the dynamometer, were initially measured.

The tensile tests were conducted by applying a pre-tension of up to 2 N at a speed of 5 mm/min, while the actual test was carried out at a tensioning speed of 1 mm/min.

The acquired data were processed into stress-strain curves, from which the toughness, Young's modulus, and the stress and strain at break were calculated for the specimens.

Three replicates of each measurement were taken.

1.6 References

(1) X. Wang, M. Jiang, Z. Zhou, J. Gou, D. Hui, 3D printing of polymer matrix composites: A review and prospective, *Compos. B Eng.* **2017**, *110*, 442-458, https://doi.org/10.1016/j.compositesb.2016.11.034.

(2) J. C. Najmon, S. Raeisi, A. Tovar, (**2019**) Review of additive manufacturing technologies and applications in the aerospace industry, Elsevier.

(3) S. C. Joshi, A. A. Sheikh, 3D printing in aerospace and its long-term sustainability, *Virtual Phys. Prototyp.* **2015**, *10*, 175−185, https://doi.org/10.1080/17452759.2015.1111519.

(4) M. P. Browne, E. Redondo, M. Pumera, 3D Printing for Electrochemical Energy Applications, *Chem. Rev.* **2020**, *120*, 2783−2810, https://doi.org/10.1021/acs.chemrev.9b00783.

(5) Y. W. D. Tay, B. Panda, S. C. Paul, N. A. Noor Mohamed, M. J. Tan, K. F. Leong, 3D printing trends in building and construction industry: a review, *Virtual Phys. Prototyp.* **2017**, *12*, 261−276, https://doi.org/10.1080/17452759.2017.1326724.

(6) F. Rengier, A. Mehndiratta, H. Von Tengg-Kobligk, C. Zechmann, R. Unterhinninghofen, H. U. Kauczor, F. Giesel, 3D printing based on imaging data: review of medical applications, *Int. J. CARS* **2010**, *5*, 335–341, https://doi.org/10.1007/s11548-010-0476-x.

(7) S. M. Peltola, F. P. Melchels, D. W. M. Grijpma, Kellomäki, A review of rapid prototyping techniques for tissue engineering purposes, *Ann. Med.* **2008**, *40*, 268-280, https://doi.org/10.1080/07853890701881788.

(8) S. V. Murphy, A. Atala, 3D bioprinting of tissues and organs, *Nat. Biotechnol.* **2014**, *32*, 773−785, https://doi.org/10.1038/nbt.2958.

(9) W. Zhu, X. Ma, M. Gou, D. Mei, K. Zhang, S. Chen, 3D printing of functional biomaterials for tissue engineering, *Curr. Opin. Biotechnol.* **2016**, *40*, 103−112, https://doi.org/10.1016/j.copbio.2016.03.014.

(10) Q. Yan, H. Dong, J. Su, J. Han, B. Song, Q. Wei, Y. Shi, A review of 3D printing technology for medical applications, *Engineering* **2018**, *4*, 729−742, https://doi.org/10.1016/j.eng.2018.07.021.

(11) M. S. Mannoor, Z. Jiang, T. James, Y. L. Kong, K. A. Malatesta, W. O. Soboyejo, N. Verma, D. H. Gracias, M. C. McAlpine, 3D printed bionic ears, *Nano Lett.* **2013**, *13*, 2634−2639, https://doi.org/10.1021/nl4007744.

(12) N. W. Bartlett, M. T. Tolley, J. T. B. Overvelde, J. C. Weaver, B. Mosadegh, K. Bertoldi, G. M. Whitesides, R. J. Wood, A 3D-printed, functionally graded soft robot powered by combustion, *Science* **2015**, *349*, 161−165, https://doi.org/10.1126/science.aab012.

(13) M. Wehner, R. L. Truby, D. J. Fitzgerald, B. Mosadegh, G. M. Whitesides, J. A. Lewis, R. J. Wood, An integrated design and fabrication strategy for entirely soft, autonomous robots, *Nature* **2016**, *536*, 451, https://doi.org/10.1038/nature19100.

(14) T. Gissibl, S. Thiele, A. Herkommer, H. Giessen, Two-photon direct laser writing of ultracompact multi-lens objectives, *Nat. Photonics* **2016**, *10*, 554, https://doi.org/10.1038/nphoton.2016.121.

(15) Y. L. Kong, M. K. Gupta, B. N. Johnson, M. C. McAlpine, 3D printed bionic nanodevices, *Nano Today* **2016**, *11*, 330−350, https://doi.org/10.1016/j.nantod.2016.04.007.
(16) X. Zhou, C.-J. Liu, Three-dimensional printing for catalytic applications: current status and perspectives, *Adv. Funct. Mater.* **2017**, *27*, 1701134, https://doi.org/10.1002/adfm.201701134.
(17) S.-Z. Guo, K. Qiu, F. Meng, S. H. Park, M. C. McAlpine, 3D printed stretchable tactile sensors, *Adv. Mater.* **2017**, *29*, 1701218, https://doi.org/10.1002/adma.201701218.
(18) R. L. Truby, J. A. Lewis, Printing soft matter in three dimensions, *Nature* **2016**, *540*, 371−378, https://doi.org/10.1038/nature21003.
(19) S. C. Ligon, R. Liska, J. Stampfl, M. Gurr, R. Muelhaupt, Polymers for 3D printing and customized additive manufacturing, *Chem. Rev.* **2017**, *117*, 10212−10290, https://doi.org/10.1021/acs.chemrev.7b00074.
(20) M. Manoj Prabhakar, A. K. Saravanan, A. Haiter Lenin, I. Jerin leno, K. Mayandi, P. Sethu Ramalingam, A short review on 3D printing methods, process parameters and materials, *Mater. Today* **2021**, *45*, 6108-6114, https://doi.org/10.1016/j.matpr.2020.10.225.
(21) H. Quan, T. Zhang, H. Xu, S. Luo, J. Nie, X. Zhu, Photo-curing 3D printing technique and its challenges, *Bioact. Mater.* **2020**, *5*, 110-115, https://doi.org/10.1016/j.bioactmat.2019.12.003.
(22) R. Janusziewicz, J. R. Tumbleston, A. L. Quintanilla, S. J. Mecham, J. M. DeSimone, Layerless fabrication with continuous liquid interface production, *PNAS* **2016**, *113*, 11703–11708, https://doi.org/10.1073/pnas.1605271113.
(23) M. Monzón, Z. Ortega, A. Hernández, R. Paz, F. Ortega, Anisotropy of photopolymer parts made by digital light processing, *Materials* **2017**, *10*, 64, https://doi.org/10.3390/ma10010064.
(24) R. Quintana, J.-W. Choi, K. Puebla, R. WickerInt, Effects of build orientation on tensile strength for stereolithography-manufactured ASTM D-638 type I specimens, *J. Adv. Manuf. Technol.* **2010**, *46*, 201–215, https://doi.org/10.1007/s00170-009-2066-z.
(25) K. Puebla, K. Arcaute, R. Quintana, R. B. Wicker, Effects of environmental conditions, aging, and build orientations on the mechanical properties of ASTM type I specimens manufactured via stereolithography, *Rapid Prototyp. J.* **2012**, *12*, 374–388, https://doi.org/10.1108/13552541211250373
(26) J.-Y. Lee, J. An, C. K. Chua, Fundamentals and applications of 3D printing for novel materials *Appl. Mater. Today* **2017**, *7*, 120-133, https://doi.org/10.1016/j.apmt.2017.02.004.
(27) L. Strohmeier, H. Frommwalda, S. Schlögl, Digital light processing 3D printing of modified liquid isoprene rubber using thiol-click chemistry, *RSC Adv.* **2020**, *40*, 23607-23614, https://doi.org/10.1039/D0RA04186F.
(28) L. Pezzana, R. Wolff, G. Melilli, N. Guigo, N. Sbirrazzuoli, J. Stampfl, R. Liska, M. Sangermano, Hot-lithography 3D printing of biobased epoxy resins, *Polymer* **2022**, *254*, 125097, https://doi.org/10.1016/j.polymer.2022.125097.
(29) H. Gao, Y. Sun, M. Wang, Z. Wang, G. Han, L. Jin, P. Lin, Y. Xia, K. Zhang, Mechanically robust and reprocessable acrylate vitrimers with hydrogen-bond-

integrated networks for photo-3D printing, *ACS Appl. Mater. Interfaces* **2021**, *13*, 1581−1591, https://doi.org/10.1021/acsami.0c19520.

(30) E. Rossegger, R. Höller, D. Reisinger, J. Strasser, M. Fleisch, T. Griesserb, S. Schlögl, Digital light processing 3D printing with thiol–acrylate vitrimers, *Polym. Chem.* **2021**,*12*, 639-644, DOI https://doi.org/10.1039/D0PY01520B.

(31) X. Li, R. Yu, Y. He, Y. Zhang, X. Yang X. Zhao, W. Huang, Self-healing polyurethane elastomers based on a disulfide bond by digital light processing 3D printing, *ACS Macro Lett.* **2019**, *8*, 11, 1511–1516, https://doi.org/10.1021/acsmacrolett.9b00766.

(32) S. Wang, J. Yin, W. Huang, J. Ye, H. Deng, J. Huang, S. Wang, X. Liu, H. Xiang, UV-induced disulfide metathesis: Strengthening interlayer adhesion and rectifying warped 3D printed materials, *Addit. Manuf.* **2022**, *59*, 103085, https://doi.org/10.1016/j.addma.2022.103085.

(33) A. Vilanova-Pérez, S. De la Flor, X. Fernández-Francos, À. Serra, A. Roig, Biobased Imine Vitrimers Obtained by Photo and Thermal Curing Procedures─ Promising Materials for 3D Printing, *ACS Appl. Polym. Mater.* **2024**, *6*, 3364-3372, https://doi.org/10.1021/acsapm.3c03234.

(34) M. Rottger, T. Domenech, R. van der Weegen, A. Breuillac, R. Nicolaÿ, L. Leibler, High-performance vitrimers from commodity thermoplastics through dioxaborolane metathesis, *Science* **2017**, *356*, 62−65, https://doi.org/10.1126/science.aah5281.

(35) O. R. Cromwell, J. Chung, Z. Guan, Malleable and self-healing covalent polymer networks through tunable dynamic boronic ester bonds, *J. Am. Chem. Soc.* **2015**, *137*, 6492−6495, https://doi.org/10.1021/jacs.5b03551.

(36) A. Breuillac, A. Kassalias, R. Nicolaÿ, Polybutadiene vitrimers based on dioxaborolane chemistry and dual networks with static and dynamic cross-links, *Macromolecules* **2019**, *52*, 7102−7113, https://doi.org/10.1021/acs.macromol.9b01288.

(37) F. Meng, M. O. Saed, E. M. Terentjev, Elasticity and relaxation in full and partial vitrimer networks, *Macromolecules* **2019**, *52*, 7423−7429, https://doi.org/10.1021/acs.macromol.9b01123.

(38) Y. Ding, R. Miao, J. Liu, Z. Xin, C. Bao, Covalent Adaptable Networks Containing Nitrogen-Coordinated Boronic Ester and Imine Bonds, *ACS Appl. Polym. Mater.* **2024**, *6*, 9008-9016, https://doi.org/10.1021/acsapm.4c01334.

(39) Y. Zeng, S. Liu, X. Xu, Y. Chen, F. Zhang, Fabrication and curing properties of o-cresol formaldehyde epoxy resin with reversible cross-links by dynamic boronic ester bonds, *Polymer* **2020**, *211*, 123116, https://doi.org/10.1016/j.polymer.2020.123116.

(40) J. J. Cash, T. Kubo, A. P. Bapat, B. S. Sumerlin, Room-temperature self-healing polymers based on dynamic-covalent boronic esters, *Macromolecules* **2015**, *48*, 2098−2106, https://doi.org/10.1021/acs.macromol.5b00210.

(41) J. J. Cash, T. Kubo, D. J. Dobbins, B. S. Sumerlin, Maximizing the symbiosis of static and dynamic bonds in self-healing boronic ester networks, *Polym. Chem.* **2018**, *9*, 2011−2020, https://doi.org/10.1039/C8PY00123E.

(42) L. L. Robinson, J. L. Self, A. D. Fusi, M. W. Bates, J. Read de Alaniz, C. J. Hawker, C. M. Bates, C. S. Sample, Chemical and mechanical tunability of 3D-

printed dynamic covalent networks based on boronate esters, *ACS Macro Lett.* **2021**, *10*, 857−863, https://doi.org/10.1021/acsmacrolett.1c00257.

(43) L. Sinawehl, R. Wolff, T. Koch, J. Stampfl, R. Liska, S. Baudis, Photopolymers based on boronic esters for the enhanced degradation of 3D-printed scaffolds, *Polym. Chem.* **2018**, *9*, 2011−2020, https://doi.org/10.1021/acsapm.3c01000.

(44) C. Schmidt, T. Scherzer, Monitoring of the shrinkage during the photopolymerization of acrylates using hyphenated photorheometry/near-infrared spectroscopy, *J. Polym. Sci., Part B: Polym. Phys.* **2015**, *53*, 729–739, https://doi.org/10.1002/polb.23694.

(45) C. Schmutzler, T. H. Stiehl, M. F. Zaeh, Empirical process model for shrinkage-induced warpage in 3D printing, *Rapid Prototyp. J.* **2019**, *25*, 721-727, https://doi.org/10.1108/RPJ-04-20180098.

(46) Y.-M. Huang, C.-P. Jiang, Curl Distortion Analysis During Photopolymerisation of Stereolithography Using Dynamic Finite Element Method, *J. Adv. Manuf. Technol.* **2003**, *21*, 586–595, https://doi.org/10.1007/s00170-002-1317-z.

(47) G. V. Salmoria, C. H.Ahrens, V. E. Beal, A. T. N. Pires, V. Soldi, Evaluation of post-curing and laser manufacturing parameters on the properties of SOMOS 7110 photosensitive resin used in stereolithography, *Mater. Des.* **2009**, *30*, 758–763, https://doi.org/10.1016/j.matdes.2008.05.016.

Chapter 2

"Photocurable Isosorbide-Based Water Disintegrable Interpenetrating Polymer Networks"

This study was conducted as part of the internship at Elantas EUROPE, Collecchio (Parma).

2.1 Introduction

Isosorbide is a promising next-generation raw material derived from polysaccharides-rich biomass. It is a water-soluble biheterocyclic diol obtained from the dehydration reaction of sorbitol[1,2], a polyol derived from glucose hydrogenation[3-5] (**Figure 2.1a**).

With two hydroxyl groups in its structure, it offers wide opportunities for diverse modifications. mong these, introducing reactive functional groups such as epoxy and (meth)acrylates enables the formation of polymer networks with intriguing mechanical properties. For this reason, isosorbide is considered an appealing bio-based alternative to raw materials traditionally derived from petroleum sources, such as bisphenol A.

However, polymer networks derived from isosorbide exhibit significant hydrophilicity, leading to considerable swelling and, in some cases, material disintegration upon water exposure. [6-10] (**Figure 2.1b**).

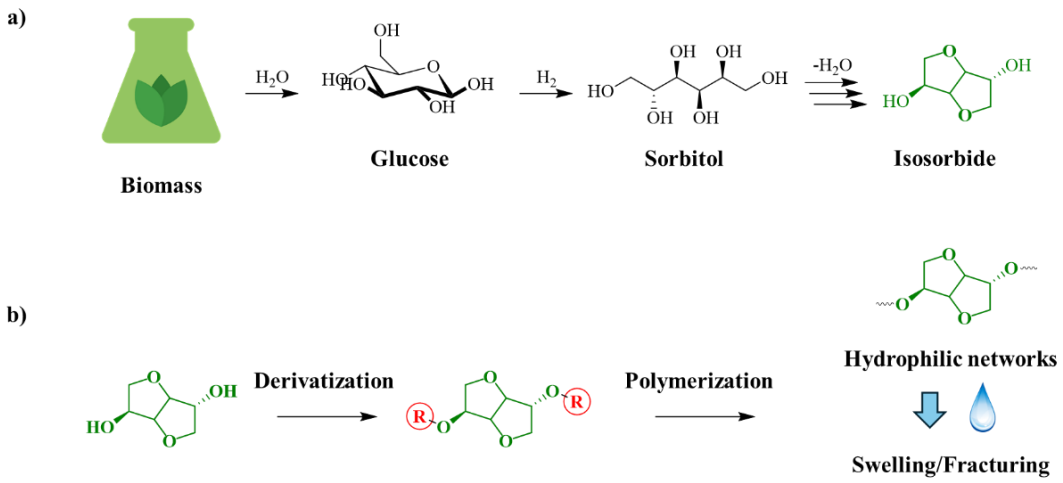

Figure 2.1. a) Synthesis from biomass, **b)** derivatization and polymerization of isosorbide.

While this phenomenon highlights significant limitations in the mechanical stability and practical applicability of these materials in wet environments, it can be turned into an advantage.

Mold-based manufacturing processes, such as composite fabrication and injection molding, exemplify scenarios where controlled degradation of the mold material is advantageous, as it facilitates efficient removal of the mold once the final product has been formed. A disposable mold made from a material with strong mechanical properties and capable of rapid disintegration upon water exposure is appealing for the production of artifacts with advanced shape complexity.

To effectively fabricate a complex-shaped mold with these characteristics, an appropriate manufacturing technique is crucial. Out of all manufacturing processes, 3D printing stands out for the ability to design desired shapes using CAD and rapidly translate data into a three-dimensional custom object, while simultaneously keeping production costs low. Furthermore, examples of using 3D printing to produce water-soluble or hydrolysable molds have already been reported, suggesting its feasibility.[11,12] The wide range of available 3D printing techniques enables a selective choice of the most suitable one. In fact, parameters such as the cost and availability of raw materials, detail resolution, and mechanical performance of the produced artifacts should always be considered.

This study focused on vat polymerization (VP) 3D printing, selected for its compatibility with the widely available photopolymerizable isosorbide-based compounds. Although limited, existing literature provides a few examples of isosorbide derivatives used in photopolymerization [13] and VP 3D printing.[14,15] The objective of this work is to develop an isosorbide-based photoresin specifically designed for 3D printing objects that readily disintegrate in water. Potential applications for this material include the production of disposable molds for fabricating complex-shaped carbon fiber composites and injection-molded products with intricate geometries. (**Figure 2.2**)

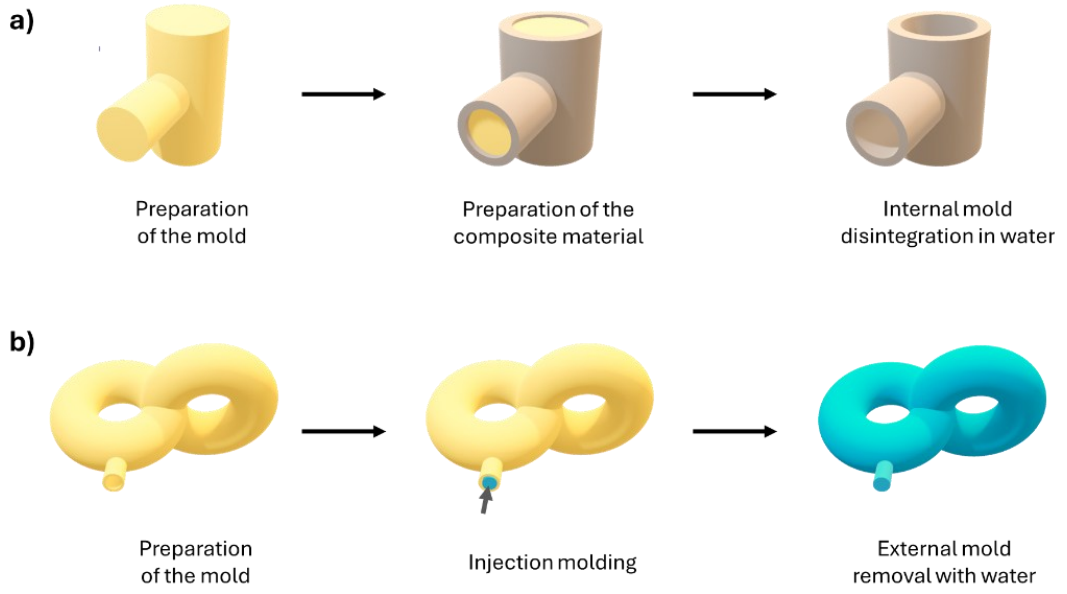

Figure 2.2. 3D printed **a)** internal molds for complex shape carbon fiber composite materials, and **b)** external molds for injection molding of complex shape object.

2.2 Results and discussion

To accomplish this objective, we focused on two primary isosorbide derivatives: isosorbide diglycidyl ether (**ISDGE**) and isosorbide diglycidyl methacrylate (**ISDGMA**) (structures shown in **Figure 2.3**).

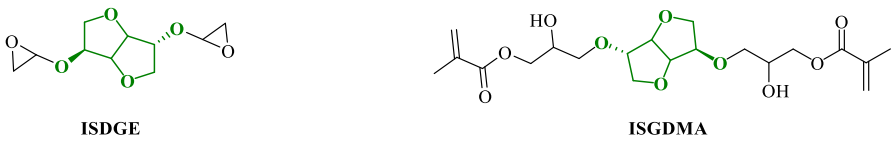

Figure 2.3. Molecular structures of **ISDGE** (left) and of **ISDGMA** (right).

Both derivatives exhibited properties advantageous for our application, though each exhibited noteworthy drawbacks.

ISDGE is a diepoxy synthesized through the reaction of isosorbide with epichlorohydrin. With a viscosity of 760 mPa·s at 25 °C, **ISDGE** satisfies the viscosity requirements for VP 3D printing. Additionally, the cured materials derived from this resin effectively disintegrate upon swelling in water.[6-8] However, the low absorbance of cationic photoinitiators at the high-wavelength radiation commonly used in stereolithography may pose challenges to the printing process.

Conversely, **ISDGMA**, obtained through the ring-opening addition of methacrylates to **ISDGE**, exhibited a viscosity of approximately 35400 mPa·s at 25 °C, rendering it unsuitable for 3D printing at room temperature. However, the radical polymerization kinetics of methacrylates align well with the rapid curing requirements of VP 3D printing, and a broader range of radical photoinitiators with extensive absorption spectra is available commercially. Nevertheless, immersion in water of materials derived from the homopolymerization of **ISDGMA** led to significant swelling without any actual disintegration or fragmentation of the objects.[9,10]

To achieve an optimal balance between reactivity and low viscosity, we prepared a series of photoresins by blending **ISDGE** and **ISDGMA** in various ratios. Materials obtained from the simultaneous or sequential polymerization of two or more components with orthogonal curing chemistries are referred to as interpenetrating polymer networks (**IPNs**).

The combination of polymers into **IPNs** enables the development of materials with properties intermediate between those of the original polymers. Key requirements for obtaining a stable **IPN** include good miscibility of the starting monomers and minimal phase separation during the curing process.[16,17] The literature contains various examples of epoxy/(meth)acrylate **IPNs** applied in VP 3D printing, which can be distinguished based on the curing method.

The first and most direct approach is the addition of a combination of radical and cationic photoinitiators, enabling the simultaneous photocuring of both matrices.[18]

A second approach uses radical photoinitiators to enable photocuring of the methacrylate component during 3D printing. An appropriate imidazole initiator is incorporated in the formulation to enable post-printing thermally accelerated curing of the epoxy component.[19]

In this work, both strategies are independently implemented, resulting in two arrays of **ISDGE/ISGDMA**-based photocurable formulations, each studied separately.

2.2A Isosorbide-based IPNs with simultaneously photocurable matrices

2.2A.1 Formulation of the resins and determination of the viscosity at room temperature

A set of photocurable formulations was prepared by mixing various proportions of **ISDGE** and **ISDMA**. Each mixture was supplemented with a constant amount of a cationic photoinitiator solution (**CPI**) and a radical photoinitiator mixture (**RPI**). The **CPI** consists of 50 wt% solution of a hexafluorophosphate sulfonium salt in propylene carbonate, while the **RPI** is a mixture of 50 wt% phenylbis(2,4,6-trimethylbenzoyl)phosphine oxide and 50 wt% 1-hydroxycyclohexyl phenyl ketone. Additionally, the effect of 2-hydroxyethyl methacrylate (**HEMA**) was evaluated, as it is expected to enhance hydrophilicity, reduce viscosity due to its own low viscosity, and form covalent bonds with both networks, thereby minimizing phase separation and improving mechanical performance. The molecular structures of the components used to formulate the photoresins are shown in **Figure 2.4**.

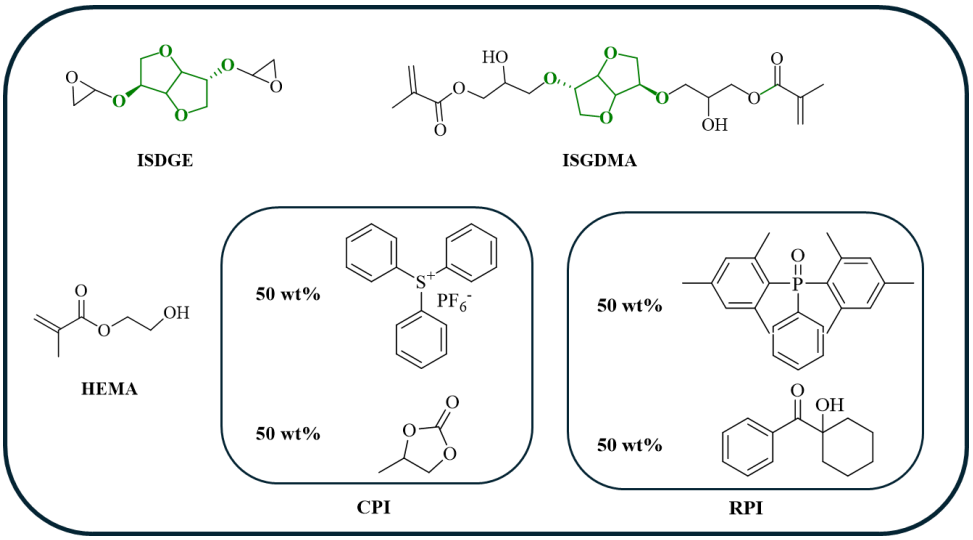

Figure 2.4. Chemical structures of the species contained in the simultaneously photocurable photoresins.

All formulations were prepared by mixing the specified materials in varying weight ratios and subjecting the mixtures to reduced pressure until complete dissolution of the solid components and homogenization was achieved. In addition to the formulations derived from mixing **ISDGE**, **ISGDMA**, and **HEMA**, **100**ISDGE and **100**ISDGDMA were prepared by incorporating fixed amounts of **CPI** and **RPI** into pure **ISDGE** and **ISGDMA**, respectively. Although **100**ISDGE and **100**ISDGDMA are not considered suitable for 3D printing due to the limitations previously discussed, they were included in the study to evaluate the properties of the material obtained from their photocuring process. To evaluate the potential of these formulations for 3D printing, a preliminary assessment of their viscosity at 25 °C was conducted. The quantities of materials used in the formulations and the corresponding viscosity data are provided in **Table 2.1** (more detailed informations provided in **Table A2.1**).

Resin	**ISDGE** (wt%)	**CPI** (wt%)	**ISGDMA** (wt%)	**RPI** (wt%)	**HEMA** (wt%)	**Viscosity at 25 °C** (mPa s)
100ISDGE	97.0	3.0	/	/	/	755
100ISDGDMA	/	/	98.0	2.0	/	55000
2ISDGE**1**ISGDMA	63.3	3.0	31.7	2.0	/	1910
2ISDGE**1**ISGDMA(HEMA)	60.0	3.0	30.0	2.0	5.0	1240
1ISDGE**2**ISGDMA	31.7	3.0	63.3	2.0	/	8450
1ISDGE**2**ISGDMA(HEMA)	30.0	3.0	60.0	2.0	5.0	3400

Table 2.1. Simultaneously photocurable photoresins formulation details and corresponding viscosities determined at 25 °C.

As expected, viscosity measurements at 25 °C indicate a decrease as **ISDGE** content increases, particularly with the addition of 5 wt% **HEMA**, which significantly lowers viscosity. In contrast, although blended with several low-viscosity components, **ISGDMA** markedly increases the viscosity of the final formulations. Therefore, **2**ISDGE**1**ISGDMA(HEMA) is the only photoresin formulated exhibiting promising features for **VP** 3D printing applications, as its viscosity approaches the maximum printability limit of approximately 1200 mPa s.

2.2A.2 Simultaneous photocuring of the formulations

To characterize the polymer networks formed by photocuring, samples of photocurable resin with thicknesses up to 4 mm were polymerized using a dual step photocuring protocol. This protocol involves an initial irradiation with a 405 nm LED lamp, followed by a subsequent exposure to a 365 nm LED lamp.

This two-step approach is designed to more accurately simulate **VP** 3D printing conditions, as these printers typically use visible light sources, commonly operating at 405 nm. However, 405 nm radiation is relatively ineffective at activating the **CPI**, making a subsequent curing step with higher-energy 365 nm radiation necessary to achieve high conversion in both the epoxy and methacrylate networks.

2.2A.3 Glass transition temperature evaluation

Common mold-based manufacturing processes usually rely on high-temperature treatments. Since a sudden increase in the thermal expansion coefficient is anticipated near the glass transition temperature (*Tg*), exceeding this threshold could significantly alter the mold dimensions, thus negatively impacting the quality of the process. Therefore, a clear quantification of the *Tg* using a technique based on the evaluation of the expansion coefficient is required. Thermomechanical analysis (**TMA**), capable of evaluating the linear deformation of a sample as a function of temperature, proved to be the most suitable method. **Table 2.2** shows the values of *Tg* determined via TMA on the cured materials.

Resin	*Tg* determined via TMA (°C)
100ISDGE	83 °C
100ISDGDMA	101 °C
2ISDGE**1**ISGDMA	72 °C
2ISDGE**1**ISGDMA(HEMA)	76 °C
1ISDGE**2**ISGDMA	84 °C
1ISDGE**2**ISGDMA(HEMA)	83 °C

Table 2.2. Glass transition temperatures of the cured materials of the simultaneously photocurable photoresin evaluated via TMA.

A few considerations can be made regarding the data reported above. All the cured formulations exhibited *Tg* ranging from about 70 °C to 100 °C. The incorporation of **ISDGE** and **ISGDMA** into **IPN** precursor photoresins results in lowering *Tg* values compared to those obtained from the homopolymerization of **ISGDMA**. The *Tg* values of **IPNs** increase with increasing **ISGDMA** content, and the homopolymer obtained from the photocuring of pure **ISGDMA** exhibits the highest *Tg* value. Finally, the presence of a 5 wt% of **HEMA** does not significantly affect the *Tg*.

2.2A.4 Flexural testing

Bending tests were performed to allow a deeper understanding of the mechanical properties of the photocured materials as a function of photoresin content. Standard ISO178 specimens were prepared by polymerizing the simultaneously photocurable formulations according to the two-step procedure described above. Young's modulus is a key parameter, as it provides insight into how the material deforms under applied stress. Young's modulus values obtained from bending tests are reported in **Figure 2.5**.

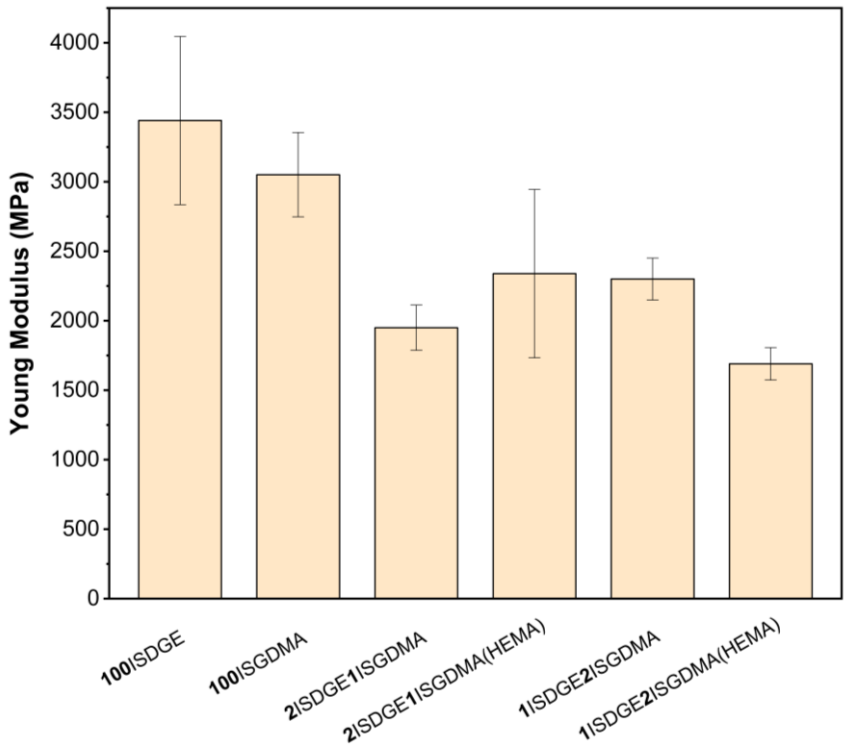

Figure 2.5. Young's modulus values obtained from the bending tests with ISO178 specimens obtained from simultaneous photocuring of designed photoresins.

IPN samples derived from the curing of **ISDGE** and **ISDGMA** blends exhibit significantly lower Young's modulus values compared to those measured for pure **ISDGE**- and **ISDGMA**-based networks. This behavior may be attributed to microphase separation occurring within the material during the simultaneous two-step photocuring process, which suggests partial incompatibility between the two materials. Additionally, the inclusion of **HEMA** does not result in any notable changes to the mechanical properties.

2.2A.5 Testing disintegration in water

Given that rapid disintegration in water is a key characteristic desired in these materials, several tests were performed to evaluate this property. Disk-shaped samples were cured using the two-step photocuring procedure previously described. Subsequently, the samples

were fully immersed in water. After 72 h at room temperature eventual disintegration of the disks was evaluated. Results and observations are presented in **Figure 2.6**.

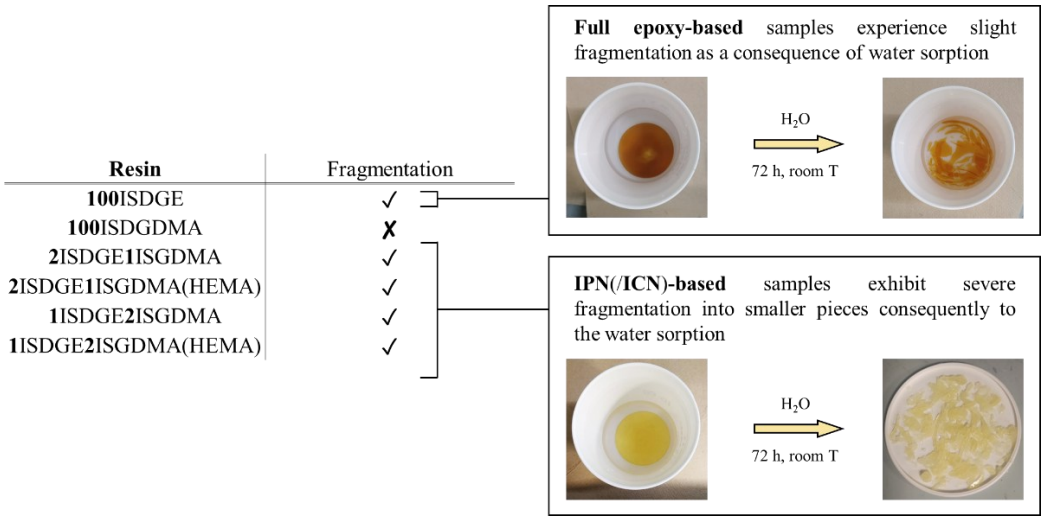

Figure 2.6. Observations on the materials after 72 h of immersion in water at room temperature.

Consistent with reports in the literature, fully **ISGDMA**-based networks were observed to swell and deform after prolonged immersion in water, without significant fracturing. One contributing factor could be the higher aliphatic chain content resulting from methacrylate polymerization, which reduces the material's hydrophilicity, making it less prone to water incorporation within the network.

In contrast, fully **ISDGE**-based materials exhibited more extensive fragmentation after 72 h. This increased fragmentation is likely due to the high content of hydrophilic polyether chains within these networks, formed via the photoinitiated homopolymerization of oxirane groups. Water immersion of **IPNs** resulted in deeper fracturing, with fragmentation into smaller pieces. The lower Young's modulus observed in bending tests may contribute to this behavior, as similar internal stresses generated by water absorption would be expected to cause greater deformation, making the material more susceptible to fracturing.

2.2A.6 VP 3D printing experiments

The 3D printing of mold prototypes for carbon fiber manufacturing focused on using **2**ISDGE**1**ISGDMA(HEMA), as it is the only photoresin with a viscosity compatible with printing, and the cured materials demonstrated substantial fracturing in water.

For the 3D printing experiments, **2**ISDGE**1**ISGDMA(HEMA) was preliminarily modified with the addition of 0.03 wt% methyl orange. The purpose of adding methyl orange is to absorb part of the light emitted by the instrument, reducing excessive radiation diffusion that could lead to the curing of parts not directly exposed to the light source.

The feasibility of 3D printing was evaluated by producing a model of an airplane aileron. The printing was attempted testing different layer thicknesses and varying single-layer irradiation times.

Despite various precautions adopted, 3D printing using **2**ISDGE**1**ISGDMA(HEMA) resulted challenging. The best result obtained from printing experiments is shown in **Figure 2.7**.

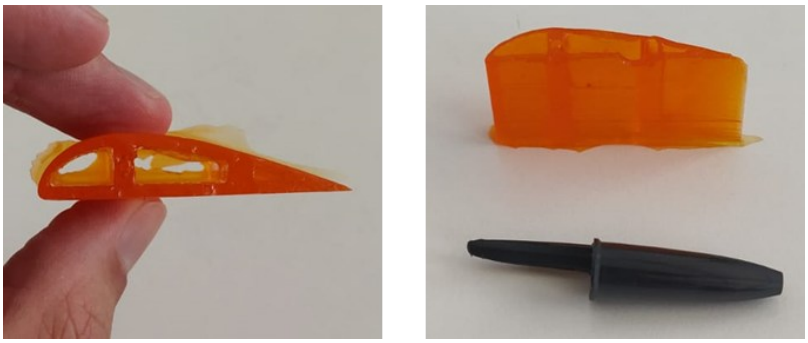

Figure 2.7. Images of samples 3D printed using the **2**ISDGE**1**ISGDMA(HEMA) photoresin modified with 0.03 wt% methyl orange.

As shown in the image above, the shape of the printed object closely matches the virtual design, with accurate proportions and a high level of detail. However, the final height of the object was only 3 cm, compared to the 10 cm specified in the CAD model. This is due to the sudden formation of a thin layer of cured resin between the object and the bottom of the vat.

This layer, partially attached to the base of the prototype shown in **Figure 2.7**, causes the object to detach from the printing platform, prematurely interrupting the printing process.
A possible explanation for the formation of the cured film is the cationic polymerization of **ISDGE**. Unlike radical polymerization, cationic polymerization is less susceptible to termination reactions, allowing polymerization to self-propagate in areas of the vat that are not directly exposed to light, thereby leading to the formation of a film.

2.2B Isosorbide-based IPNs with sequentially photo-thermal curable matrices

2.2B.1 Formulation of the resins and determination of viscosity at room temperature

A second set of formulations was prepared by mixing **ISDGE** and **ISGDMA** with a 50 wt% solution of N-methylimidazole in propylene carbonate (**IM**) and **RPI** in various amounts. Again, the effect of the addition of **HEMA** was evaluated. (**Figure 2.8**)

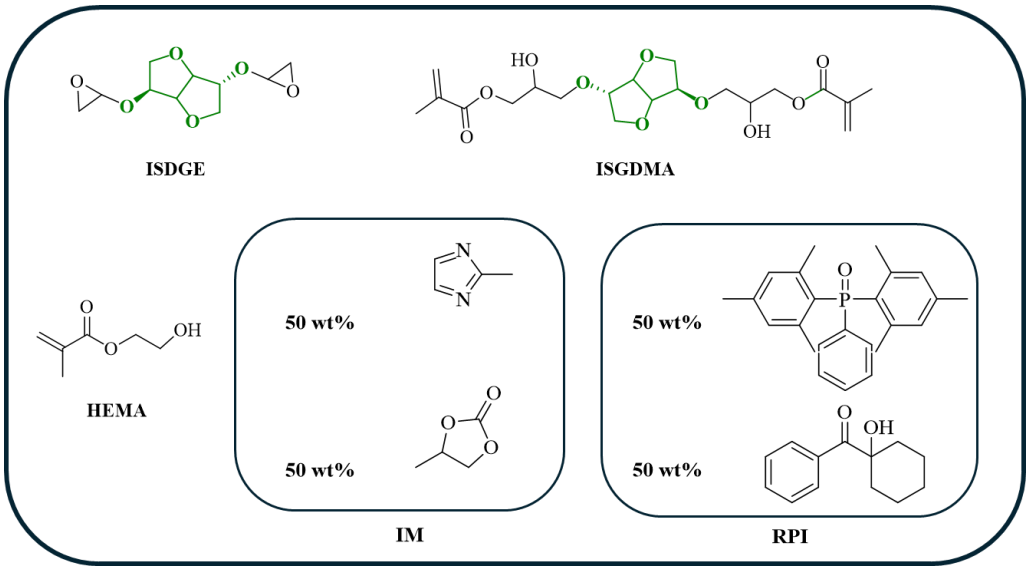

Figure 2.8. Chemical structures of the species contained in the sequentially photo-thermal curable photoresins.

In this case as well, all formulations were prepared by mixing the components under reduced pressure until complete homogenization, as described above.

Each photoresin was specifically designed to emulate the previously discussed simultaneously photocurable formulations, with **CPI** replaced by an equal weight ratio of **IM**.

An initial evaluation of the resins' viscosity at 25 °C was conducted, with **Table 2.3** showing the quantities used in each formulation alongside the resulting viscosity values (more detailed information is provided in **Table A2.2**).

Resin	**ISDGE** (wt%)	**IM** (wt%)	**ISGDMA** (wt%)	**RPI** (wt%)	**HEMA** (wt%)	**Viscosity at 25 °C** (mPa s)
100ISDGE	97.0	3.0	/	/	/	625
100ISDGDMA	/	/	98.0	2.0	/	55000
2ISDGE**1**ISGDMA	63.3	3.0	31.7	2.0	/	1650
2ISDGE**1**ISGDMA(HEMA)	60.0	3.0	30.0	2.0	5.0	910
1ISDGE**2**ISGDMA	31.7	3.0	63.3	2.0	/	5025
1ISDGE**2**ISGDMA(HEMA)	30.0	3.0	60.0	2.0	5.0	2700

Table 2.3. Sequentially photo-thermal curable photoresins formulation details and viscosities determined at 25 °C.

Also in this case, the **2**ISDGE**1**ISGDMA(HEMA) formulation is the most promising photoresin among those studied, exhibiting a viscosity suitable for VP 3D printing applications.

2.2B.2 Sequential photo-thermal curing of the formulations

Cured samples with a thickness of up to 4 mm were obtained using a two-step procedure, in which the methacrylate and epoxy matrices are cured sequentially.

In the first step the photoresin is exposed to a 405 nm LED lamp obtaining a prepolymerized material sample. This step aims to simulate the 3D printing phase, during which no significant conversion of the epoxy matrix is expected.

The second stage involves curing the material at 80 °C for 2 h, followed by a treatment at 120 °C for 4 h. This thermal process accelerates the kinetics of the imidazole-initiated anionic homopolymerization of the **ISDGE**'s oxiranes, allowing to achieve high conversion in the epoxy component.

2.2B.3 Glass transition temperature evaluation

The glass transition temperatures of materials polymerized using the sequential curing procedure were determined by TMA, and the resulting values are reported in **Table 2.4**.

Resin	*Tg* determined via TMA (°C)
100ISDGE	89 °C
100ISDGDMA	101 °C
2ISDGE**1**ISGDMA	73 °C
2ISDGE**1**ISGDMA(HEMA)	79 °C
1ISDGE**2**ISGDMA	86 °C
1ISDGE**2**ISGDMA(HEMA)	86 °C

Table 2.4. Glass transition temperatures of the cured materials obtained from sequentially photo-thermal curable photoresins evaluated via TMA.

Also in this case, the glass transition temperatures observed range from approximately 70 °C to 100 °C. The *Tg* values determined for each formulation are comparable to those obtained from the simultaneous photocuring process described in the previous section. Both

pure **ISDGE** and **ISGDMA**-based materials exhibit higher *Tg* values than the corresponding **IPNs**. For the **IPNs**, however, the *Tg* increases as the **ISGDMA** content rises. Once again, no significant difference in *Tg* was observed with the addition of **HEMA**.

2.2B.4 Flexural testing

Similarly to what was done with the previously studied systems, standard ISO178 specimens were obtained through the sequential curing of the formulations, following the procedure described above. Young's modulus values obtained from the bending experiments of these specimens are depicted in **Figure 2.9**.

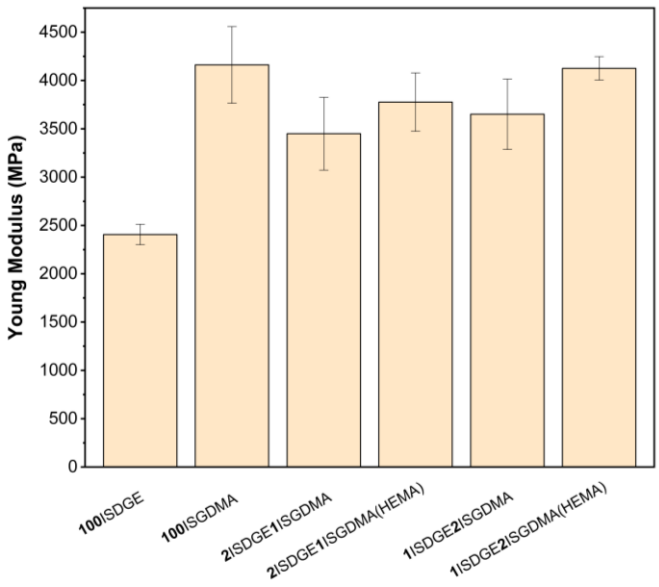

Figure 2.9. Young's modulus values obtained from the bending tests with ISO178 specimens obtained from sequential photo-thermal curing of designed photoresins.

Differently from what was observed for the previous systems, **IPNs** show remarkably higher Young's moduli, with values falling between the pure **ISDGE**- and **ISGDMA**-based systems. This behavior may be associated with a higher homogeneity of the samples, achieved thanks to the slower thermal curing of the epoxy component. Finally, the addition of **HEMA** seems to slightly improve the modulus values.

2.2B.4 Testing disintegration in water

Disk-shaped samples with 6.5 cm diameter and 2.5 mm thickness were prepared according to the sequential photo-thermal curing protocol described above. Eventual disintegration of the material was evaluated after 72 h of immersion in water at room temperature. Unexpectedly, neither the pure networks nor the **IPNs** (except for the material obtained from **100**ISDGE photoresin) exhibited significant fragmentation after the specified duration. Instead, all samples showed only swelling and minor cracking. This result is thought to be related to the higher Young's modulus values observed in **IPNs** obtained through sequential photo-thermal curing, as compared to those from simultaneous photocuring. Higher Young's modulus values for similar formulations suggest that, given comparable water uptake due to the networks' similar hydrophilicity, the material experiences similar internal stresses. These stresses lead to reduced deformation, making fracturing more challenging.

Considering the slower fracturing kinetics, we evaluated the effect of a temperature increase, focusing specifically on the formulation **2**ISDGE**1**ISGDMA(HEMA). Similar disk-shaped samples were prepared using the same procedure. The samples were immersed in water and then heated to 40 °C, 60 °C, and 80 °C. Times required for effective fragmentation are reported in **Figure 2.10**.

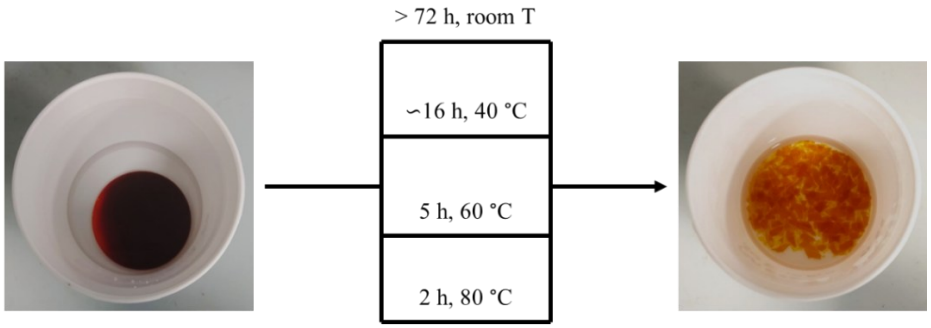

Figure 2.10. Disintegration times of the materials immersed in water at different temperatures.

The results show that, although significant fracturing of the materials was not observed at room temperature within practical timeframes, the process can be readily accelerated by increasing the temperature. As expected, the fracture rate increases with temperature.

2.2B.5 VP 3D printing experiments

Also in this case, the **2**ISDGE**1**ISGDMA(HEMA) photoresin, formulated for the sequential photo-thermal curing strategy, was selected for 3D printing. The photoresin was initially modified by adding 0.03 wt% methyl orange. The same airplane aileron model used in previous experiments was chosen for the 3D printing trials.
Despite various attempts to 3D print the model using various layer thicknesses and various single layer irradiation times all the objects obtained exhibited considerable fractures and missing parts as shown in **Figure 2.11**.

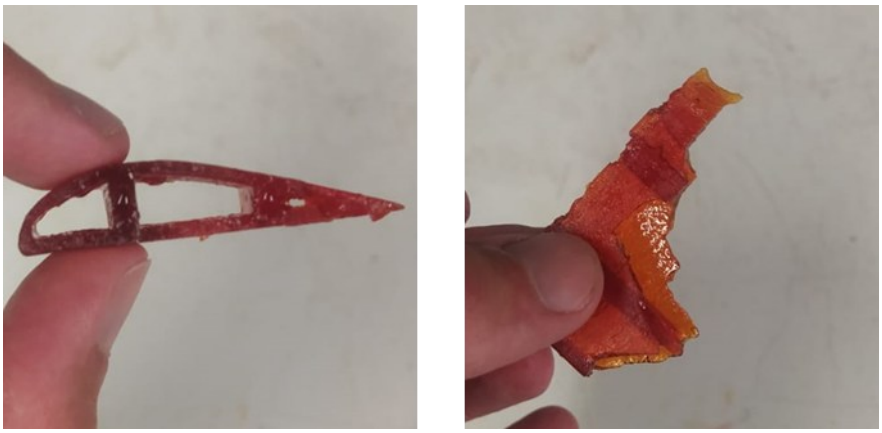

Figure 2.11. Images of samples 3D printed using the **2**ISDGE**1**ISGDMA(HEMA) photoresin modified with 0.03 wt% methyl orange.

A possible explanation for the poor results achieved could be the relatively low concentration of **ISGDMA** in **2**ISDGE**1**ISGDMA(HEMA). Indeed, **ISGDMA** is the only component that is readily photopolymerizable during 3D printing and is readily available to form the network.

2.3 Conclusions

In conclusion, two isosorbide derivatives were evaluated as precursors for photoresin formulations intended for **VP** 3D printing of disposable molds for injection molding and carbon fiber manufacturing.

Two sets of photoresins were prepared: one designed for a two-step photocuring process (405 nm followed by 365 nm irradiation), and the other for a two-step photo-thermal curing process (405 nm irradiation followed by thermal curing at 120 °C). Viscosity evaluations at 25°C allowed for the identification of the most suitable formulation, while *Tg* assessments helped determine the maximum operating temperature for 3D-printed molds. Flexural strength tests highlighted notable differences in the mechanical properties of the **IPNs** obtained through each curing strategy. Water fracturing tests further indicated that **IPNs** obtained via simultaneous curing exhibited faster disintegration, confirming their lower mechanical strength. This behavior could be ascribed to variations in the extent of interpenetration between the two polymer matrices, with simultaneous curing leading to a lower degree of interpenetration, as inferred from the observed mechanical properties.

Regrettably, none of the 3D printing attempts successfully produced intact molds, underscoring the challenges associated with employing photopolymerizable **IPNs** in 3D printing, particularly due to the difficulty in controlling the cationic photopolymerization of epoxy resins.

ACKNOWLEDGMENTS

Thanks to Dr. Ettore Fazio from Elantas EUROPE Collecchio (Parma). Thanks to Dr. Corrado Sciancalepore and Prof. Daniel Milanese from University of Parma for the help with 3D printing.

2.4 Experimental section

MATERIALS AND METHODS

All chemicals were obtained from certified commercial suppliers and used as received, without further purification.

Viscosity measurements of the raw materials and photoresin formulations were conducted using a Brookfield DV2T EXTRA HA rotational viscometer, with spindles SC4-21, SC4-27, or SC4-29 selected as appropriate.

Photoresins were irradiated using UV LED lamps from the PHOTOELECTRONIX DROLED L70 series, which emit monochromatic light at either 405 nm or 365 nm.

Thermomechanical analysis (TMA) was performed using a Discovery TMA 450 (TA Instruments).

Flexural tests were carried out using an INSTRON 5982 universal testing machine equipped with a 10 kN load cell. Samples were prepared and tested in compliance with the ISO 178 standard.

3D printing experiments were performed using a Kentstrapper Aura stereolithography printer, which features a 4K UV LCD screen emitting monochromatic light at a wavelength of 405 nm.

PHOTORESINS PREPARATION

Precise quantities and corresponding weight ratios of each component utilized in the preparation of 120 g of resin for simultaneous photocuring and sequential photo-thermal curing, respectively are detailed in **Table A2.1** and **Table A2.2**.

Photoresins formulations were prepared by combining all components in a light-shielded vessel and stirring the resulting mixture under reduced pressure until complete dissolution of the photoinitiators was achieved, resulting in a homogeneous solution.

TWO-STEP SIMULTANEOUS PHOTOCURING PROTOCOL

The photoresins selected for two-step simultaneous photocuring were as follows. A measured amount of fresh photoresin was poured into a mold, with its upper surface exposed

to light for curing. The resin was initially irradiated for 5 min using a 405 nm LED lamp at a power density of 1500 mW/cm². The partially polymerized material was then subjected to a second irradiation step for an additional 5 min using a 365 nm LED lamp at a power density of 400 mW/cm².

SEQUENTIAL PHOTO-THERMAL CURING PROTOCOL

The photoresins chosen for sequential photo-thermal curing were processed in the following manner. A measured quantity of fresh resin was poured into a mold, ensuring that the top surface was exposed to light for curing. Initially, the resin was irradiated for 1 min with a 405 nm LED lamp at a power density of 1500 mW/cm². The partially polymerized material was then heated gradually to 120 °C over the course of 1 h, maintained at this temperature for an additional 4 h, and then cooled to room temperature within 1 h.

THERMO-MECHANICAL ANALYSIS (TMA)

Disk-shaped samples, each with a diameter of 6.5 cm and a thickness of 2.5 mm, were prepared by curing 10 g of each formulated photoresin using the most suitable curing procedure from the two described above. Square samples with a surface area of 1 cm² were then cut from the resulting materials. Each sample underwent two sequential heating cycles from -20 °C to 180 °C at a rate of 5 °C/min, with an intermediate cooling step at -50 °C/min. The glass transition temperature (*Tg*) values were determined on the second heating ramp by calculating the intersection of regression lines fitted to data points before and after the inflection point.

WATER DISINTEGRATION TESTING

Disk-shaped samples, each 6.5 cm in diameter and 2.5 mm in thickness, were prepared by curing 10 g of each formulated photoresin using the most appropriate curing method from those described above. Each sample was fully immersed in 100 mL of water and stored at room temperature, with disintegration evaluated after 72 h.

The fragmentation kinetics of samples sequentially photo-thermally cured from the **2**ISDGE**1**ISGDMA(HEMA) photoresin were further evaluated at different temperatures. Similar disk-shaped samples were immersed in 100 mL of water and subsequently heated

isothermally at 40 °C, 60 °C, and 80 °C. Fragmentation kinetics were monitored and assessed at hourly intervals.

VP 3D PRINTING AND POST-CURING OF THE SPECIMENS

120 g of each photoresin selected for 3D printing were prepared according to the weight percentages and absolute quantities described above and homogenized as previously indicated. An additional 0.03 wt% of methyl orange was dissolved in each photoresin.

The feasibility of 3D printing was assessed by fabricating a model of an airplane aileron with dimensions of 10 x 5 x 1 cm. The 3D model and its orientation relative to the printer base are illustrated in **Figure 2.12**. For each photoresin, a series of trials was performed, varying the layer thickness between 0.07 cm and 0.12 cm and adjusting the irradiation time per layer between 14 s and 20 s.

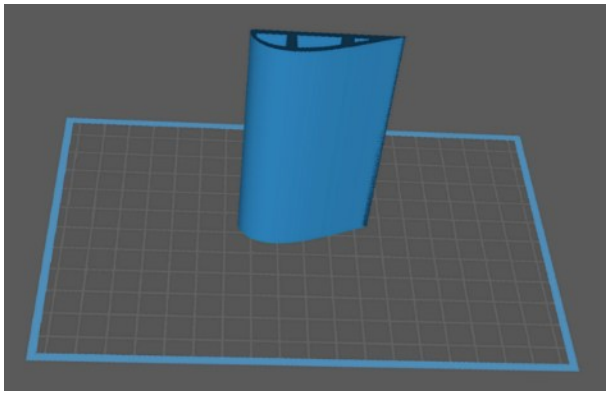

Figure 2.12. 3D printed airplane aileron model.

2.5 Appendix information

Resin	ISDGE	CPI	ISGDMA	RPI	HEMA
100ISDGE	97.0 wt% 116.4 g	3.0 wt% 3.6 g	/	/	/
100ISDGDMA	/	/	98.0 wt% 117.6 g	2.0 wt% 2.4 g	/
2ISDGE**1**ISGDMA	63.3 wt% 76.0 g	3.0 wt% 3.6 g	31.7 wt%	2.0 wt% 2.4 g	/
2ISDGE**1**ISGDMA(HEMA)	60.0 wt% 72.0 g	3.0 wt% 3.6 g	30.0 wt% 36 g	2.0 wt% 2.4 g	5.0 wt% 6.0 g
1ISDGE**2**ISGDMA	31.7 wt%	3.0 wt% 3.6 g	63.3 wt% 76.0 g	2.0 wt% 2.4 g	/
1ISDGE**2**ISGDMA(HEMA)	30.0 wt% 36 g	3.0 wt% 3.6 g	60.0 wt% 72.0 g	2.0 wt% 2.4 g	5.0 wt% 6.0 g

Table A2.1. Weight ratios and absolute masses of each component used in the formulation of 120 g of simultaneously photocurable photoresins.

Resin	ISDGE	IM	ISGDMA	RPI	HEMA
100ISDGE	97.0 wt% 116.4 g	3.0 wt% 3.6 g	/	/	/
100ISDGDMA	/	/	98.0 wt% 117.6 g	2.0 wt% 2.4 g	/
2ISDGE**1**ISGDMA	63.3 wt% 76.0 g	3.0 wt% 3.6 g	31.7 wt%	2.0 wt% 2.4 g	/
2ISDGE**1**ISGDMA(HEMA)	60.0 wt% 72.0 g	3.0 wt% 3.6 g	30.0 wt% 36 g	2.0 wt% 2.4 g	5.0 wt% 6.0 g
1ISDGE**2**ISGDMA	31.7 wt%	3.0 wt% 3.6 g	63.3 wt% 76.0 g	2.0 wt% 2.4 g	/
1ISDGE**2**ISGDMA(HEMA)	30.0 wt% 36 g	3.0 wt% 3.6 g	60.0 wt% 72.0 g	2.0 wt% 2.4 g	5.0 wt% 6.0 g

Table A2.2. Weight ratios and absolute masses of each component used in the formulation of 120 g of sequentially photo-thermal curable photoresins.

2.6 References

(1) M. Rose, R. Palkovits, Isosorbide as a Renewable Platform chemical for Versatile Applications-Quo Vadis?, *ChemSusChem* **2012**, *5*, 167–176, https://doi.org/10.1002/cssc.201100580.

(2) C. Dussenne, T. Delaunay, V. Wiatz, H. Wyart, I. Suisse, M. Sauthier, Synthesis of isosorbide: an overview of challenging reactions, *Green Chem.* **2017**, *19*, 5332-5344, https://doi.org/10.1039/C7GC01912B.

(3) A. Romero, A. Nieto-Márquez, E. Alonso, Bimetallic Ru:Ni/MCM-48 catalysts for the effective hydrogenation of d-glucose into sorbitol, *Appl. Catal. A: Gen.* **2017**, *529*, 49-59, https://doi.org/10.1016/j.apcata.2016.10.018.

(4) K. Gao, J. Xin, D. Yan, H. Dong, Q. Zhou, X. Lu, S. Zhang, Direct conversion of cellulose to sorbitol via an enhanced pretreatment with ionic liquids, *J. Chem. Technol. Biotechnol.* **2018**, *93*, 2617-2624, https://doi.org/10.1002/jctb.5615.

(5) J. Zhang, J. Li, S. B. Wu, Y. Liu, Advances in the catalytic production and utilization of sorbitol, *Ind. Eng. Chem. Res.* **2013**, *52*, 11799–11815, https://doi.org/10.1021/ie4011854.

(6) J. Łukaszczyk, B. Janicki, M. Kaczmarek, Synthesis and properties of isosorbide based epoxy resin, *Eur. Polym. J.* **2011**, *47*, 1601-1606, https://doi.org/10.1016/j.eurpolymj.2011.05.009.

(7) M. Chrysanthos, J. Galy, J.-P. Pascault, Preparation and properties of bio-based epoxy networks derived from isosorbide diglycidyl ether, *Polymer* **2011,** *52*, 3611-3620, https://doi.org/10.1016/j.polymer.2011.06.001.

(8) J. Hong, D. Radojčić, M. Ionescu, Z. S. Petrović, E. Eastwood, Advanced materials from corn: isosorbide-based epoxy resins, *Polym. Chem.* **2014**, *5*, 5360-5368, https://doi.org/10.1039/C4PY00514G.

(9) J Łukaszczyk, B Janicki, A Frick, Investigation on synthesis and properties of isosorbide based bis-GMA analogue, *J. Mater. Sci.: Mater. Med.* **2012**, *23*, 1149-1155, https://doi.org/10.1007/s10856-012-4594-6.

(10) J. Łukaszczyk, B. Janicki, A. López, K. Skołucka, H. Wojdyła, C. Persson, S. Piaskowski, M. Śmiga-Matuszowicz, Novel injectable biomaterials for bone augmentation based on isosorbide dimethacrylic monomers, *Mater. Sci. Eng.* **2014**, *40*, 76-84, https://doi.org/10.1016/j.msec.2014.03.046.

(11) R. Wick-Joliat, M. Tschamper, R. Kontic, D. Penner, Water-soluble sacrificial 3D printed molds for fast prototyping in ceramic injection molding, *Addit. Manuf.* **2021**, *48*, 78-86, https://doi.org/102408, 10.1016/j.addma.2021.102408.

(12) https://www.addyx.it/.

(13) D. N. Lastovickova, F. R. Toulan, J. R. Mitchell, D. VanOosten, A. M. Clay, J. F. Stanzione III, G. R. Palmese, J. J. La Scala, Resin, cure, and polymer properties

of photopolymerizable resins containing bio-derived isosorbide, *J. Appl. Polym.* **2021**, *138*, 1-22, https://doi.org/10.1002/app.50574.

(14) A. Liguori, E. Oliva, M. Sangermano, M. Hakkarainen, Digital Light Processing 3D Printing of Isosorbide- and Vanillin-Based Ester and Ester–Imine Thermosets: Structure–Property Recyclability Relationships, *ACS Sustain. Chem. Eng.* **2023**, *11*, 14601–14613, https://doi.org/10.1021/acssuschemeng.3c04362.

(15) X. Chu, J. Tu, H. R. Berensmann, J. J. La Scala, G. R. Palmese, High Tg, Bio-Based Isosorbide Methacrylate Resin Systems for Vat Photopolymerization, *Polymers* **2023**, *15*, 1-14. https://doi.org/10.3390/polym15092007.

(16) J. Joy, K. Winkler, K. Joseph, S. Anas, S. Thomas, Epoxy/methyl methacrylate acrylonitrile butadiene styrene (MABS) copolymer blends: reaction-induced viscoelastic phase separation, morphology development and mechanical properties, *New J. Chem.* **2019**, *43*, 9216-9225, https://doi.org/10.1039/C8NJ05653F.

(17) U. Farooq, J. Teuwen, C. Dransfeld, Toughening of Epoxy Systems with Interpenetrating Polymer Network (IPN): A Review, *Polymers* **2020**, *12*, 1908, https://doi.org/10.3390/polym12091908.

(18) S. Lantean, I. Roppolo, M. Sangermano, C. F. Pirri, A. Chiappone, Development of New Hybrid Acrylic/Epoxy DLP-3D Printable Materials, *Inventions* **2018**, *3*, 29, https://doi.org/10.3390/inventions3020029.

(19) H. Wang, Z. Huang, Y. Zhang, L. Li, J. Li, Design of enhanced mechanical properties by interpenetrating network of 3D printing dual-curing resins, *Polymer* **2023**, *282*, 126153, https://doi.org/10.1016/j.polymer.2023.126153.

Chapter 3

"Epoxy-Based Photoresins for Enhanced Curing Depth via Photo-Induced Frontal Polymerization"

This study was conducted as part of the internship at Elantas EUROPE, Collecchio (Parma).

3.1 Introduction

Photopolymerization is a process in which polymeric materials are cured upon exposure to ultraviolet (UV) or visible light[1,2]. This technique allows for highly localized curing, enabling precise polymerization in regions directly exposed to light. As a result, photopolymerization is particularly well-suited for the fabrication of complex microstructures with fine resolution and smooth surfaces.[3,4] It is widely applied in fields such as coatings, printing inks, dental composite resins, photoresists, and 3D printing[4-7].

However, photopolymerization is limited by the shallow penetration depth of light, which decreases with intensity according to the Beer-Lambert law. This limits the effective curing primarily to thin layers, typically up to 50 μm, or at most a few millimeters, depending on factors like material absorptivity, the type of photoinitiator, and the wavelength and intensity of the light source. To overcome this limitation, innovative approaches are needed.[8]

Frontal polymerization offers a promising solution by enabling efficient polymerization even under challenging conditions. This method facilitates curing in shadowed or inaccessible regions and supports the polymerization of larger material volumes.[9,10] Frontal polymerization works by generating a polymerization front, which is initiated by an external stimulus such as heat[11] or irradiation[12]. Once triggered, the polymerization front propagates through the material in a self-sustaining manner, driven by the exothermic nature of the reaction and without requiring further external activation. The formation of the polymerization front is achieved by supplementing the system with complementary initiators, which are activated by the heat released during the exothermic reaction. This self-propagating mechanism provides significant advantages, including faster processing, higher energy efficiency, and reduced reliance on external equipment, making it ideal for a range of applications such as coatings[13], adhesives[14,15], 3D printing[16,17], and composites[10,18].

In particular, research on the frontal polymerization of epoxy resins is highly relevant *to* the manufacturing of fiber-reinforced composite materials, as epoxies are extensively used as polymer matrices in these systems. The application of frontal polymerization in these systems holds the potential to enable faster production rates and significantly lower the energy consumption associated with the manufacturing processes.

In recent years, studies have focused on the radical-induced cationic homopolymerization of oxirane functionalities in epoxy resins.[15,19-21] The aim of this project is to develop a fully epoxy-based formulation capable of undergoing both thermally- and photoinitiated frontal polymerization, leveraging an entirely cationic mechanism. The critical components for designing an efficient formulation suitable for photoinitiated frontal polymerization include a cationic photoinitiator and a thermally triggerable cationic initiator.

As the photoinitiator, a hexafluorophosphate sulfonium salt dissolved in a 50 wt% solution of propylene carbonate (**CPI**) was selected. This initiator is well-established for initiating photopolymerization reactions. Upon exposure to UV light, **CPI** undergoes a series of reactions, leading to the formation of the highly reactive superacid HPF6, which in turn initiates the cationic homopolymerization of oxiranes. (**Scheme 3.1a**) Similarly, the thermally initiated cationic initiator used in this study is a 50 wt% solution of N-(4-methoxybenzyl)-N,N-dimethylbenzenaminium hexafluoroantimonate in propylene carbonate (**TI**). This initiator was selected for its ability to efficiently trigger polymerization upon heating. The elevated temperature facilitates the decomposition of **TI** into N,N-dimethylaniline and a p-methylbenzyl cation, the key species responsible for initiating the thermal cationic polymerization of oxiranes (**Scheme 4.1b**).[22,23]

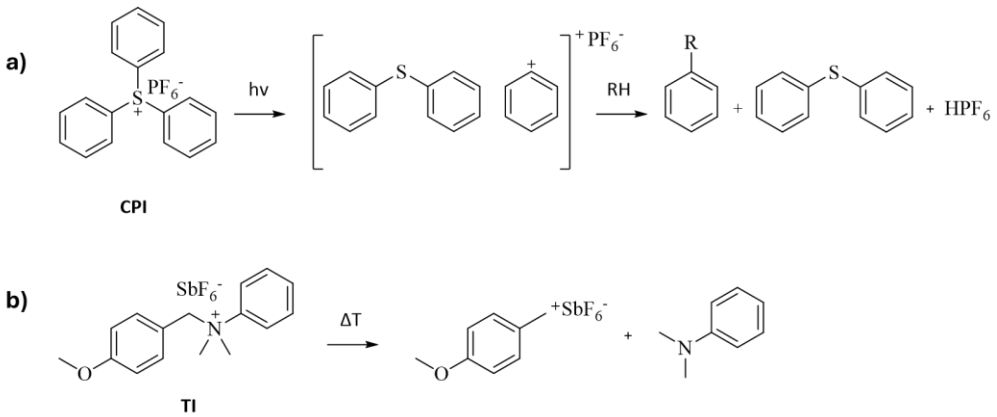

Scheme 3.1. a) Photoactivation mechanism of **CPI**, and **b)** thermally assisted activation of **TI**.

3.2 Results and discussion

3.2.1 Choice of raw materials

To develop a fully epoxy-based formulation capable of efficient frontal polymerization and suitable for industrial scalability, two bifunctional epoxy resins were selected as the starting materials. The chosen resins include bisphenol F diglycidyl ether (**BFDGE**), and 3,4-epoxycyclohexylmethyl-3',4'-epoxycyclohexane carboxylate (**ECC**). The molecular structures of the epoxy resins used as raw materials are presented in **Figure 3.1**.

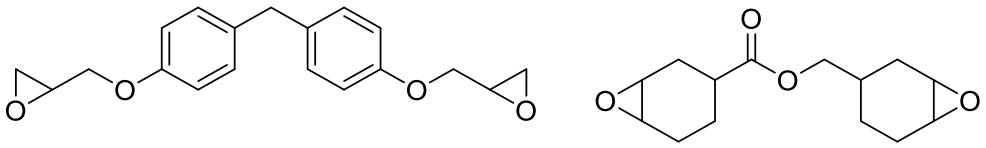

BFDGE **ECC**

Figure 3.1. Molecular structures of epoxy resins used as raw materials.

BFDGE is a widely used diepoxy resin derived from bisphenol F. Its curing typically relies on the use of amines and carboxylic acids. In contrast, **ECC** is a cycloaliphatic diepoxy resin known for its exceptionally high reactivity in cationic homopolymerization, a process where neutral monomers repeatedly attack an oxonium ion in a nucleophilic fashion. This remarkable reactivity results from a synergistic combination of molecular factors, primarily ring strain and steric hindrance.[24]

However, despite **ECC**'s superior reactivity, it is considerably more expensive than the more commonly used bisphenol-based resins, such as **BFDGE**. Given that **BFDGE** is more affordable, our aim was to develop a functional blend that is rich in **BFDGE** to keep the material cost-effective, while leveraging **ECC** in smaller quantities to boost the reactivity of the blend. To explore this approach, we tested various blends of **ECC** with **BFDGE**, optimizing the ratio to balance both performance and cost-effectiveness.

3.2.2 Assessing the initiators activity via DSC

Since the combination of sulfonium and benzylanilinium salts for photoinduced frontal polymerization is unprecedented in the literature, preliminary tests were conducted to evaluate their compatibility. A high curing enthalpy is critical for ensuring the effective activation of **TI** without dependence on an external heat source. This ensures efficient curing in areas shielded from light, where **CPI** remains inactive.

To investigate the thermal curing behavior, a series of formulations was prepared by dissolving **CPI** and **TI** at varying weight percentages into pure **BFDGE** (**100**BFDGE formulations) and, in parallel, into pure **ECC** (**100**ECC formulations). DSC was employed to analyze the thermally induced curing of these formulations.

The results indicate that both **100**BFDGE and **100**ECC formulations with 0.0 wt% **CPI** and fixed 2.0 wt% **TI** share similar curing enthalpies. The main difference between formulations derived from pure **BFDGE** and **ECC** lies in their peak temperatures, which differ by approximately 15–20 °C. **ECC**-based resins exhibit lower peak temperatures, indicating faster reaction kinetics despite having similar curing enthalpies (see **100**BFDGE**0**CPI**2**TI and **100**ECC**0**CPI**2**TI in **Table A2.2**, **Appendix information**). Furthermore, the curing enthalpies, onset, and peak temperatures remain largely unchanged when the **TI** content is increased up to 8.0 wt%, while maintaining the **CPI** content at 0.0 wt% (see **100**BFDGE**0**CPI**8**TI and **100**ECC**0**CPI**8**TI in **Table A2.2**, **Appendix information**).

For both **100**BFDGE and **100**ECC formulations, a progressive increase in **CPI** content, while maintaining a fixed 2.0 wt% of **TI**, results in a significant decrease in the absolute curing enthalpy (**Figure 3.2a**). In contrast, the onset and peak temperatures remain comparable to those observed in formulations without **CPI** (see **100**BFDGE**1-2-4**CPI**2**TI and **100**ECC**1-2-4**CPI**2**TI in **Table A2.2**, **Appendix information**). In **100**BFDGE resins, this reduction becomes significant after the addition of only 1.0 wt% **CPI**, while in **100**ECC resins, a notable decline in curing enthalpy is observed starting at 2.0 wt% **CPI**. This behavior is likely due to the hexafluorophosphate anion in **CPI** forming a tightly bound ion pair with the benzyl cation generated during **TI** activation. Such ion pairing limits the availability of the benzyl cation to effectively initiate cationic homopolymerization.

This quenching effect is further corroborated by data from formulations with higher **CPI** concentrations. Specifically, when **CPI** is fixed at 4.0 wt% (**Figure 3.2b**), a **TI** concentration

exceeding 8.0 wt% is required to achieve enthalpy values comparable to those observed in formulations without **CPI**. Even in this case, no significant variations in onset and peak temperatures are observed (see **100**BFDGE**4**CPI**0-2-8**TI and **100**ECC**4**CPI**0-2-8**TI in **Table A2.2**, **Appendix information**). Furthermore, as expected, photoresins lacking **TI** do not exhibit any thermally induced curing behavior.

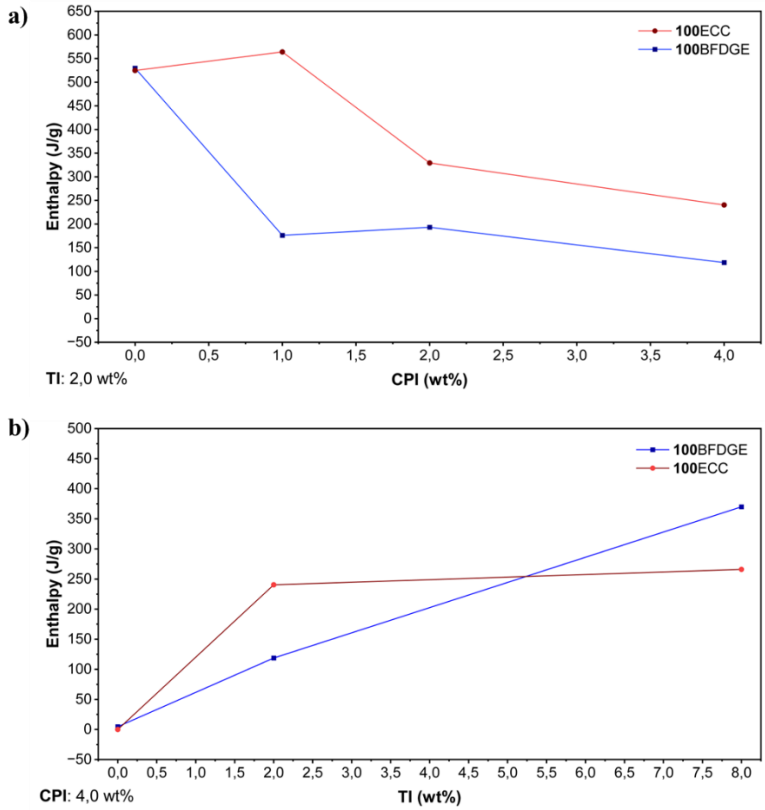

Figure 3.2. Curing enthalpies of photoresins formulated with a fixed 2.0 wt% of **TI** while varying the weight percentage of **CPI a)**, and **b)** with a fixed 4.0 wt% of **CPI** while varying the weight percentage of **TI**.

3.2.3 Evaluating thermally induced frontal polymerization in pure epoxy matrices

Having observed that **CPI** partially inhibits the system's thermally assisted reactivity, the study shifted its focus to formulations without **CPI**, which are anticipated to demonstrate the

highest exothermicity. Experiments were performed on pure **100**BFDGE and **100**ECC formulations with varying concentrations of **TI**. In these experiments, frontal polymerization was triggered by applying a thermal stimulus to the bottom of the tube containing the resin formulations. The progression of the curing front and the subsequent complete polymerization of the sample were carefully monitored and assessed. (**Figure 3.3**)

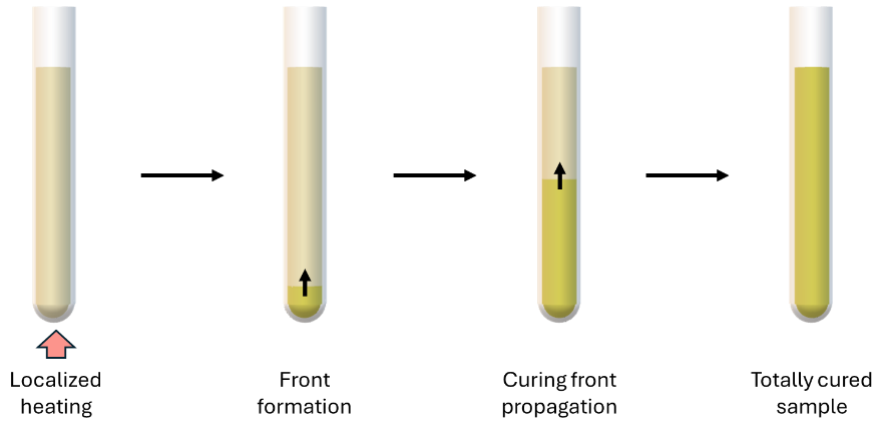

Figure 3.3. Thermally induced frontal polymerization experiment setup.

Table 3.1 indicates the inability to achieve effective frontal polymerization when utilizing bisphenol derivatives, regardless of the **TI** content. In contrast, **100**ECC formulations exhibited successful frontal polymerization, starting from as low as 2.0 wt% of **TI**. These observations lead to the conclusion that **100**BFDGE formulations are unable to sustain a stable curing front, even at high **TI** concentrations and in the absence of **CPI**'s quenching effect. The integration of these observations with DSC analysis results indicates that the inability of **100**BFDGE formulations to sustain frontal polymerization can be attributed to their higher peak temperatures compared to **100**ECC formulations, which suggest slower reaction kinetics.

Matrix	TI: 0.0 wt%	TI: 2.0 wt%	TI: 8.0 wt%
100BFDGE	X	X	X
100ECC	X	✓	✓

X : stable front not obtained

✓ : stable front and total curing achieved

Table 3.1. Results of thermally induced frontal polymerization experiments conducted on single component epoxy matrices with varying content of **TI** and absence of **CPI**.

3.2.4 Evaluating thermally induced frontal polymerization in mixed epoxy matrices

Having demonstrated that pure **100**BFDGE formulations cannot establish a stable thermal curing front, subsequent investigations focused on exploring formulations composed of blends of **BFDGE** and the more reactive **ECC**.

The previously described experiments were extended to blends of **BFDGE** and **ECC** prepared in a 1:1 weight ratio (**1**BFDGE**1**ECC formulations). These investigations focused on formulations containing 2.0 wt% **TI**, as this concentration had been previously shown to be sufficient for achieving efficient thermally induced frontal polymerization in pure epoxy-based systems. A maximum of 1.0 wt% **CPI** was included to avoid excessively suppressing the reaction's exothermicity.

The results summarized in **Table 3.2** indicate that formulations based solely on an **ECC** matrix retain the ability to undergo thermally initiated frontal polymerization when 1.0 wt% **CPI** is added. This observation is consistent with the data presented in **Figure 3.2b**, which shows that **ECC**-based formulations containing 2.0 wt% **TI** maintain their curing enthalpy when up to 1.0 wt% **CPI** is added.

Additionally, formulations composed of **BFDGE** and **ECC** blended in a 1:1 weight ratio are capable of undergoing thermally initiated frontal polymerization, both in the absence and presence of 1.0 wt% **CPI**.

Matrix	CPI: 0.0 wt%	CPI: 1.0 wt%
100BFDGE	X	X
1BFDGE**1**ECC	✓	✓
100ECC	✓	✓

X : stable front not obtained

✓ : stable front and total curing achieved

Table 3.2. Summary of thermally induced frontal polymerization results for single-component and blended epoxy matrices, prepared with a constant 2.0 wt% **TI** and varying **CPI** content.

Previous observations were combined with DSC analyses performed on uncured formulations. The results indicate that **1**BFDGE**1**ECC formulations exhibit curing enthalpies comparable to those of pure **BFDGE**- and **ECC**-based formulations. When the **CPI** content is 0.0 wt%, the peak temperatures are similar to those of **100**ECC formulations, while with 1.0 wt% **CPI**, the peak temperatures fall between the values observed for the two pure matrices (see **1**BFDGE**1**ECC**0**CPI**2**TI and **1**BFDGE**1**ECC**1**CPI**2**TI in **Table A2.2**, **Appendix information**).

3.2.5 Evaluating photoinduced frontal polymerization on epoxy blends

The next phase of the research shifted towards examining the more intriguing photoinduced thermal frontal polymerization. Effectiveness of photoinduced curing front formation was evaluated directly by exposing localized portions of resins to UV light. The formulated photoresins were placed in sealed transparent glass tubes, which were then positioned horizontally under a UV lamp emitting a broad spectrum of wavelengths, with a primary peak at 365 nm. The tubes were mostly shielded from light, with only a small area at one end exposed to the UV radiation. The tubes were then irradiated until curing was observed, or for a maximum duration of 30 s. (**Figure 3.4**)

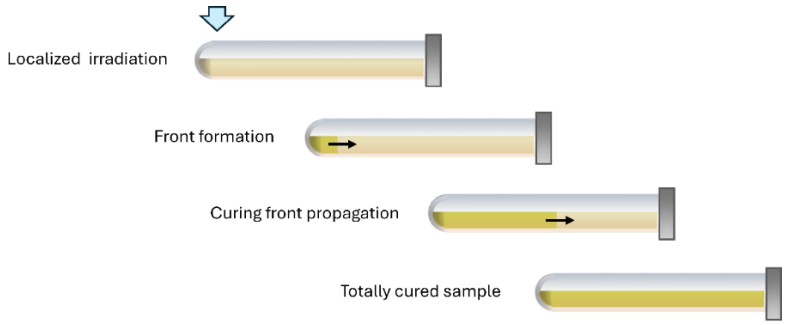

Figure 3.4. Photoinduced frontal polymerization experiment setup.

The results of this second experiment (**Table 3.3**) clearly demonstrate that, as anticipated, formulations lacking **CPI** do not undergo photo-induced frontal polymerization. However, an effective curing front was observed in both **100**ECC and **1**BFDGE**1**ECC photoresins when supplemented with 1.0 wt% **CPI**. While this behavior was also observed in the previously described thermally induced frontal polymerization experiments, these results highlight that the heat generated by localized photoinitiated polymerization triggered by light exposure is sufficient to induce the formation of the curing front.

Matrix	CPI: 0.0 wt%	CPI: 1.0 wt%
100BFDGE	X	X
1BFDGE**1**ECC	X	✓
100ECC	X	✓

X : stable front not obtained

✓ : stable front and total curing achieved

Table 3.3. Summary of photoinduced frontal polymerization results for single-component and blended epoxy matrices, prepared with a constant 2.0 wt% **TI** and varying **CPI** content.

Figure 3.5 presents images capturing the progression of the curing front initiated by localized irradiation of a photoresin formulation consisting of **1**BFDGE**1**ECC, combined

with 2.0 wt% **TI** and 1.0 wt% **CPI**. Once initiated, the curing front progresses steadily at a constant rate of approximately 3.3 cm/min, continuing until the entire resin volume is cured.

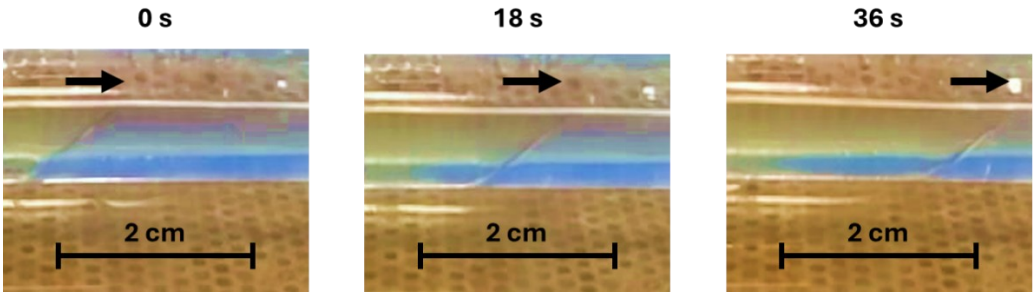

Figure 3.5. Photoinduced curing front progression observed in a **1**BFDGE**1**ECC formulation, supplemented with 2.0 wt% **TI** and 1.0 wt% **CPI**.

3.3 Conclusions

This chapter presented an investigation into the design and evaluation of epoxy-based formulations for efficient frontal polymerization, focusing on both thermally and photo-induced mechanisms. The results demonstrate the critical role of resin composition and initiator concentration in enabling stable curing front formation.

100BFDGE formulations were unable to generate a thermal curing front, even at high concentrations of **TI**, highlighting the need for more reactive components. **ECC**-based formulations, in contrast, exhibited robust thermal frontal polymerization, achieving successful front propagation with as little as 2.0 wt% **TI**. Notably, blending **BFDGE** with **ECC** in a 1:1 weight ratio allowed for effective thermal curing front formation, maintaining performance even with small additions of **CPI** to the blend.

The study was also extended to photo-induced frontal polymerization, where localized UV irradiation successfully initiated curing fronts in both **100**ECC and **1**BFDGE**1**ECC formulations. This behavior underscores the ability of the heat released during photoinitiated polymerization to drive curing front formation, even in formulations with reduced content of the highly reactive **ECC**.

ACKNOWLEDGMENTS

Thanks to Davide Malinverno and Giacomo Bianconi from EUROPE Collecchio (Parma).

3.4 Experimental section

MATERIALS AND METHODS

All reagents were purchased from certified commercial sources and used as received without further purification.

Differential Scanning Calorimetry (DSC) analyses were performed using a DSC250 instrument from the Discovery Series by TA Instruments.

UV irradiation was carried out using a DYMAX ECE 5000 flood lamp equipped with a mercury (Hg) bulb. The lamp emitted a broad spectrum of radiation with a primary peak at 365 nm and a power density of 100 mW/cm^2.

RESIN PREPARATION

The detailed weight ratios and exact quantities of each component used to prepare 100 g of each formulation analyzed in this study are reported in **Table A3.1**.

Resin formulations were prepared by combining all components in a light-shielded vessel and stirring the mixture under reduced pressure until a homogeneous solution was obtained.

DIFFERENTIAL SCANNING CALORIMETRY

DSC experiments were conducted on uncured formulations in an air atmosphere, at a heating rate of 10 °C/min. The thermal curing enthalpy was determined by integrating the area of the exothermic peak observed during the heating phase.

THERMALLY INDUCED FRONTAL POLYMERIZATION EXPERIMENTS

The effectiveness of thermally induced frontal polymerization was evaluated by pouring approximately 15 g of the specified formulations into 25 mL glass tubes. The bottom of the tubes was then heated using a thermal lance until polymerization initiation was observed, or for a maximum duration of 1 min.

PHOTOINDUCED FRONTAL POLYMERIZATION EXPERIMENTS

The effectiveness of photoinduced frontal polymerization was evaluated by pouring approximately 10 g of the specified formulations into 25 mL transparent glass tubes. The tubes were then sealed and positioned horizontally under the UV lamp. The tubes were mostly shielded from light using aluminum foil, leaving only a 3 cm section at one end exposed to UV radiation. Irradiation continued until polymerization was observed or for a maximum duration of 30 s.

3.5 Appendix information

Matrix	BFDGE	ECC	CPI	TI
100BFDGE**0**CPI**2**TI	98 wt% (g)	/	/	2.0 wt% (g)
100BFDGE**1**CPI**2**TI	97 wt% (g)	/	1.0 wt% (g)	2.0 wt% (g)
100BFDGE**2**CPI**2**TI	96 wt% (g)	/	2.0 wt% (g)	2.0 wt% (g)
100BFDGE**4**CPI**2**TI	94 wt% (g)	/	4.0 wt% (g)	2.0 wt% (g)
100BFDGE**4**CPI**0**TI	96 wt% (g)	/	4.0 wt% (g)	/
100BFDGE**4**CPI**8**TI	88 wt% (g)	/	4.0 wt% (g)	8.0 wt% (g)
100BFDGE**0**CPI**8**TI	92 wt% (g)	/	/	8.0 wt% (g)
100ECC**0**CPI**2**TI	/	98 wt% (g)	/	2.0 wt% (g)
100ECC**1**CPI**2**TI	/	97 wt% (g)	1.0 wt% (g)	2.0 wt% (g)
100ECC**2**CPI**2**TI	/	96 wt% (g)	2.0 wt% (g)	2.0 wt% (g)
100ECC**4**CPI**2**TI	/	94 wt% (g)	4.0 wt% (g)	2.0 wt% (g)
100ECC**4**CPI**0**TI	/	96 wt% (g)	4.0 wt% (g)	/
100ECC**4**CPI**8**TI	/	88 wt% (g)	4.0 wt% (g)	8.0 wt% (g)
100ECC**0**CPI**8**TI	/	92 wt% (g)	/	8.0 wt% (g)
1BFDGE**1**ECC**0**CPI**2**TI	49.0 wt% (g)	49.0 wt% (g)	/	2.0 wt% (g)
1BFDGE**1**ECC**1**CPI**2**TI	48.5 wt% (g)	48.5 wt% (g)	1.0 wt% (g)	2.0 wt% (g)

Table A3.1. Weight ratios and absolute masses of components used for the preparation of 100 g of each investigated formulation (abbreviations distinguishing the formulations are not used in the **Results and discussion** section).

It is important to note that **CPI** refers to a 50 wt% solution of hexafluorophosphate sulfonium salt in propylene carbonate, whereas **TI** refers to a 50 wt% solution of N-(4-methoxybenzyl)-N,N-dimethylbenzenaminium hexafluoroantimonate in propylene carbonate.

Matrix	Enthalpy (J/g)	Onset (°C)	Peak Temperature (°C)
100BFDGE**0**CPI**2**TI	530	101	127
100BFDGE**1**CPI**2**TI	176	102	131
100BFDGE**2**CPI**2**TI	193	104	136
100BFDGE**4**CPI**2**TI	101	102	133
100BFDGE**4**CPI**0**TI	/	/	/
100BFDGE**4**CPI**8**TI	370	110	131
100BFDGE**0**CPI**8**TI	520	101	125
100ECC**0**CPI**2**TI	525	88	108
100ECC**1**CPI**2**TI	564	97	123
100ECC**2**CPI**2**TI	329	95	118
100ECC**4**CPI**2**TI	240	93	118
100ECC**4**CPI**0**TI	/	/	/
100ECC**4**CPI**8**TI	266	99	118
100ECC**0**CPI**8**TI	570	91	101
1BFDGE**1**ECC**0**CPI**2**TI	484	88	114
1BFDGE**1**ECC**1**CPI**2**TI	453	95	113

Table A3.2. Enthalpies, onset temperatures, and peak temperatures measured during the thermal curing of the uncured formulations by DSC.

3.6 References

(1) J. P. Fouassier, X. Allonas, D. Burget, Photopolymerization reactions under visible lights: Principle, mechanisms and examples of applications. *Prog. Org. Coat.* **2003**, *47*, 16–36, https://doi.org/10.1016/S0300-9440(03)00011-0.

(2) B. Steyrer, P. Neubauer, R. Liska, J. Stampfl, Visible Light Photoinitiator for 3D-Printing of Tough Methacrylate Resins. *Materials* **2017**, *10*, 1445, https://doi.org/10.3390/ma10121445.

(3) T.Femmer, A. Jans, R. Eswein, N. Anwar, M. Moeller, M. Wessling, A. J. C. Kuehne, High-Throughput Generation of Emulsions and Microgels in Parallelized Microfluidic Drop-Makers Prepared by Rapid Prototyping. *ACS Appl. Mater. Interfaces* **2015**, *7*, 12635–12638, https://doi.org/10.1021/acsami.5b03969.

(4) M. J. Männel, C. Fischer, J. Thiele, A Non-Cytotoxic Resin for Micro-Stereolithography for Cell Cultures of HUVECs. *Micromachines* **2020**, *11*, 246, https://doi.org/10.3390/mi11030246.

(5) M. Buonocore, Adhesive sealing of pits and fissures for caries prevention, with use of ultraviolet light. *J. Am. Dent. Assoc.* **1970**, *80*, 324–330, https://doi.org/10.14219/jada.archive.1970.0061.

(6) H. Lorenz, M. Despont, N. Fahrni, N. LaBianca, P. Renaud, P. Vettiger, SU-8: A low-cost negative resist for MEMS. *J. Micromech. Microeng.* **1997**, *7*, 121–124, https://doi.org/10.1088/0960-1317/7/3/010.

(7) C. Decker, Photoinitiated crosslinking polymerization. *Prog. Polym. Sci.* **1996**, *21*, 593–650, https://doi.org/10.1016/0079-6700(95)00027-5.

(8) P. Garra, C. Dietlin, F. Morlet-Savary, F. Dumur, D. Gigmes, J.-P. Fouassier, J. Lalevée, Photopolymerization processes of thick films and in shadow areas: A review for the access to composites. *Polym. Chem.* **2017**, *8*, 7088–7101, https://doi.org/10.1039/C7PY01778B.

(9) J. A. Pojman, V. M. Ilyashenko, A. M. Khan, Free-radical frontal polymerization: Self-propagating thermal reaction waves. *J. Chem. Soc., Faraday Trans.* **1996**, *92*, 2825-2837, https://doi.org/10.1039/FT9969202825.

(10) I. D. Robertson, M. Yourdkhani, P. J. Centellas, J. E. Aw, D. G. Ivanoff, E. Goli, E. M. Lloyd, L. M. Dean, N. R. Sottos, P. H. Geubelle, J. S. Moore, S. R. White, Rapid energy-efficient manufacturing of polymers and composites via frontal polymerization. *Nature* **2018**, *557*, 223–227, https://doi.org/10.1038/s41586-018-0054-x.

(11) J. A. Pojman, Traveling fronts of methacrylic acid polymerization. *J. Am. Chem. Soc.* **1991**, *113*, 6284-6286, https://doi.org/10.1021/ja00016a063.

(12) J. A. Pojman, S. Popwell, D. I. Fortenberry, V. A. Volpert, Nonlinear dynamics in frontal polymerization. *ACS Symp. Ser.* **2004**, *869*, 106−120, https://doi.org/10.1021/bk-2004-0869.ch009.

(13) K. Bansal, J. A. Pojman, D. Webster, M. Quadir, Frontal polymerization of a thin film on a wood substrate. *ACS Macro. Lett.* **2020**, *9*, 169–173, https://doi.org/10.1021/acsmacrolett.9b00887.

(14) T. Holt, K. Fazende, E. Jee, Q. Wu, J. A. Pojman, Cure-on-demand wood adhesive based on the frontal polymerization of acrylates. *J. Appl. Polym. Sci.* **2016**, *133*, 44064, https://doi.org/10.1002/app.44064.

(15) M. Turani, A. Baggio, V. Casalegno, M. Salvo, M. Sangermano, An Epoxy Adhesive Crosslinked through Radical-Induced Cationic Frontal Polymerization. *Macromol. Mater. Eng.* **2021**, *306*, 2100495, https://doi.org/10.1002/mame.202100495.

(16) M. Ziaee, J. W. Johnson, M. Yourdkhani, 3D Printing of Short-Carbon-Fiber-Reinforced Thermoset Polymer Composites via Frontal Polymerization. *ACS Appl. Mater. Interfaces* **2022**, *14*, 16694–16702, https://doi.org/10.1021/acsami.2c02076.

(17) Z. Zhang, L. Ruochen, L. Wei, L. Yuchen, P. Zhijian, Q. Jingjing, W. Shiren, Frontal polymerization-assisted 3D printing of short carbon fibers/dicyclopentadiene composites. *J. Manuf. Process.* **2021**, *71*, 753-762, https://doi.org/10.1016/j.jmapro.2021.10.014.

(18) E. Goli, N. A. Parikh, M. Yourdkhani, N. G. Hibbard, J. S. Moore, N. R. Sottos, P. H. Geubelle, Frontal polymerization of unidirectional carbon-fiber-reinforced composites. *Compos. - A: Appl. Sci. Manuf.* **2020**, *130*, 105689, https://doi.org/10.1016/j.compositesa.2019.105689.

(19) A. Mariani, S. Bidali, S. Fiori, M. Sangermano, G. Malucelli, R. Bongiovanni, A. Priola, UV-ignited frontal polymerization of an epoxy resin. *J. Polym. Sci., Part A:Polym. Chem.* **2004**, *42*, 2066-2072, https://doi.org/10.1002/pola.20051.

(20) A. D. Tran, T. Koch, P. Knaack, R. Liska, Radical induced cationic frontal polymerization for preparation of epoxy composites. *Compos. - A: Appl. Sci. Manuf.* 2020, *132*, 105855, https://doi.org/10.1016/j.compositesa.2020.105855.

(21) D. Bomze, P. Knaack, T. Koch, H. Jin, R. Liska, Radical induced cationic frontal polymerization as a versatile tool for epoxy curing and composite production. *J. Polym. Sci., Part A:Polym. Chem.* **2016**, 54, 3751-3759, https://doi.org/10.1002/pola.28274.

(22) S. Nakano, T. Endo, Thermal cationic curing with benzylammonium salts. *Prog. Org. Coat.* **1993**, *22*, 287-300, https://doi.org/10.1016/0033-0655(93)80031-5.

(23) S. Nakano, T. Endo, Cationic polymerization of glycidyl phenyl ether by benzylammonium salts. *J. Polym. Sci., Part A: Polym. Chem.* **1995**, *33*, 505-512.

(24) H. Sasaki, Curing properties of cycloaliphatic epoxy derivatives. *Prog. Org. Coat.* **2007**, *58*, 227-230, https://doi.org/10.1016/j.porgcoat.2006.09.030.

Chapter 4

"Sequestration of Anthropogenic Perfluorinated Micropollutants with Quinoxaline-based Cavitands"

4.1 Introduction

4.1.1 PFAS: a challenging class of micropollutants

Poly- and perfluoroalkyl substances (PFAS) are a class of synthetic fluorinated aliphatic compounds, widely utilized across various industrial sectors. The general term PFAS includes both small molecular species and polymers.[1] However, in the literature, the term PFAS is mainly restricted to perfluoroalkyl carboxylic acids and sulfonates, which share a similar structure: $F(CF_2)_nR$, where R represents either a carboxylic acid or sulfonic acid functional group. This subclass of PFAS, featuring a long hydrophobic tail and a small polar functional group, is classified as surfactants.

Due to their exceptional ability to lower surface tension in aqueous solutions, PFAS surfactants are commonly applied in various fields, with significant uses in the manufacture of fluoropolymers, coatings, and aqueous film-forming foams for extinguishing fires involving highly flammable liquids.[2-4]

Recently, this group of PFAS has gained considerable attention from regulatory bodies, such as the drinking water guidelines issued by the United States Environmental Protection Agency (US EPA)[5] and Regulation Directive 2006/122/EC[6], due to their emerging status as environmental pollutants.

The primary concerns associated with PFAS arise from their toxicological effects, which have been linked to various acute and chronic human health conditions. Studies have identified associations between PFAS exposure and diseases such as liver damage, thyroid disorders, asthma, cardiovascular diseases, obesity, anxiety, hyperuricemia, immune toxicity, kidney disorders, and pediatric allergies.[7-9] Furthermore, animal studies have demonstrated additional toxic effects, including carcinogenicity, immunotoxicity, and hormonal disruptions, particularly related to perfluoroalkyl carboxylic acids.[10,11]

Additionally, the remediation of this class of pollutants from wastewater proves challenging[12] due to their exceptional thermal and chemical stability,[13] as well as their resistance to biodegradation,[14] primarily attributed to the remarkable chemical persistence of the strong C-F bonds (513 ± 10 kJ mol^{-1}).

The PFAS surfactant group is divided into short-chain and long-chain compounds. The global regulatory community is particularly focused on long-chain perfluoroalkyl sulfonic acids ($F(CF_2)nSO_3H$, with $n \geq 6$) and carboxylic acids ($F(CF_2)nCOOH$, with $n \geq 7$), along with their corresponding anions.[15] These long-chain PFAS are of greater concern due to their higher bioaccumulation potential compared to short-chain variants. Their increased hydrophobicity facilitates their accumulation in lipophilic biological matrices, making them more persistent in the environment and organisms.[16-18] Nonetheless, recent studies have highlighted that short-chain PFAS, while less bioaccumulative, exhibit comparable levels of toxicity and environmental persistence to their long-chain counterparts.[19]

Perfluorooctane sulfonic acid (**PFOS**) and perfluorooctanoic acid (**PFOA**) are the most extensively studied long-chain perfluoroalkyl acids, frequently highlighted in scientific research due to their widespread occurrence and impact. Notably, they are also the PFAS compounds that have been under regulatory control for the longest time.[20,21] The US EPA has established a drinking water guideline for **PFOA** and **PFOS** at a combined limit of 70 ng/L.

However, despite these regulatory efforts, numerous studies have reported that effluents from wastewater treatment plants often exceed these guidelines, with concentrations of conventional PFAS frequently surpassing 100 ng/L. Furthermore, alternative PFAS introduced as replacements for conventional compounds have also been detected in treated wastewater at comparable concentrations, reaching up to several hundred ng/L.[22-24] This underscores the persistent challenges posed by both traditional and emerging PFAS to water quality and environmental management.

Common treatments, such as Cl_2 or UV radiation, as well as oxidation processes involving O_3 or hydroxyl radicals, have proven ineffective in degrading PFAS. Conversely, methods such as adsorption onto activated carbon, the use of ion-exchange resins, high-pressure nanofiltration, and reverse osmosis membranes have demonstrated greater efficacy.[12] However, the operational conditions required for achieving quantitative PFAS removal are not feasible for large-scale applications, presenting a significant challenge for widespread implementation.[25]

4.1.2 Quinoxaline cavitands: versatile receptors for hydrophobic molecules

Quinoxaline cavitands are a class of organic macrocycles featuring preorganized cavities of molecular dimensions, first introduced by Cram in 1982.[26] From their initial discovery, two principal and stable conformations, the "vase" and "kite" forms, were already observed. The vase conformation exhibits C_{4v} symmetry and is characterized by a continuous concave inner surface formed by the four quinoxaline walls, which are positioned perpendicular to the plane of the eight phenolic oxygen atoms (**Figure 4.1a**). In the kite conformation, the quinoxaline walls move apart from each other, resulting in the loss of the cavity and an open structure. This conformation displays C_{2v} symmetry (**Figure 4.1b**).

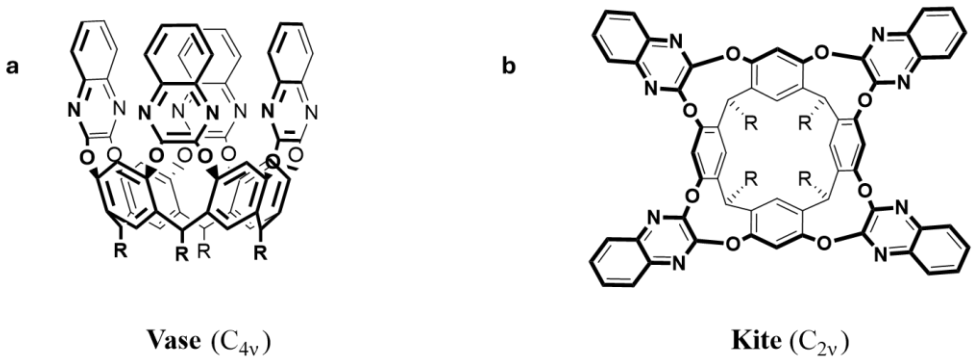

Figure 4.1. Quinoxaline cavitand's **a)** vase and **b)** kite conformations.

The interconversion between the vase and kite conformations of quinoxaline cavitands is influenced by a variety of factors. For example, the temperature dependence of the vase-to-kite equilibrium is governed by the solvation free energy (ΔG_{solv}). In DCM, the vase conformation is preferred at temperatures of 25 °C or higher, while the kite conformation, which exposes a larger surface area of the molecule to the solvent, is stable at -60 °C.[26] This behavior is due to the $T\Delta S_{solv}$ term becoming more significant at lower temperatures. Similarly, acidic conditions tend to favor the kite conformation, as the protonation of the quinoxaline nitrogen atoms causes electrostatic repulsions.[27] Additionally, the presence of Zn^{2+} ions in solution stabilizes the kite form through coordination with the nitrogen atoms, resulting in a 2:1 Zn^{2+}-cavitand complex.[28]

Quinoxaline cavitands, while in their vase conformation, exhibit the ability to complex hydrophobic molecules while in the solid state,[29] in solution,[30] and in gas phase.[31] This conformation preferentially complexes hydrophobic aromatic molecules such as benzene, toluene, ethylbenzene, and xylene (BTEX),[32] as well as polycyclic aromatic hydrocarbons (PAHs),[33] through π-π stacking interactions.

The ability of quinoxaline-based cavitands to complex aliphatic hydrocarbons through CH-π interactions has been demonstrated in aqueous solutions. In such media, these cavitands exhibit a distinct supramolecular behavior, forming dimeric structures known as velcrands. Velcrands consist of two quinoxaline cavitands in the kite conformation, oriented at a 90 ° angle relative to each other. This dimerization occurs via π-π stacking interactions between the quinoxaline walls, effectively minimizing their hydrophobic surfaces' exposure to the surrounding aqueous environment.[34,35] Upon the introduction of aliphatic hydrocarbons as guests, the cavitand conformation switches from the kite form to the vase form. This structural rearrangement facilitates the encapsulation of the hydrophobic guests, which, in turn, stabilize the newly adopted vase conformation.[36]

4.1.3 Sequestration of PFAS using quinoxaline cavitands

Given their ability to reversibly bind hydrophobic molecules through hydrophobic interactions, quinoxaline cavitands represent a promising platform for the sequestration of PFAS. Indeed, perfluoroalkyl carboxylates and sulfonates exhibit exceptional hydrophobicity, which significantly exceeds that of their hydrogenated counterparts in conventional aliphatic surfactants with equivalent chain lengths. This remarkable property is illustrated in **Figure 4.2** (adapted from the literature)[37], where the hydrophobicity of linear perfluorocarboxylates and their corresponding aliphatic carboxylic acids/carboxylates is quantified in terms of the logarithm of the octanol-water partition coefficient (log $P^{O'}$), highlighting the superior affinity of perfluorosurfactants for nonpolar environments.

The log $P^{O'}$ value is a key parameter that has shown a strong correlation with the molecular inclusion capacity of quinoxaline cavitands. Specifically, analyses performed on various guest molecules in aqueous solutions, with concentrations ranging from tens to hundreds μg/L, and using cavitands in the solid phase, demonstrated that a log $P^{O'}$ value of approximately 0.7 serves as the lower threshold for complexation to occur. For guest

molecules with log $P^{O'}$ values greater than 0.95, sequestration efficiencies exceeding 50 % were observed.

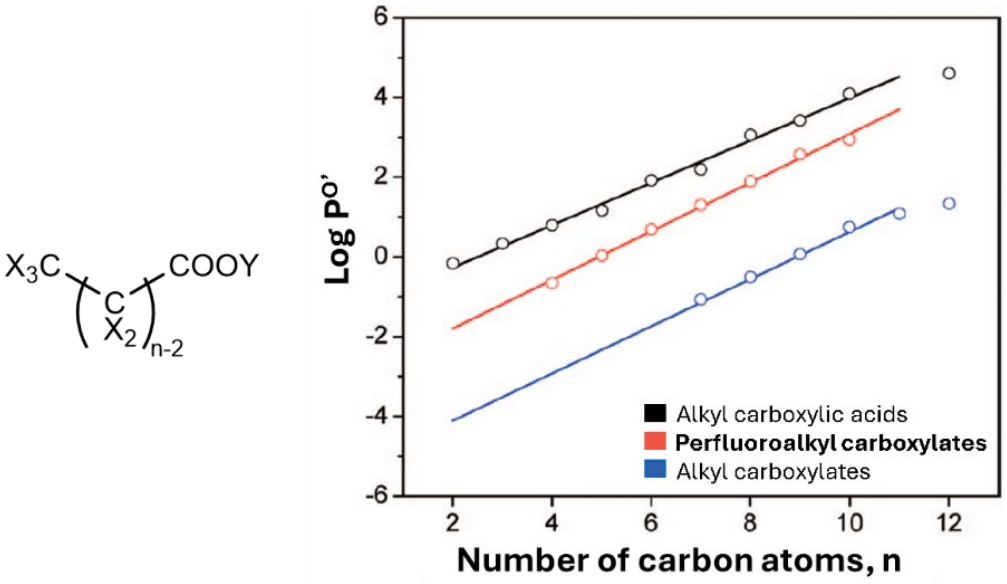

Figure 4.2. Log $P^{O'}$ values for linear perfluorocarboxylates and aliphatic carboxylic acids/carboxylates, with n indicating the number of carbon atoms in the chain.

An additional critical factor for effective complexation is the shape complementarity between host and guest molecules.[38] Notably, cavitands with hydrophobic cavities have been shown to host linear aliphatic hydrocarbon chains of varying lengths, which adopt folded conformations to fit within the cavity.[34,39,40] Similarly, linear PFAS are expected to undergo folding, facilitating their complexation within quinoxaline-based cavitands.

The aim of this study is to evaluate the feasibility of sequestering PFAS of varying chain lengths through hydrophobic interaction-driven complexation using quinoxaline-based cavitands. Additionally, we aim to design novel, tailored receptors for efficient PFAS removal from water. The most effective receptors will then be integrated into a polymeric matrix to create a reusable membrane, as exemplified by Amorini et al.[33]

4.2 Results and discussion

4.2.1 Host-guest NMR titrations in aqueous solutions

The initial phase of the research focused on exploring the potential to complex PFAS in aqueous solution using water-soluble quinoxaline-based cavitands. The complexation is hypothesized to occur via the encapsulation of the lipophilic PFAS chains within the hydrophobic cavity of the quinoxaline-based host, thereby stabilizing the system.

To accomplish this, the three cavitands shown in **Figure 4.3** were synthesized following procedures described in previous PhD theses.[41] Each cavitand is functionalized with four pyridinium groups at its lower rim, providing high water solubility. Among the three cavitands studied, **QxCav4Py** and **BzPyCav4Py** are expected to effectively host PFASs within their deep hydrophobic cavities. In contrast, **MeCav4Py** serves as a control cavitand, as its shallower cavity is not expected to be sufficiently deep to accommodate these compounds.

As discussed in the **Introduction**, **QxCav4Py** and **BzPyCav4Py** adopt velcrand conformations in aqueous solutions, driven by the need to minimize the exposure of their hydrophobic wings to water. A conformational shift from the velcrand to the vase form is anticipated upon the complexation of hydrophobic guest molecules.

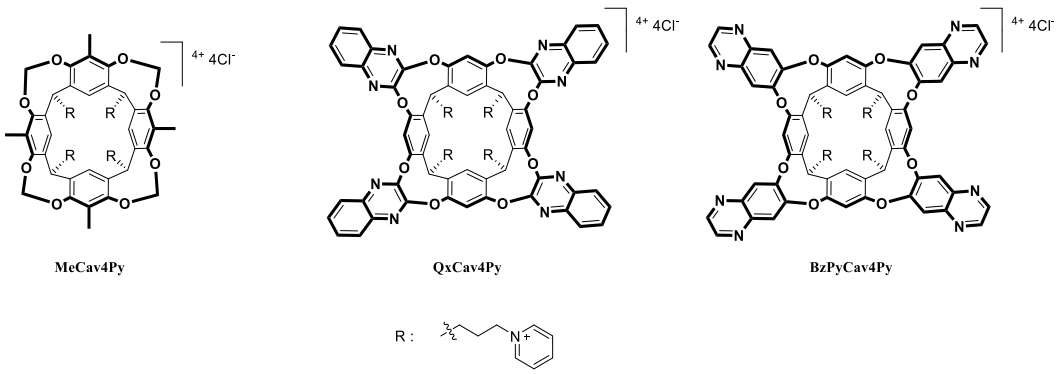

Figure 4.3. Structures of water-soluble cavitands used in NMR titration experiments conducted in D_2O.

The titrations were conducted using sodium perfluorooctanoate (**NaPFO**) as the guest molecule, prepared via the deprotonation of **PFOA** (as detailed in the **Experimental section**), which was chosen as it is one of the most representative PFAS. The decision to preemptively deprotonate **PFOA** was based on the high acidity of perfluorocarboxylic acids, which would significantly alter the pH upon dissolution in water and interfere with the cavitand's vase-kite equilibrium. All titrations were carried out by progressively adding increasing aliquots of a **NaPFO** solution in D_2O to a 1.55 mM cavitand solution in D_2O. Variation of signals was monitored both via ^{1}H and ^{19}F NMR experiments.

The results indicate that, in all cases, a brownish powder begins to precipitate in the tube immediately after the addition of the first 0.25 equivalents of the guest. The fact that both the pure host and guest are water-soluble suggests that their interaction leads to the formation of a water-insoluble adduct. Furthermore, the observation that precipitation also occurs with **MeCav4Py** indicates that this phenomenon is not associated with the presence of the deep hydrophobic cavity, but rather suggests an ionic interaction between the carboxylate group of **NaPFO** and the pyridinium cations at the lower rim of the cavitands.

Notably, a distinct peak at approximately 5.73 ppm emerges in the ^{1}H NMR spectrum of **BzPyCav4Py** only upon the addition of 0.50 cumulative equivalents of **NaPFO**, despite the observed precipitation (**Figure 4.4**).

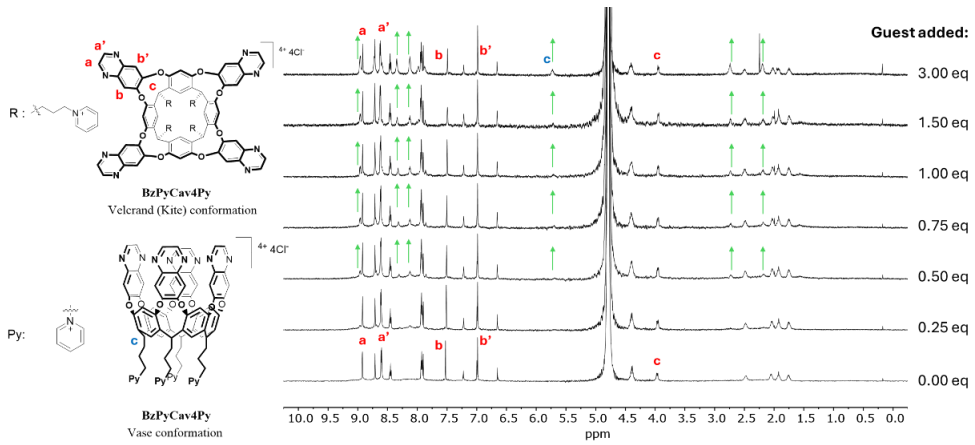

Figure 4.4. Host-guest ^{1}H NMR titration of **BzPyCav4Py** with **NaPFO**, in D_2O, 600 MHz, 25 °C.

This peak is characteristic of the bridging methine groups at the lower rim of the cavitand in its vase conformation, indicating that a portion of the cavitand adopts this conformation in aqueous solution.[36] This behavior is typically associated with guest complexation, which promotes the transition of the velcrand to the vase conformation.[26,35] Furthermore, several new peaks are observed in the aromatic region (downfield), along with two additional peaks in the aliphatic region (upfield). While shifts in the aromatic signals are expected due to the proximity of the quinoxaline walls, the new aliphatic signals might alternatively suggest an interaction between the guest and the alkyl chains at the cavitand's lower rim.

^{19}F NMR spectra collected (**Figure 4.5**) during the titration clearly show upfield-shifted peaks corresponding to the guest molecule. Notably, the extent of the shift increases with the distance of the fluorine atoms from the carboxylate functional group. This observation provides additional evidence supporting the guest complexation hypothesis, suggesting that the hydrophobic tail of **NaPFO** is more likely to be encapsulated within the cavity.

It is important to note that, although signals typically associated with guest complexation are observed, the precipitation prevents determination of the stoichiometric ratio of host and guest molecules involved in the formation of the host-guest complex in solution.

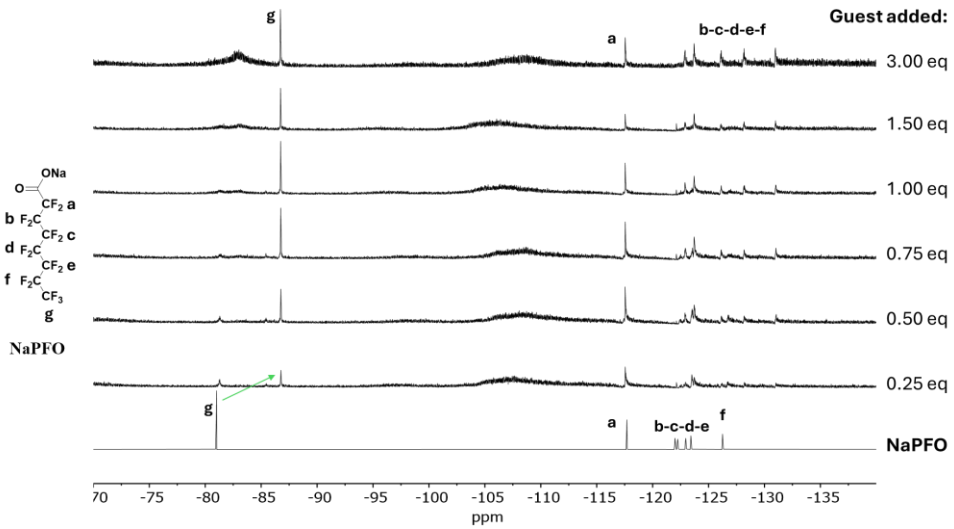

Figure 4.5. Host-guest ^{19}F NMR titration of **BzPyCav4Py** with **NaPFO**, in D_2O, 565 MHz, 25 °C.

As previously anticipated, the results achieved with **BzPyCav4Py** as the host were not reproduced when using **QxCav4Py** or **MeCav4Py** (^{1}H NMR titrations reported in **Figure A4.1** and **Figure A4.2** in **Appendix information** section) and lead to complete precipitation of **NaPFO** added. While it was expected that **MeCav4Py** would not function effectively as a host for **NaPFO**, the reasons for the observed differences between **QxCav4Py** and **BzPyCav4Py** remain unclear.

4.2.2 Study of PFAS sequestration from aqueous solutions with unmodified quinoxaline-based cavitands in solid phase

Following the detection of signals indicative of complexation in the aqueous phase, the study shifted its focus to evaluating the feasibility of sequestering PFAS from aqueous solutions using solid-state quinoxaline-based cavitands. Specifically, the investigation concentrated on three cavitands previously reported in the literature, which synthesis was carried out following procedures described in earlier studies.[26,33,42] The structures of the cavitands are shown in **Figure 4.6**. **QxCav** is a quinoxaline-based cavitand, structurally similar to those previously studied in aqueous solutions, with a cavity depth of 5.8 Å and a cavity volume of 173 Å^3. **BenzoQxCav**, another quinoxaline-based cavitand, features a deeper cavity of 8.3 Å and a larger cavity volume of 226 Å^3, enabling it to accommodate larger hydrophobic molecules such as polyaromatic hydrocarbons.[33] In contrast, **MeCav** serves as a control system, as its cavity is too shallow to form complexes with hydrophobic guests.

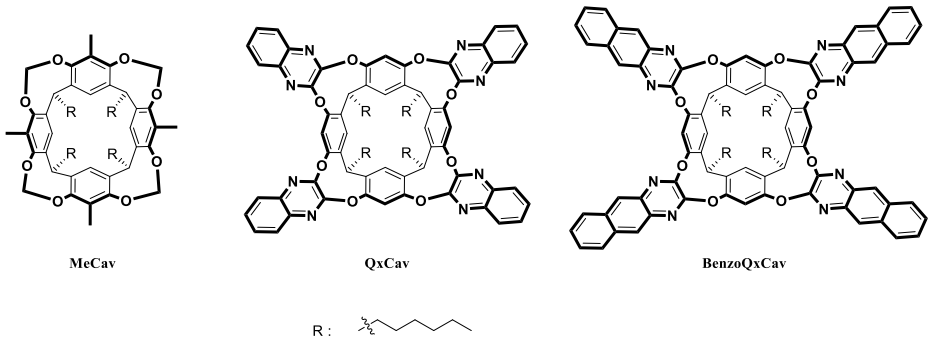

Figure 4.6. Structures of cavitands tested for PFAS removal at the solid-liquid interface.

The sequestration test was performed by suspending a fixed amount of solid cavitand in aqueous solutions containing various PFAS, including both carboxylic and sulfonic acids with different perfluorinated chain lengths. The initial PFAS concentrations were in the scale of 0.1 ppb. Changes in PFAS concentrations in the water after exposure to the cavitands were analyzed using Ultra-high-performance liquid chromatography-high-resolution mass spectrometry (UHPLC-HRMS).

Figure 4.7 and **Figure 4.8** present the results of PFAS concentration reductions after exposure to cavitands. The data reveal a notable similarity in the outcomes for perfluorocarboxylic acids and perfluorosulfonic acids. The findings indicate that removal efficiency is primarily influenced by the perfluorinated chain length, with the impact of the terminal polar group being minimal. The results show comparable performances of **BenzoQxCav** and **QxCav** suggesting that the effect of cavity size on removal efficiency is minimal. Finally, the results demonstrate more efficient removal of PFAS with long perfluorinated chains compared to those with shorter chains. Specifically, using **BenzoQxCav** or **QxCav** achieves removal efficiencies exceeding 80 % for PFAS with a C9 chain, decreasing to between 60 % and 10 % for chain lengths of 8 to 6 units, and dropping below 10 % for PFAS with shorter chains. Furthermore, the significant removal efficiencies of PFAS with chain lengths ranging from C8 to C10 achieved with MeCav suggest that physisorption of PFAS onto the cavitand-based hydrophobic solid phase plays a major role in the process. However, the presence of the cavity in **BenzoQxCav** and **QxCav** substantially enhances the removal efficiency specifically within this chain-length range. For longer-chain PFAS, the contributions of physisorption and cavity interactions become indistinguishable, as removal efficiencies for all three compounds reach quantitative levels.

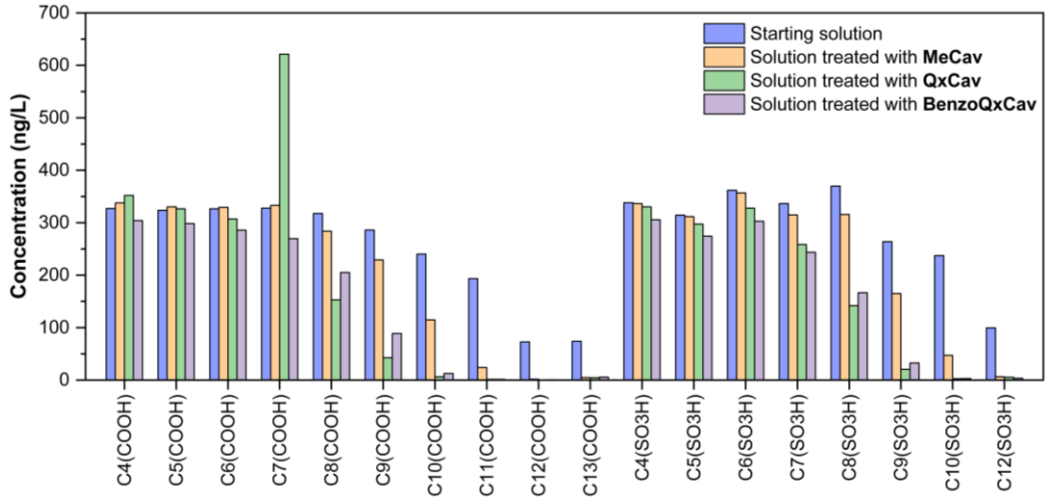

Figure 4.7. Absolute concentrations of PFAS, including carboxylic and sulfonic acids with different perfluorinated chain lengths, measured before and after cavitand treatment.

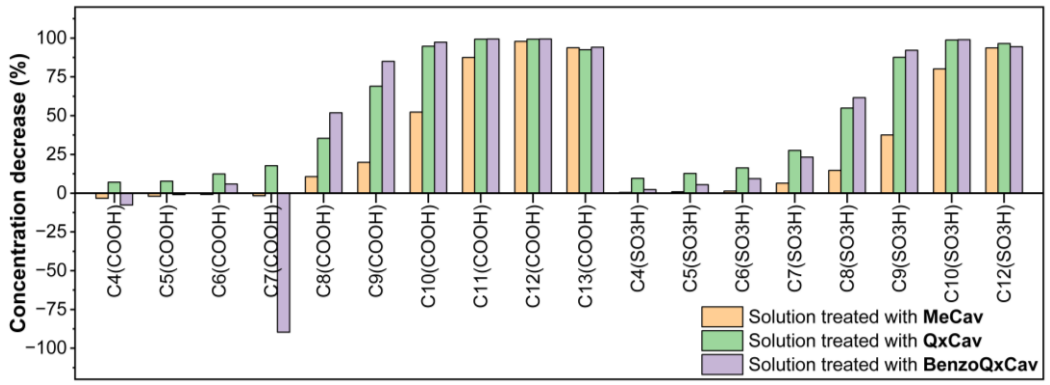

Figure 4.8. Reduction in the concentrations of PFAS, including carboxylic and sulfonic acids with varying perfluorinated chain lengths, observed after treatment with cavitands.

Figure 4.9 compares the removal efficiencies of perfluorocarboxylates with varying chain lengths to their corresponding calculated log $P^{O'}$ values, highlighting a correlation between removal efficiency and the lipophilicity of the tested PFAS. The analyses presented herein are consistent with previous observations,[29] confirming that removal efficiencies of at least

10 % are associated with a log $P^{O'}$ lower threshold in the range of 0.5 to 1.5. This correlation emphasizes that unmodified quinoxaline-based cavitands are more effective at capturing perfluorinated micropollutants with higher hydrophobicity, underscoring the need to design tailored receptors for the sequestration of more hydrophilic short-chain PFAS.

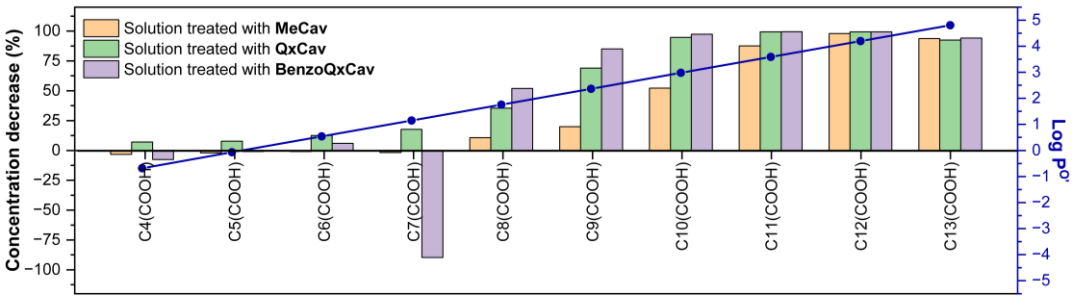

Figure 4.9. Reduction in the concentrations of PFAS carboxylic acids with varying perfluorinated chain lengths after treatment with cavitands, plotted against their respective log $P^{O'}$ values.

4.2.3 Synthesis of quinoxaline cavitands functionalized with permanently positively charged upper rim substituents

The results presented highlight the particular challenge posed by short-chain PFASs, which are more difficult to remove due to their lower hydrophobicity. Among the various strategies proposed to address this issue, combining hydrophobic and ionic interactions has shown significant potential. This dual strategy was demonstrated by Dichtel and co-workers,[43] who copolymerized a styrene-based monomer functionalized with a positively charged cyclodextrin alongside other monomers. The resulting polymer effectively achieved quantitative removal of PFAS at an initial concentration of 1 µg/L by leveraging a combination of electrostatic and hydrophobic interactions. More recently, Sanchez-Lievanos et al. developed cationic porphyrin-based nanocages capable of efficiently capturing both short- and long-chain PFASs, with the added advantage of multiple regeneration cycles.[44]

Building on this concept, we designed a novel receptor, **QAQxCav**, which features a deep hydrophobic cavity, effective for capturing long-chain PFAS, and a quaternary ammonium group to facilitate ionic interactions with negatively charged surfactants. The synthesis of **QAQxCav** was accomplished through the multistep protocol outlined in **Scheme 4.1**.

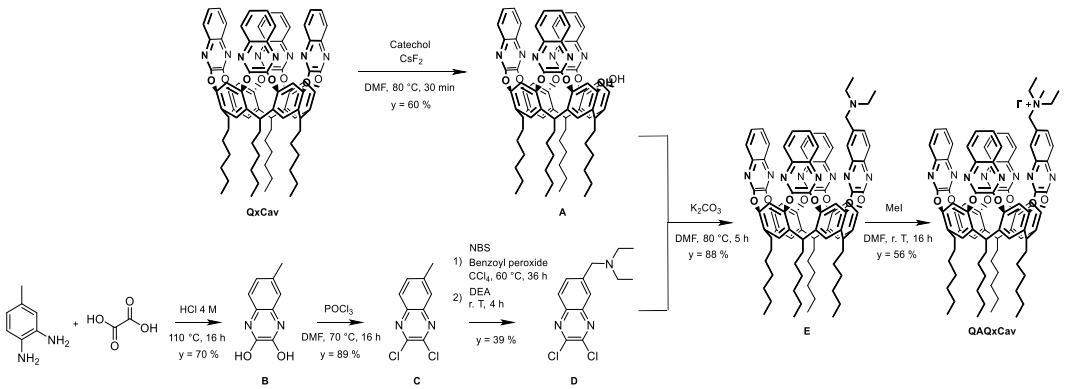

Scheme 4.1. Synthethic pathway to **QAQxCav**.

The synthesis of **QAQxCav** was initiated from the well-known compound **QxCav**, the synthesis of which is extensively documented in the literature and will not be detailed here.[6] **QxCav** was selectively modified by removing a single quinoxaline wall, producing intermediate **A**, following a previously reported procedure.[9]

Quinoxaline **D**, which features a tertiary benzyl amine, was synthesized in a three-step process. First, an acid-catalyzed condensation between 3,4-diaminotoluene and oxalic acid was performed to form intermediate **B**. Next, the hydroxy groups of **B** were chlorinated to generate intermediate **C**. Finally, **C** underwent monobromination at the benzyl carbon, followed by nucleophilic substitution of the resulting benzyl bromide with diethylamine (DEA), yielding quinoxaline **D**.

The reaction between intermediates **A** and **D** then resulted in the formation of cavitand **E**, which contains a tertiary amine at the upper rim. Finally, cavitand **E** was alkylated with methyl iodide (MeI) to yield **QAQxCav**, incorporating the desired quaternary ammonium group at the upper rim.

QAQxCav was subsequently characterized using various spectroscopic techniques, including ^{1}H and COSY, ^{13}C NMR, DEPT135, and HSQC, as well as ESI-MS.

The ^{1}H NMR spectrum of **QAQxCav** is shown in **Figure 4.10**. The most diagnostic signals are two doublets corresponding to the H_5 protons, which become diastereotopic upon the attachment of the monofunctionalized quinoxaline **D** to substrate **A**, forming a planary chiral cavitand **E**. The loss of symmetry following this attachment complicates the fine interpretation of the aromatic region of the spectrum. Additionally, the spectrum displays four adjacent multiplets centered around 3.5 ppm, corresponding to the H_1 and H_2 methylene protons. These protons also become diastereotopic, because of the planar chirality of **QAQxCav**.

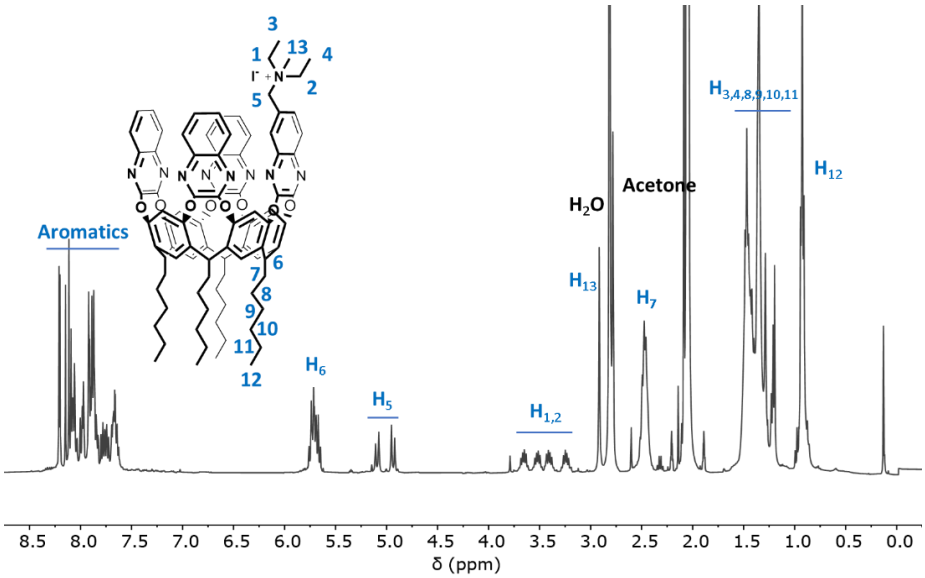

Figure 4.10. ^{1}H NMR spectrum of **QAQxCav**, in acetone-d6, 600 MHz, 25 °C.

Additional characterizations conducted using NMR are available in from **Figures A4.3** to **A4.6** in **Appendix information** section)

Further confirmation of the successful synthesis is provided by the ESI-MS analysis shown in **Figure 4.11**. The results clearly confirm the formation of **QAQxCav**, detected exclusively as the molecular ion and its adduct with a MeOH molecule.

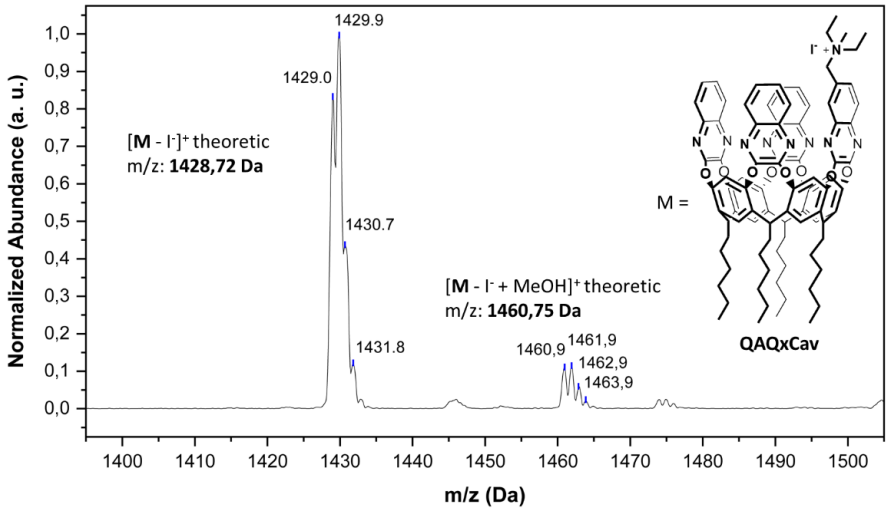

Figure 4.11. ESI-MS analysis of **QAQxCav** dissolved in MeOH, conducted in positive ionization mode.

4.2.4 Study of PFAS sequestration from aqueous solutions with QAQxCav in solid phase

Using a similar approach to that applied with unmodified quinoxaline-based cavitands, the ability of **QAQxCav** to sequester PFAS from aqueous solutions was investigated. **QAQxCav** was suspended in a complex PFAS mixture, with each PFAS solubilized at a concentration of 1 ppm. Changes in PFAS concentrations were measured using UHPLC-HRMS. Notably, **QAQxCav** displayed a strong propensity to localize at the liquid-air interface when dispersed in water, preventing sedimentation via centrifugation and necessitating filtration. This requirement introduced the possibility of interactions between the filter and the PFAS solution, potentially interfering with the data presented in **Figure 4.12**.

Despite being affected by significant experimental error, preliminary results for **QAQxCav** showed a removal efficiency exceeding 99 % for all analytes, regardless of their chain length. This promising outcome underscores the critical role of **QAQxCav**'s permanent positive charge in enhancing the removal efficiency of both long-chain and short-chain PFAS.

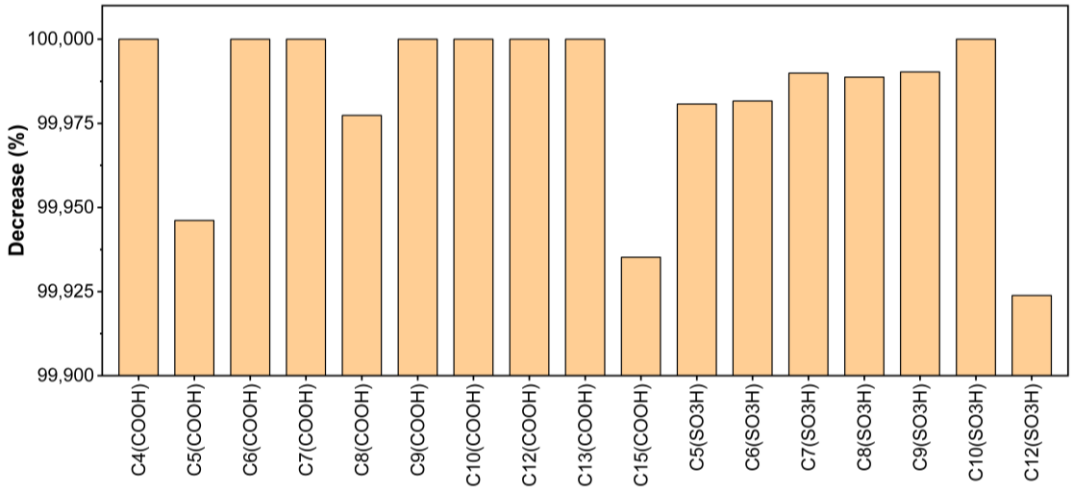

Figure 4.12. Reduction in the concentrations of PFAS, including carboxylic and sulfonic acids with varying perfluorinated chain lengths, observed after treatment with cavitands.

Notably, testing higher initial PFAS concentrations in aqueous solutions could help to better differentiate the removal efficiencies between long-chain and short-chain PFAS. Furthermore, a more in-depth investigation involving competitive negatively charged analytes would provide valuable insights into whether the hydrophobic cavity still contributes to the complexation of PFAS with **QAQxCav**, or if the sequestration is driven exclusively by ionic interactions.

4.3 Conclusions

In summary, the ability of quinoxaline cavitands to remove PFAS from aqueous solutions was evaluated using several methodologies.

Specifically, NMR titrations in water indicated that complexation between water-soluble quinoxaline-based cavitands and PFOA may occur, although the analyses were significantly affected by salt precipitation.

Additionally, studies on the sequestration of PFAS from aqueous solutions using unmodified quinoxaline-based cavitands revealed that the removal efficiency is strongly influenced by the hydrophobicity of the pollutants. Efficient removal of short-chain PFAS requires the

development of new, tailored receptors. To this purpose, **QAQxCav**, a new quinoxaline cavitand featuring a quaternary ammonium ion at the upper rim, was designed, successfully synthesized, and characterized.

Preliminary tests on solid **QAQxCav** demonstrated an improved capacity to remove PFAS from aqueous solutions, regardless of their chain length, emphasizing the role of ionic interactions. Additionally, testing with higher PFAS concentrations could help distinguish the removal efficiencies for long-chain and short-chain PFAS. Further investigation, incorporating competitive negatively charged analytes, would provide insight into whether the hydrophobic cavity plays a role in PFAS complexation, or if sequestration is primarily driven by ionic interactions.

Future studies will focus on integrating cavitand **QAQxCav** into a polymeric matrix to evaluate its ability to reversibly sequester PFAS from contaminated water.

ACKNOWLEDGMENTS

Thanks to Dr. Nicolò Riboni and to Prof. Federica Bianca from University of Parma for their contributions to the analysis of PFAS sequestration from aqueous solutions using solid cavitands.

4.4 Experimental section

MATERIALS AND METHODS

All substances were purchased from certified commercial sources and used as received, without further purification. The solvents designated as anhydrous are treated according to procedures well-established in the literature.[9-11]

NMR spectra, including ^{1}H, COSY, ^{13}C, DEPT135, and HSQC, were recorded on a Bruker AVANCE 400 MHz or on a Jeol 600 MHz spectrometer using $CDCl_3$, DMSO-d_6, D_2O, or acetone-d_6 as solvents. All chemical shifts (δ) are reported in parts per million (ppm), referenced either to the residual proton resonances from incomplete deuteration of the NMR solvents or to the solvent's ^{13}C resonance. The abbreviations: s, d, dd, t and m indicate the spectrum peaks referred to: singlet, doublet, doublet of doublets, triplet and multiplet, respectively. The b that eventually precedes the abbreviations means broad.

Electrospray ionization mass spectrometry (ESI-MS) analyses were performed using either an Infusion Waters Acquity Ultra Performance LC HO6UPS-823M instrument equipped with an electrospray ionization (ESI) source operating in positive mode or an Agilent 1260 Infinity II system with an ESI source also configured in positive mode.

Gas chromatography-mass spectrometry (GC-MS) analyses were conducted using an Agilent Technologies 6890N Network GC System, ensuring precise and reliable performance.

Ultra-high-performance liquid chromatography-high-resolution mass spectrometry (UHPLC-HRMS) analyses were carried out using a Phenomenex Luna Omega PS C18 column.

PERFLUOROOCTANOIC ACID DEPROTONATION PROTOCOL

500 mg of perfluorooctanoic acid (1.21 mmol) are dissolved in 1 mL of water. Separately, 48.3 mg of NaOH (1.21 mmol) are dissolved in 1 mL of water. The NaOH solution is added dropwise to the perfluorooctanoic acid solution under stirring, and the mixture is stirred for 10 min to ensure complete homogenization. The solvent is then removed under reduced pressure, yielding **NaPFO** as a white solid.

^{1}H AND ^{19}F HOST-GUEST NMR TITRATIONS PROCEDURE

1.09 μmol of host (water soluble cavitand) are solubilized in 700 μL of D_2O. 600 μL of the resulting solution (0.93 μmol of host) are poured in an NMR tube. Separately, 2.02 mg (4.64 μmol) of **NaPFO** (guest) are solubilized in 250 μL di D_2O. Progressive additions of aliquots from the guest solution to the host solution are performed, and ^{1}H and ^{19}F NMR spectra are recorded after each addition.

PFAS SEQUESTRATION FROM AQUEOUS SOLUTIONS WITH UNMODIFIED QUINOXALINE-BASED CAVITANDS IN SOLID PHASE

10 mg of cavitand were suspended in 10 mL of water containing a mixture of PFAS carboxylates and sulfonates with varying chain lengths, pre-solubilized to achieve final concentrations on the order of 10^{-1} ppb. The suspension was subjected to sequential vortexing and centrifugation to promote cavitand sedimentation. Aliquots of the PFAS solution were collected, injected, and analyzed using UHPLC-HRMS. Changes in PFAS concentrations after cavitand exposure were assessed relative to a blank, untreated sample. Each analysis was performed in triplicate to ensure reproducibility.

SYNTHESIS OF **QAQxCAV**

The following is a detailed description of all the steps involved in the synthesis of **QAQxCav**, as illustrated in **Scheme 4.1** in the **Results and Discussion** section.

Intermediate **A** - In anhydrous conditions, 500 mg (0.376 mmol) of **QxCav** is suspended in 80 mL of DMF. CsF (1.14 g, 7.52 mmol) is added to the suspension, and the resulting mixture is stirred and heated at 80 °C. Separately, a solution of pyrocatechol (45.5 mg, 0.414 mmol) in anhydrous DMF (20 mL) is prepared and added dropwise to the reaction mixture. The reaction mixture is maintained at 80 °C under continuous stirring for an additional 30 min. The mixture is then poured into 500 mL of ice-cold saturated aqueous NaCl solution, a white precipitate is formed. The suspension is filtered to separate the solid, which is washed with water and purified by flash chromatography using a gradient elution

from pure DCM to DCM-EtOAc (95:5). After solvent evaporation, 270 mg (0.376 mmol, 60 % yield) of pure **A** is obtained as a white solid.

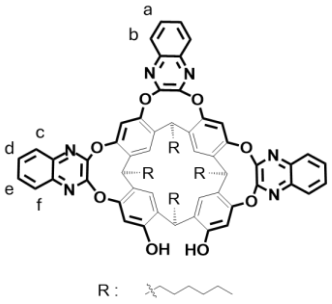

Figure 4.12. Molecular structure of intermediate **A**.

^{1}H NMR (400 MHz, $CDCl_3$): δ ppm = 8.27 (s, 2H, Ar**H$_{up}$** away from OHs), 7.96 (dd, 2H, **H$_f$**, J = 8.3 Hz, 1.4 Hz), 7.85 (m, 2H, H_a), 7.71 (dd, 2H, H_d, J = 8.4 Hz, 1.4 Hz), 7.59 (m, 2H, H_e), 7.51 (m, 4H, H_b + H_c), 7.28 (s, 2H, Ar**H$_{down}$** away from OHs), 7.16 (s, 2H, Ar**H$_{down}$** close to OHs), 7.11 (s, 2H, Ar**H$_{up}$** close to OHs), 5.62 (t, 1H, C**H**CH_2- away from OHs, J = 8.1 Hz), 5.54 (t, 2H, C**H**CH_2-, J = 8.1 Hz), 4.29 (t, 1H, C**H**CH_2- close to OHs, J = 7.7 Hz), 2.26 (m, 8H, CHC**H$_2$**-), 1.34 (m, 32H, -C**H$_2$**C**H$_2$**C**H$_2$**C**H$_2$**CH_3), 0.93 (m, 12H, -CH_2CH_2C**H$_3$**).

Intermediate **B** - 3,4-Diaminotoluene (3.00 g, 24.0 mmol) and oxalic acid (2.65 g, 29.0 mmol) are dissolved in 45 mL of 4 M aqueous HCl solution. The mixture is heated to 110 °C under stirring for 72 h, during which a grey precipitate forms. After that time, the suspension is cooled to room temperature. The resulting solid is collected by filtration and washed with water until the filtrate reaches a neutral pH. 2.96 g (16.8 mmol, 70 % yield) of pure intermediate **B** are collected as a grey powder.

^{1}H NMR (400 MHz, DMSO-d_6): δ ppm =11.87 (s, 1H, -O**H** in 2 position), 11.85 (s, 1H, -O**H** in 3 position), 7.01 (d, 1H, Ar**H** in 8 position, J = 7.9 Hz), 6.91 (m, 2H, Ar**H** in 5 and 7 positions), 2.27 (s, 3H, -CH_3).

GC-MS: $[M - Cl^-]^+$ ($C_9H_6Cl_2N_2^+$) theoretical m/z: 211.99 Da, experimental: 212.00 Da;

Intermediate **C** - Under anhydrous conditions, 600 mg (3.41 mmol) of intermediate **B** are dissolved in 12 mL of DMF. 3.00 mL (32.1 mmol) of phosphorus oxychloride ($POCl_3$) is then added, and the reaction mixture is heated to 50 °C under stirring for 16 h. After completion, the mixture is allowed to cool to room temperature, and 5 mL of MeOH are added to hydrolyze the residual $POCl_3$. The solvent is then evaporated under reduced pressure. The resulting solid is washed with water, filtered, and extracted with DCM. The organic phase is separated and dried with Na_2SO_4, the solvent is removed under reduced pressure to afford 647 mg (3.03 mmol, 89 % yield) intermediate **C** as an orange solid.

^{1}H NMR (400 MHz, $CDCl_3$): δ ppm = 7.92 (d, 1H, ArH in 8 position, J = 8.6 Hz), 7.80 (s, 1H, ArH in 5 position), 7.64 (dd, 1H, ArH in 7 position, J = 8.6 Hz, 1.9 Hz), 2.60 (s, 3H, -CH_3).

GC-MS: $[M + H^+]^+$ ($C_9H_9N_2O_2^+$) theoretical m/z: 177.07 Da, experimental: 177.07 Da; $[M + HCl - e^-]^+$ ($C_9H_9ClN_2O_2^+$) theoretical m/z: 212.04 Da, experimental: 212.07 Da.

Intermediate **D** - Under anhydrous conditions, 400 mg (1.88 mmol) of intermediate **C** are dissolved in 50 mL of CCl_4. 418 mg (2.35 mmol) of N-bromosuccinimide (NBS) are added, followed by a catalytic amount of benzoyl peroxide. The suspension obtained is degassed and stirred at 60 °C for 36 h. After that time, solvent is evaporated, and the crude product is suspended in 3 mL of diethylamine (DEA). The suspension is stirred at room temperature for 4 h. The solvent is then evaporated, and the product is purified by flash column chromatography using a gradient elution from pure DCM to a mixture of DCM and MeOH in a 96:4 ratio. 206 mg (0.724 mmol, 39 % yield) of the desired product **D** are obtained as a yellow oil.

^{1}H NMR (400 MHz, $CDCl_3$): δ ppm = 7.97 (m, 2H, Ar**H** in 5 and 7 positions), 7.87 (d, 1H, Ar**H** in 8 position, J = 8.6 Hz), 3.77 (s, 2H, -C**H$_2$**N(CH_2CH_3)$_2$), 2.57 (q, 4H, -N(C**H$_2$**CH_3)$_2$, J = 7.1 Hz), 1.06 (t, 6H, -N(CH_2C**H$_3$**)$_2$, J = 7.1 Hz).

^{13}C NMR (101 MHz, $CDCl_3$): δ ppm = 132.57 (Ar**C** in 7 position), 127.82 (Ar**C** in 8 or 5 position), 126.98 (Ar**C** in 8 or 5 position), 57.36 (Ar**C**H_2-), 47.13 (-**C**H_2CH_3), 11.97 (-CH_2**C**H_3).

GC-MS: $[M - N(CH_2CH_3)_2^-]^+$ ($C_9H_5Cl_2N_2^+$) theoretical m/z: 210.98 Da, experimental: 211.05 Da; $[M - CH_3^-]^+$ ($C_{12}H_{12}Cl_2N_3^+$) theoretical m/z: 268.04 Da, experimental: 268.08 Da; $[M - e^-]^+$ ($C_{13}H_{15}Cl_2N_3^+$) theoretical m/z: 283.06 Da, experimental: 283.08 Da.

Intermediate **E** – 35.4 mg (0.125 mmol) of intermediate **D** are dissolved in 1.3 mL of DMF in anhydrous conditions. 125 mg (0.104 mmol) of intermediate **A** and 28.7 mg (0.208 mmol) of K_2CO_3 are added. The suspension obtained is stirred at 80 °C. After 5 h, the solvent is evaporated under reduced pressure, and the resulting solid is washed with water and collected by filtration. The product is then purified by flash column chromatography using a gradient elution from pure DCM to a mixture of DCM and MeOH in a 9:1 ratio. 111 mg (0.104 mmol, 76 yield) of pure **E** are collected as a yellow powder.

^{1}H NMR (400 MHz, Acetone-d_6): δ ppm = 8.20 (m, 4H, Ar**H$_{up}$**), 7.92 and 7.64 (two bm, 15H, Ar**H** of quinoxaline walls), 7.83 (m,4H, Ar**H$_{down}$**), 5.69 (m, 4H, C**H**CH_2-), 3.80 (d, 1H, -C**H$_2$**'$N(CH_2CH_3)_2$, J = 14.1 Hz), 3.58 (d, 1H, -C**H$_2$**''$N(CH_2CH_3)_2$, J = 14.1 Hz), 2.42 (bm, 12H, CHC**H$_2$**- and -$N(CH_2CH_3)_2$), 1.37 (bm, 32H, -C**H$_2$**C**H$_2$**C**H$_2$**C**H$_2$**CH_3), 0.92 (bm, 18H, -CH_2CH_2C**H$_3$** and -$N(CH_2CH_3)_2$).

^{13}C NMR (101 MHz, Acetone-d_6): δ ppm = 153.23, 143.88, 140.33, 137.03, 131.20, 130.04, 128.67, 127.15, 125.54, 119.30, 58.06, 47.54, 35.14, 32.63, 28.80, 23.26, 14.26, 12.40.

ESI-MS: $[M + H^+]^+$ ($C_{89}H_{92}N_9O_8^+$) theoretical m/z: 1414.71 Da, experimental: 1414.72 Da; $[M + NH_4^+]^+$ ($C_{89}H_{95}N_{10}O_8^+$) theoretical m/z: 1431.73 Da, experimental: 1431.88 Da.

QAQxCav - 205.6 mg (0.145 mmol) of intermediate **E** are dissolved in anhydrous DMF under dry conditions, and 0.27 mL (4.4 mmol) of methyl iodide (MeI) are added to the solution. The mixture is stirred at room temperature for 16 h. The solvent is then evaporated under reduced pressure. The resulting solid is washed with abundant water and collected by filtration. The product is purified by flash column chromatography with a gradient elution from pure dichloromethane (DCM) to a mixture of DCM and MeOH in a ratio of 8:2. After solvent removal, 125.8 mg (0.145 mmol, 56 % yield) of **QAQxCav** are recovered as a yellow powder.

^{1}H NMR (600 MHz, Acetone-d_6): δ ppm = 8.11, 7.86 and 7.66 (three bm, 23H, Ar**H**), 5.67 (m, 4H, C**H**CH_2-), 5.15 (d, 1H, -C**H$_2$**'N(CH_2CH_3)$_2$, J = 12.8 Hz), 4.95 (d, 1H, -C**H$_2$**''N(CH_2CH_3)$_2$, J = 12.8 Hz), 3.65, 3.48, 3.34 and 3.16 (four m, 4H, -N(CH_3)(C**H$_2$**CH_3)$_2$), 2.84 (s, 3H, -N(C**H$_3$**)(CH_2CH_3)$_2$), 2.46 (m, 8H, CHC**H$_2$**-), 1.37 (bm, 32H, -C**H$_2$**C**H$_2$**C**H$_2$**C**H$_2$**CH_3), 1.26 and 1.11 (two bt, 6H, , -N(CH_3)(CH_2C**H$_3$**)$_2$), 0.90 (bt, 12H, -CH_2CH_2C**H$_3$**).

^{13}C NMR (151 MHz, Acetone-d_6): δ ppm = 153.03, 140.21, 137.40, 134.20, 133.52, 131.27, 130.57, 128.95, 128.54, 126.34, 125.62, 119.10, 64.46, 56.98, 56.36, 46.89, 35.28, 32.90, 32.63, 29.93, 28.79, 23.24, 14.25, 8.56.

ESI-MS: $[M - I^-]^+$ ($C_{90}H_{94}N_9O_8^+$) theoretical m /z: 1428.72 Da, experimental: 1429.0 Da; $[M - I^-]^+$ ($C_{90}H_{94}N_9O_8^+$) theoretical m /z: 1460.75 Da, experimental: 1460.9 Da.

PFAS SEQUESTRATION FROM AQUEOUS SOLUTIONS WITH QAQXCAV IN SOLID PHASE

5 mg of cavitand were suspended in 10 mL of water containing a mixture of PFAS carboxylates and sulfonates with varying chain lengths, pre-solubilized to achieve final concentrations of 1 ppm each. The suspension was subjected to sequential vortexing and centrifugation to promote the sedimentation of the cavitand. Aliquots of the PFAS solution were collected, injected, and analyzed using UHPLC-HRMS. Changes in PFAS concentrations after cavitand exposure were assessed relative to a blank, untreated sample. Each analysis was performed in duplicate.

4.5 Appendix information

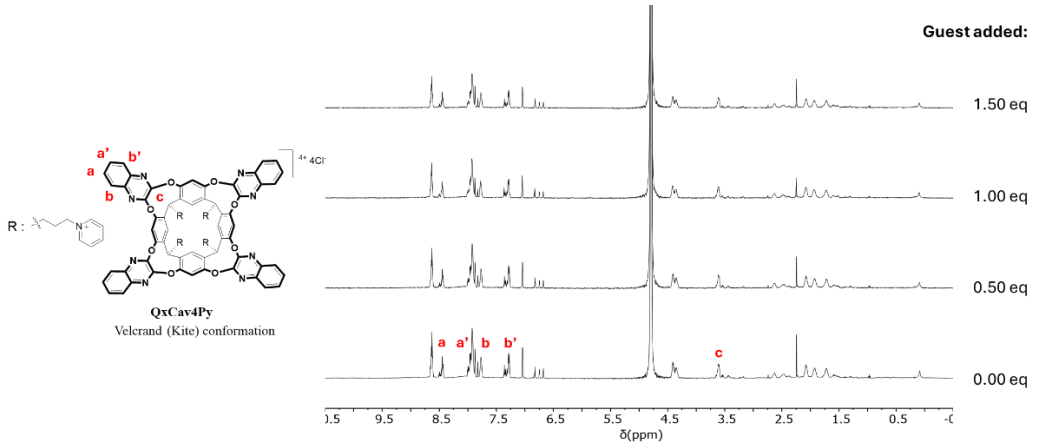

Figure A4.1. Host-guest ^{1}H NMR titration of **QxCav4Py** with **NaPFO**, in D_2O, 600 MHz, 25 °C.

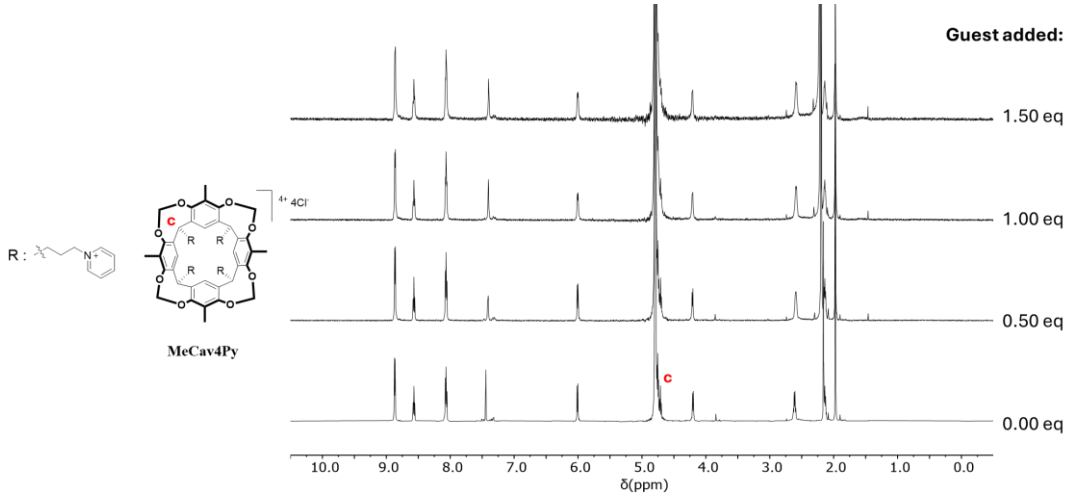

Figure A4.2. Host-guest ^{1}H NMR titration of **MeCav4Py** with **NaPFO**, in D_2O, 600 MHz, 25 °C.

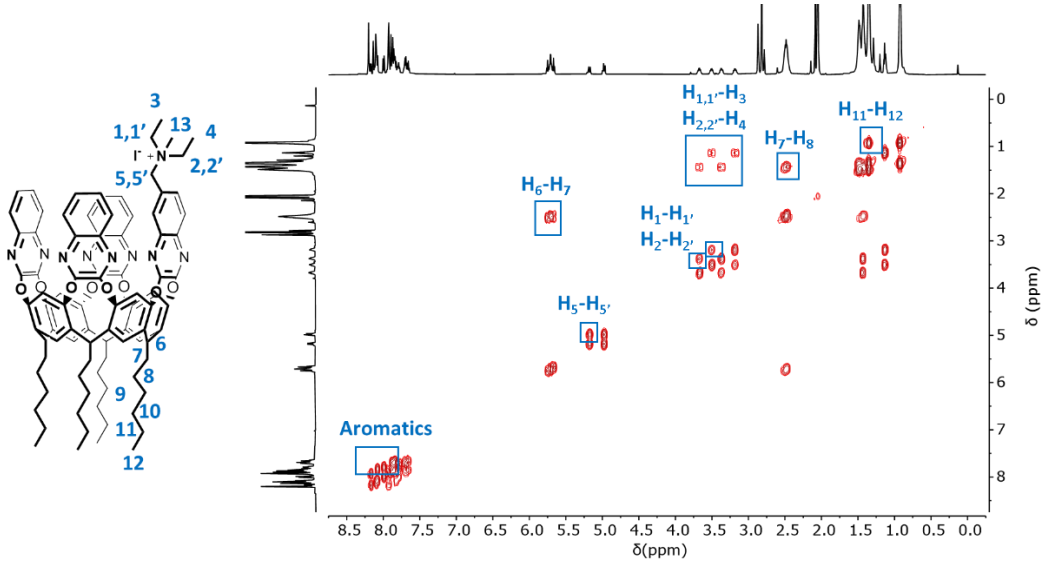

Figure A4.3. COSY NMR spectrum of **QAQxCav**, in acetone-d6, 600 MHz, 25 °C.

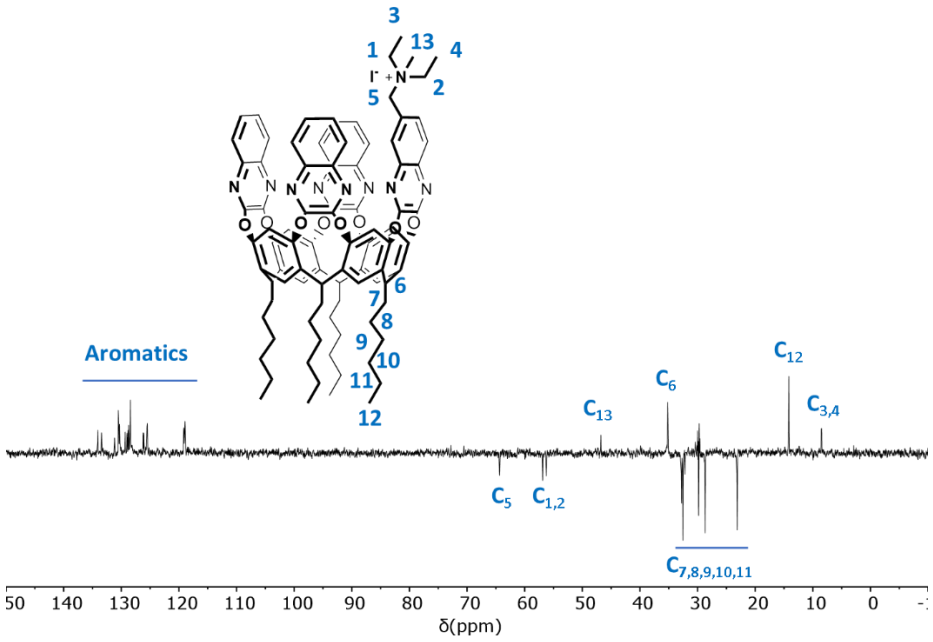

Figure A4.4. DEPT135 NMR spectrum of **QAQxCav**, in acetone-d6, 151 MHz, 25 °C.

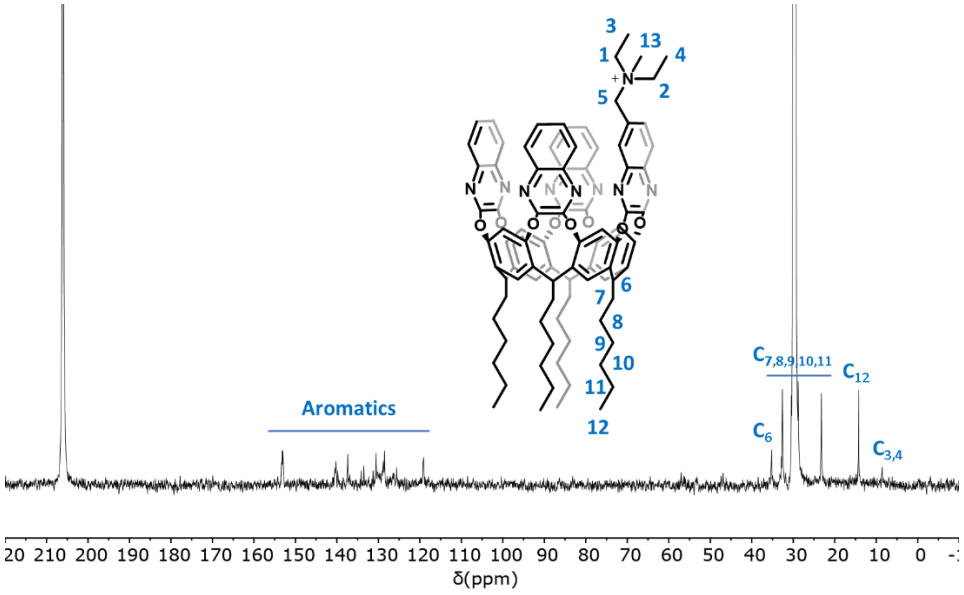

Figure A4.5. ^{13}C NMR spectrum of **QAQxCav**, in acetone-d6, 151 MHz, 25 °C.

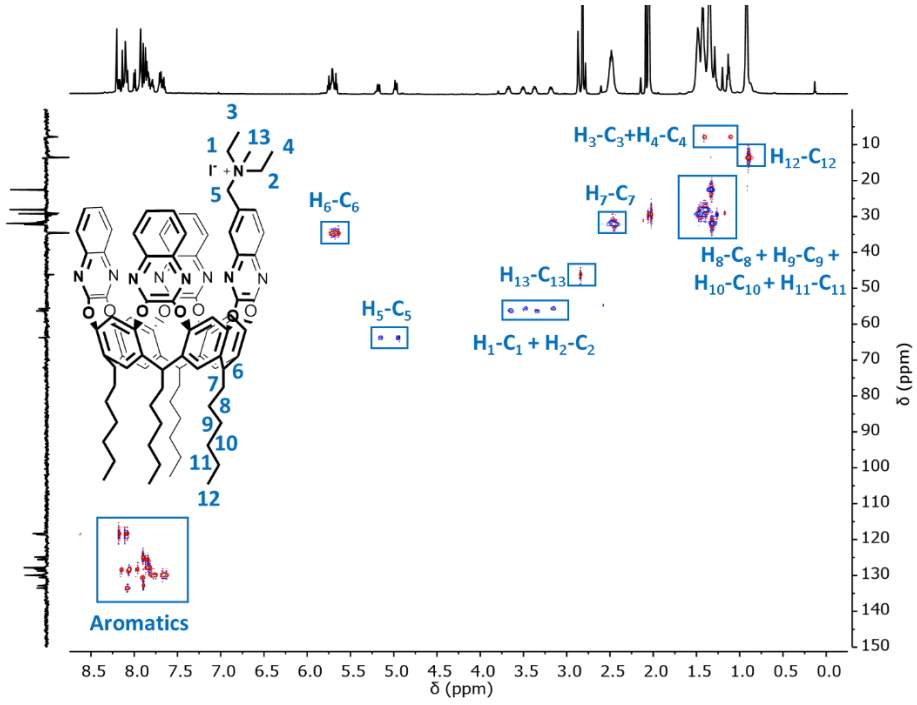

Figure A4.6. HSQC NMR spectrum of **QAQxCav**, in acetone-d6, 600 MHz, 25 °C.

4.6 References

(1) R. C. Buck, J. Franklin,U. Berger, J. M. Conder, I. T. Cousins,P. de Voogt, A. A. Jensen, K. Kannan, S. A. Mabury, S. P. J. van Leeuwen, Perfluoroalkyl and polyfluoroalkyl substances in the environment: Terminology, classification, and origins. *Integr. Environ. Assess Manag.* **2011**, *7*, 513–541, https://doi.org/10.1002/ieam.258.

(2) E. Kissa, (**1994**) Fluorinated surfactants: Synthesis–Properties–Applications (Surfactant science series 50), Ed. Marcel Dekker, New York.

(3) C. K. Taylor, (**1999**) Design and selection of performance surfactants: Annual surfactants review, Ed. John Wiley & Sons, New York.

(4) E. Kissa, (**2001**) Fluorinated surfactants and repellents (2nd edition revised and expanded) (Surfactant science series 97), Ed Marcel Dekker, New York.

(5) https://www.epa.gov/sdwa/and-polyfluoroalkyl-substances-pfas.

(6) https://eur-lex.europa.eu/legal-content/EN/TXT/?uri=celex%3A32006L0122.

(7) Y. Ruan, D. Lalwani, K.Y. Kwok, E. Yamazaki, S. Taniyasu, N. J. I. Kumar, P. K. S. Lam, N. Yamashita, Assessing exposure to legacy and emerging per- and polyfluoroalkyl substances via hair – The first nationwide survey in India. *Chemosphere* **2019**, *229*, 366-373, https://doi.org/10.1016/j.chemosphere.2019.04.195.

(8) J. M. Jian, Y. Guo, L. Zeng, L. Liang-Ying, X. Lu, F. Wang, E. Y. Zeng, Global distribution of PerFluoroChemicals (PFCs) in potential human exposure source–a review. *Environ. Int.* **2017**, *108*, 51-62, https://doi.org/10.1016/j.envint.2017.07.024.

(9) F. Suja, B. K. Pramanik, S. M. Zain, Contamination, bioaccumulation and toxic effects of Perfluorinated Chemicals (PFCs) in the water environment: a review paper. *Water Sci. Technol.* **2009**, *60*, 1533-1554, https://doi.org/10.2166/wst.2009.504.

(10) S. Poothong, E. Papadopoulou, J. A. Padilla-Sánchez, C. Thomsen, L. S. Haug, Multiple pathways of human exposure to poly- and perfluoroalkyl substances (PFASs): From external exposure to human blood. *Environ. Int.* **2020**, *134*, 105244, https://doi.org/10.1016/j.envint.2019.105244.

(11) A. A. Rand, S. A. Mabury, Is there a human health risk associated with indirect exposure to Perfluoroalkyl Carboxylates (PFCAs)?. *Toxicology* **2017**, *375*, 28-36, https://doi.org/10.1016/j.tox.2016.11.011.

(12) https://cen.acs.org/environment/persistent-pollutants/Getting-PFAS-drinking-water/102/i20.

(13) V. Mulabagal, L. Liu, J. Qi, C. Wilson, J.S. Hayworth, A rapid UHPLC-MS/MS method for simultaneous quantitation of 23 perfluoroalkyl substances

(PFAS) in estuarine water. *Talanta* **2018**, *190*, 95-102, https://doi.org/10.1016/j.talanta.2018.07.053.

(14) M. Rodríguez-Varela, J. C. Durán-Álvarez, B. Jiménez-Cisneros, O. Zamora, B. Prado, Occurrence of perfluorinated carboxylic acids in Mexico City's wastewater: A monitoring study in the sewerage and a mega wastewater treatment plant. *Sci. Total. Environ.* **2021**, 774, 145060, https://doi.org/10.1016/j.scitotenv.2021.145060.

(15) https://www.epa.gov/assessing-and-managing-chemicals-under-tsca/long-chain-perfluorinated-chemicals-pfcs-action-plan.

(16) J. W Martin, S. A. Mabury, K. R. Solomon, D. C. G. Muir. Dietary accumulation of perfluorinated acids in juvenile rainbow trout (Oncorhynchus mykiss). *Environ. Toxicol. Chem.* **2009**, *22*, 189–195, https://doi.org/10.1002/etc.5620220125.

(17) J. M. Conder, R. A. Hoke, W. de Wolf, M. H. Russell, R. C. Buck, Are PFCAs bioaccumulative? A critical review and comparison with regulatory criteria and persistent lipophilic compounds. *Environ. Sci. Technol.* **2008**, *42*, 995–1003, https://doi.org/10.1021/es070895g.

(18) G. W. Olsen, S.-C. Chang, P. E. Noker, G. S. Gorman, D. J. Ehresman, P. H. Lieder, J. L. Butenhoff, A comparison of the pharmacokinetics of perfluorobutanesulfonate (PFBS) in rats, monkeys, and humans. *Toxicology* **2009**, *256*, 65–74, https://doi.org/10.1016/j.tox.2008.11.008.

(19) F. Li, J. Duan, S. Tian, H. Ji, Y. Zhu, Z. Wei, D. Zhao, Short-chain per- and polyfluoroalkyl substances in aquatic systems: occurrence, impacts and treatment. *Chem. Eng. J.* **2020**, *380*, 122506, https://doi.org/10.1016/j.cej.2019.12250.

(20) http://eurlex.europa.eu/LexUriServ/LexUriServ.do?uri=OJ:L:2006:372:0032:0034:en:PDF.

(21) https://chm.pops.int/TheConvention/ConferenceoftheParties/ReportsandDecisions/tabid/208/Default.aspx.

(22) C. Gremmel, T. Frömel, T. P. Knepper, HPLC–MS/MS methods for the determination of 52 perfluoroalkyl and polyfluoroalkyl substances in aqueous samples. *Anal. Bioanal. Chem.* **2017**, *409*, 1643-1655, https://doi.org/10.1007/s00216-016-0110-z.

(23) J. L. Domingo, M. Nadal, Human exposure to per- and Polyfluoroalkyl Substances (PFAS) through drinking water: a review of the recent scientific literature. *Environ. Res.* **2019**, *177*, 108648, https://doi.org/10.1016/j.envres.2019.108648.

(24) E. F. Houtz, R. Sutton, J. S. Park, M. Sedlak, Poly- and perfluoroalkyl substances in wastewater: significance of unknown precursors, manufacturing shifts, and likely AFFF impacts. *Water. Res.* **2016**, *95*, 142-149, https://doi.org/10.1016/j.watres.2016.02.055.

(25) E. Gagliano, M. Sgroi, P. P. Falciglia, F. G. A. Vagliasindi, P. Roccaro, Removal of poly- and perfluoroalkyl substances (PFAS) from water by adsorption: Role of PFAS chain length, effect of organic matter and challenges in adsorbent regeneration. *Water Res.* **2020**, *171*, 115381, https://doi.org/10.1016/j.watres.2019.115381.

(26) J. R. Moran, S. Karbach, D. J. Cram, Cavitands: synthetic molecular vessels. *J. Am. Chem. Soc.* **1982**, *104*, 5826-5828, https://doi.org/10.1021/ja00385a064.

(27) P. J. Skinner, A. G. Cheetham, A. Beeby, V. Gramlich, F. Diederich, Conformational switching of resorcin [4] arene cavitands by protonation, preliminary communication. *Helv. Chim. Acta.* **2001**, *84*, 2146-2153, https://doi.org/10.1002/1522-2675(20010711)84:7<2146::AID-HLCA2146>3.0.CO;2-K

(28) M. Frei, F. Marotti, F. Diedrich, Zn II-induced conformational control of amphiphilic cavitands in Langmuir monolayers. *Chem. Comm.* **2004**, *4*, 1362-1363, https://doi.org/10.1039/B405331A.

(29) E. Dalcanale, G. Costantini, P. Soncini, Removal of organic pollutants from water via molecular inclusion within a cavitand. *J. Incl. Phenom. Mol. Recognit. Chem.* **1992**,*13*, 87-92, https://doi.org/10.1007/BF01076673.

(30) E. Dalcanale, P. Soncini, G. Bacchilega, F. Ugozzoli, Selective complexation of neutral molecules in organic solvents. Host–guest complexes and cavitates between cavitands and aromatic compounds. *J. Chem. Soc., Chem. Common.* **1989**, 500-502, https://doi.org/10.1039/C39890000500.

(31) M. Vincenti, E. Dalcanale, P. Soncini, G. Guglielmetti, Host-guest complexation in the gas phase by desorption chemical ionization mass spectrometry. *J. Am. Chem. Soc.* **1990**, *112*, 445–447, https://doi.org/10.1021/ja00157a068.

(32) F. Bertani, N. Riboni, F. Bianchi, G. Brancatelli, E. S. Sterner, R. Pinalli, S. Geremia, T. M. Swager, E. Dalcanale, Triptycene-Roofed Quinoxaline Cavitands for the Supramolecular Detection of BTEX in Air. *Chem. Eur. J.* **2016**, *22*, 3312–3319, https://doi.org/10.1002/chem.201504229.

(33) M. Amorini, N. Riboni, L. Pesenti, V. A. Dini, A. Pedrini, C. Massera, C. Gualandi, F. Bianchi, R. Pinalli, E. Dalcanale, Reusable Cavitand-Based Electrospun Membranes for the Removal of Polycyclic Aromatic Hydrocarbons from Water. *Small* **2022**, *18*, 2104946, https://doi.org/10.1002/smll.202104946.

(34) R. J. Hooley, H. J. Van Anda, J. Rebek, Extraction of Hydrophobic Species into a Water-Soluble Synthetic Receptor. *J. Am. Chem. Soc.* **2007**, *129*, 13464–13473, https://doi.org/10.1021/ja0727058.

(35) P. Roncucci, L. Pirondini, G. Paderni, C. Massera, E. Dalcanale, V. A. Azov, F. Diederich, Conformational Behavior of Pyrazine-Bridged and Mixed-Bridged Cavitands: A General Model for Solvent Effects on Thermal "Vase–Kite" Switching. *Chem: Eur J.* **2006**, *12*, 4775-4784, https://doi.org/10.1002/chem.200600085.

(36) F. U. Rahman, H. N. Feng, Y. Yu, A new water-soluble cavitand with deeper guest binding properties. *Org. Chem. Front.* **2019**, *6*, 998-1001, https://doi.org/10.1039/C9QO00049F.

(37) P. Jing, P. J. Rodgers, S. Amemiya, High Lipophilicity of Perfluoroalkyl Carboxylate and Sulfonate: Implications for Their Membrane Permeability. *J. Am. Chem. Soc.* **2009**, 131, 2290–2296, https://doi.org/10.1021/ja807961s.

(38) J.-P. Behr, (**1994**) The Lock and Key principle. The state of the art – 100 years on, Wiley Publishing.

(39) K-.D. Zhang, D. Ajami, J.V. Gavette, J. Rebek, Alkyl Groups Fold to Fit within a Water-Soluble Cavitand. *J. Am. Chem. Soc.* **2014**, *136*, 5264–5266, https://doi.org/10.1021/ja501685z.

(40) N.-W. Wu, J. Rebek*,* Cavitands as Chaperones for Monofunctional and Ring-Forming Reactions in Water. *J. Am. Chem. Soc.* **2016**, 138, 7512–7515, https://doi.org/10.1021/jacs.6b04278.

(41) A. Favero (2020). Biochemical and environmental sensing with cavitands [Doctoral dissertation, Università di Parma]. DSpaceUnipr.

(42) E. Román, C. Peinador, S. Mendoza, A. E. Kaifer, Improved Synthesis of Cavitands. *J. Org. Chem.* **1999**, *64*, 2577–2578, https://doi.org/10.1021/jo982218y.

(43) R. Wang, Z.-W. Lin, M. J. Klemes, M. Ateia, B. Trang, J. Wang, C. Ching, D. E. Helbling, W. R. Dichtel, A Tunable Porous β-Cyclodextrin Polymer Platform to Understand and Improve Anionic PFAS Removal. *ACS Cent. Sci.* **2022**, *8*, 663–669, https://doi.org/10.1021/acscentsci.2c00478.

(44) K. R. Sanchez-Lievanos, D. Zhang, S. M. Simpson, M. K. Wijayahena, G. Rizzo, J. M. N. Aguilar, L. M. Abaya, J. M. Dovi, H. I. Sirotkin, M. R. Crawley, T. R. Cook, D. S. Aga, Synthesis and Evaluation of Cationic Porphyrin-Based Organic Nanocages for the Removal of 38 PFAS from Water: Experimental, Theoretical, and Eco-toxicological Insights, *ACS EST Eng.* **2024**, https://doi.org/10.1021/acsestengg.4c00639.

Abbreviations

BAETDMA	Bisphenol A ethoxylate dimethacrylate
BFDGE	Bisphenol F diglycidyl ether
CPI	Cationic Photoinitiator
DBEDMA	Diboronate ester dimethacrylate
DCM	Dichloromethane
DEA	Diethylamine
DIPEA	*N,N*-Diisopropylethylamine
DMA	Dynamic Mechanical Analysis
DMAP	4-Dimethylaminopyridine
DMF	Dimethylformamide
DSC	Differential Scanning Calorimetry
ESI-MS	Electrospray Ionization Mass Spectrometry
EtOAc	Ethyl acetate
GC-MS	Gas Chromatography - Mass Spectrometry
HEMA	2-Hydroxyethyl methacrylate
IM	2-Methylimidazole
ISDGE	Isosorbide diglycidyl ether
ISGDMA	Isosorbide diglycidyl methacrylate
Log PO'	Octanol-water partition coefficient
MeCN	Acetonitrile
MeI	Methyl iodide
MeOH	Methanol
NaPFO	Sodium perfluorooctanoate
NMR	Nuclear Magnetic Resonance
PFAS	Poly- and Perfluoroalkyl Substances
PFOA	Perfluorooctanoic acid
PFOS	Perfluorooctanesulfonic acid
PPGDA	Polypropylene glycol diacrylate
PTSA	p-Toluenesulfonic acid
QAQxCav	Quinoxaline Cavitand with Quaternary Ammonium function

RPI	Radical Photoinitiator
TGA	Thermogravimetric Analysis
THF	Tetrahydrofuran
TI	Thermal Initiator
TMA	Thermomechanical Analysis
UHPLC-HRMS	Ultra High Performance Liquid Chromatography - High Resolution Mass Spectrometry
VP	Vat Photopolymerization
SLA	Stereolithography
CAD	Computer Aided Design
Tg	Glass transition temperature
BAPO	Phenylbis(2,4,6-trimethylbenzoyl)phosphine oxide
ECC	3,4-Epoxycyclohexylmethyl-3',4'-epoxycyclohexane carboxylate

La borsa di dottorato è stata cofinanziata con risorse del
Programma Operativo Nazionale Ricerca e Innovazione 2014-2020, risorse FSE REACT-EU
Azione IV.4 “Dottorati e contratti di ricerca su tematiche dell’innovazione”
e Azione IV.5 “Dottorati su tematiche Green”